On the Transition from Two- to Three-Dimensional Behavior in Adsorbed Films

Thesis by
Peter Kenneth Day

In Partial Fulfillment of the Requirements
for the Degree of
Doctor of Philosophy

California Institute of Technology
Pasadena, California

1993

(Defended January 4, 1993)

Acknowledgements

First, I would like to thank my parents, without whose support, this work would not have been possible. This thesis is as much theirs as it is mine. I am very grateful to Dr. Mark Lysek, whose work I continue, for introducing me to Low Temperature Physics, for countless words of advice, and above all, for his friendship. Dr. David Goodstein, who was all I could have hoped for in a thesis advisor, deserves much of the credit for the writing and the intellectual content of this thesis. I would like to thank him for his unerring guidance and for allowing me the independence I cherished. I am also very grateful to Drs. Peter Weichman and Michael Cross for explaining the theory to me, and to Nils Asplund for technical assistance. Finally, I would like to thank Dr. Nai Chang Yeh, for encouraging me to work as hard as possible, and my fellow rats in the lab upstairs, for their companionship.

Abstract

Argon and krypton films adsorbed on graphite foam have been studied in detail using vapor pressure and high resolution, heat capacity measurements. Heat capacity features near the bulk triple point temperature, previously associated with the surface melting of the uniform film, are shown to be due to the melting of bulk material condensed in pores in the substrate. The melting curve of the capillary condensate agrees with the prediction of a modified Clausius–Claperon equation. The second and third layers in argon and the second layer in krypton have a triple point at which two-dimensional solid, liquid, and gas phases coexist atop a solid lower layer. Commensurate–incommensurate transitions are found in the first two layers of argon and in the second layer of krypton, so that monolayer argon melts from a registered phase, but the second layers of both systems melt from incommensurate bilayer phases. The melting of the second and third layers in both systems are likely to be first order, but the data are not conclusive. At coverages starting with $3\frac{1}{2}$ layers, heat capacity features that are due to reentrant layering-transitions are seen in both systems, confirming the result of recent ellipsometry studies. Further heat capacity peaks suggest phase transitions that join the newly observed reentrant layering-transitions with the well studied layering-transitions at low temperature. These heat capacity peaks may be related to the recently proposed preroughening transition. A mean field theory is developed that reproduced the reentrant layering behavior for ratios of nearest and next nearest neighbor interaction energies greater than a critical value. The mean field theory gives an explanation for the appearance of reentrant layering-transitions at different film thicknesses depending on the substrate–adsorbate interaction parameter. Multilayer phase diagrams are drawn from the data that suggest a crossover from two-dimensional behavior in the second layer to bulk interfacial behavior in the higher layers. In an appendix, layering and melting transitions in CF_4 on graphite are analysed.

Contents

1 Introduction to Multilayer Film Studies **1**

1.1 Substrates 1

1.2 Monolayer Studies 5

1.3 Wetting Phenomena and the Approach to Three Dimensions . . . 10

1.4 Multilayer Phase Diagrams 13

1.5 Observations of Layering in Heat Capacity Measurements 16

1.6 Ellipsometry Data 17

2 Experimental Apparatus and Methods **20**

2.1 Scanning Ratio Calorimetry 21

2.2 The Experimental Apparatus 23

2.3 Instrumentation and Interface 26

2.4 Sample Gas Handling System 30

2.5 Experimental Procedures and Data Reduction 33

2.6 Background Runs and Noise in the Heat Capacity 38

2.7 Desorption Correction 40

3 Results **44**

3.1 Isotherms 45

3.1.1 Wetting Behavior 45

3.1.2 Hysteresis 52

3.2 First-Layer Melting in Argon 55

3.3 Second-Layer Phase Diagrams 58
3.4 Second-Layer Melting above the Triple Point 64
3.5 Third-Layer Phase Diagram 70
3.6 Higher Layers 78

4 Roughening, Preroughening, and Multilayer Films **91**
4.1 History of Roughening 91
4.2 Roughening Near an Attractive Substrate 95
4.3 Preroughening at the Crystal Interface 99
4.4 Comparison with the Data 103
4.5 Mean-Field Theory of Reentrant Layering 105

5 Other Models of Film Behavior **115**
5.1 The FCC Adsorption Model 116
5.2 Surface Melting and Substrate-Induced Freezing 123

6 Conclusions **129**

A Melting of Capillary-Condensed Solid **132**

B And now for something completely different **144**
B.1 Monolayer and Extended Monolayer Triple points 147
B.2 Melting from the HI phase 150
B.3 Orientational transition and layering 153
B.4 Melting in the third and fourth layer 157
B.5 Conclusions about CF_4 160

C Log of runs **161**

Bibliography **167**

List of Figures

1.1 Examples of isotherms. 2
1.2 The graphite interaction potential. 4
1.3 An example heat capacity scan. 6
1.4 Ar and Kr monolayer phase diagrams. 9
1.5 Wetting behavior of films. 11
1.6 Examples of multilayer phase diagrams. 15
1.7 Schematic phase diagram for multilayer methane. 18

2.1 A scanning ratio calorimeter. 22
2.2 Schematic diagram of the calorimeter probe, vaccuum can, and cryogenic dewars. 24
2.3 Block diagram of the instrumentation related to the heat capacity measurement. 27
2.4 Automated ultrahigh purity gas handling system 31
2.5 Background heat capacity of the sample cell for three different scan rates. 39
2.6 Scatter in the heat capacity data. 41
2.7 Percent RMS deviation in the heat capacity data. 42

3.1 77K argon isotherm in P versus N. 47
3.2 102K Krypton isotherm in P versus N. 48
3.3 Argon isotherm in μ versus N. 49
3.4 Krypton isotherm in μ versus N. 50
3.5 Examples of "capillaries" in a porous substrate. 54
3.6 First-layer melting peaks in argon on graphite. 57
3.7 Second-layer, triple-point peaks in argon. 60
3.8 Second-layer, triple-point peaks in krypton. 61

3.9 μ trajectories for scans around the second and third layering-transitions in Ar. 62
3.10 μ trajectories around the second layering-transition in Kr. 63
3.11 Second-layer melting above the triple point in argon. 66
3.12 Second-layer melting above the triple point in krypton. 67
3.13 Rising edges of second-layer melting peaks in argon. 68
3.14 Rising edges of second-layer melting peaks in krypton. 69
3.15 Possible phase diagrams for second-layer argon and krypton. . . . 70
3.16 Heat capacity scans around the third-layer triple point in argon. . 71
3.17 Third-layer melting in argon above the triple point. 72
3.18 Heat capacity scans, corrected for desorption, around the formation of the third layer in krypton. 73
3.19 μ trajectories around the end of the third layering-transition in krypton. 74
3.20 Possibilities for the third-layer phase diagram in Kr 75
3.21 Phase diagram for the first three layers of argon/graphite in (N, T). 76
3.22 Phase diagram for the first three layers of krypton/graphite in (N, T). 77
3.23 Heat capacity scans around reentrant layering-transition $3\frac{1}{2}$ in Ar. 80
3.24 Heat capacity scans around layering-transition $4\frac{1}{2}$ in Ar. 81
3.25 Heat capacity peaks in Ar at low temperatures for coverages higher than $3\frac{1}{2}$ layers. 83
3.26 Closely spaced heat capacity scans around reentrant layering-transition $3\frac{1}{2}$ in Kr. 86
3.27 μ trajectories around reentrant layering-transition $3\frac{1}{2}$ in Kr. . . . 87
3.28 Low-temperature peaks for coverages higher than $3\frac{1}{2}$ in Kr. . . . 88
3.29 Argon/graphite multilayer phase diagram in $(\mu_0 - \mu)^{-1/3}$. 89
3.30 Krypton/graphite multilayer phase diagram in $(\mu_0 - \mu)^{-1/3}$. . . . 90

4.1 Solid-on-solid models. 92
4.2 The Huse potential. 98
4.3 Arrow diagrams for rough and DOF surfaces. 100
4.4 Two plaquette configurations illustrating nnn interactions. 100
4.5 Possibilities for multilayer phase diagrams when a preroughening transition occurs at the crystal surface. 102
4.6 The mean-field partition function. 106
4.7 $\mathcal{F}_{MF}$ plotted versus m for various values of the parameters. 108
4.8 Surface phase diagrams calculated using the five-height model. . . 111
4.9 Examples of calculated phase diagrams in $(h, L/T)$. 112

5.1 Multilayer phase diagram based on the FCC adsorption model. . . 116
5.2 Kr phase diagrams from previous studies. 118
5.3 Possible states of films in the continuum model. 124

A.1 Capillary-condensate melting peaks for argon. 133
A.2 Capillary-condensate melting peaks for krypton. 134
A.3 Positions of capillary-condensate melting peaks plotted in (μ, T). . 138
A.4 X versus temperature for argon and krypton. 141
A.5 X versus temperature for CH_4 adsorption and desorption runs. . 142

B.1 A phase diagram for an incompletely wetting film 145
B.2 The phase diagram proposed by Zheng *et al.* for monolayer and extended monolayer CF_4. 147
B.3 Heat capacity scans in monolayer and extended monolayer CF_4 . 148
B.4 (N, T) plots of two possibilities for the triple point phenomenon in the extended monolayer of CF_4. 150
B.5 Melting of the HI phase and bilayer peaks. 152
B.6 Peaks due to the orientational transition at low coverage. 155

B.7 Peaks that are due to the orientational transition at higher coverage. 156
B.8 The melting of the third and fourth layers. 158

List of Tables

2.1 Saturated vapor-pressure fit coefficients 38

3.1 Locations of isotherm steps. 51
3.2 Layer triple points and endpoints of layering-transitions. 84
3.3 Starting points of reentrant layering-transitions. 84
3.4 Endpoints of reentrant layering-transitions. 84

5.1 Surface freezing in all systems studied 125

6.1 Roughening and preroughening temperatures. 131

B.1 Individual layer triple points in CF_4 159

Chapter 1

Introduction to Multilayer Film Studies

1.1 Substrates

The first adsorption studies on inert subtrates were carried out more for studying the characteristics of the substrate/adsorbent rather than of the adsorbate. Isotherm studies, measurements of pressure versus number of gas molecules adsorbed, were carried out on numerous different materials, typically using nitrogen or krypton gas. In these studies, known quantities of gas were let into a sample cell containing a form or carbon, alkali halide, or other adsorbent to be studied. By measuring the number remaining in the gas phase and subtracting from the total number, the number of molecules adsorbed could be calculated at various pressures.

Figure 1.1(a) shows the typical behavior of such an isotherm. Starting from a bare substrate, a quantity of gas is immediately adsorbed without much rise in the pressure. Past this critical amount, much more of the gas put into the sample cell remains in the vapor phase, and the pressure gradually rises with the number adsorbed until the bulk-saturated vapor pressure, P_0, is reached. At P_0, bulk material (either solid or liquid) begins to form, so in principle, all the additional gas introduced into the cell would be adsorbed. The first step in the isotherm

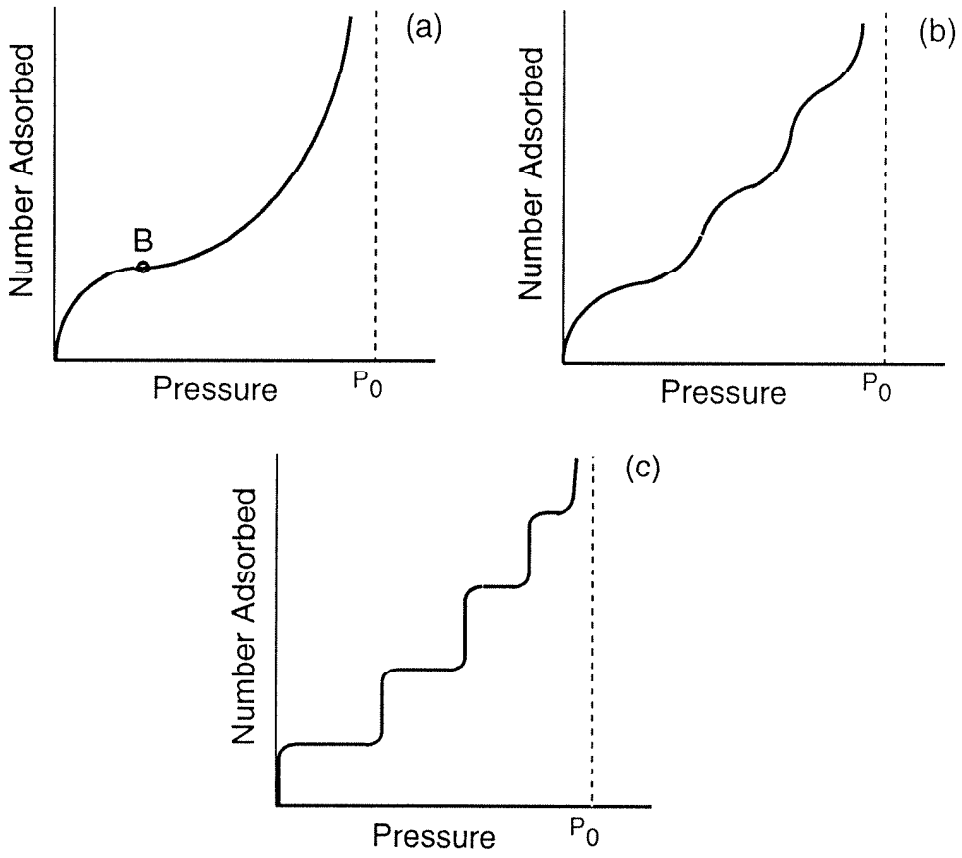

Figure 1.1: Examples of isotherms using (a) porous substrates, (b) graphitized carbon black, and (c) exfoliated graphite foam.

was identified with the physical adsorption of a monolayer of gas onto the surface. Thus, it was possible to measure, at least relatively, the surface area of various adsorbents by finding the inflection point (the point labeled B in Fig. 1.1(a)) of isotherms measured using a standard adsorbate. This idea found numerous industrial applications and is still being used to characterize surfaces.

There was early speculation by Fowler and Guggenheim[1], and also by Halsey[2] and Hill[3], that adsorption on a perfectly uniform surface should give rise to isotherms qualitatively different from those that had been measured experimentally. Assuming that the heat of adsorption of atoms into the first layer is equal at all adsorption sites and is greater than the heat of adsorption into the second

layer, also equal at all sites, and so on, they reasoned that adsorption onto a perfectly homogeneous surface should result in isotherms composed of a sequence of steps between integer film thicknesses. In this view, the shapes of the isotherms that had been measured in experiments were due to a superposition of stepwise isotherms resulting from the variation of binding energies over the heterogeneous surfaces actually used. This idea was corroborated by an experiment by Polley et al. [4] in which adsorption isotherms were measured on samples of carbon black subjected to heat treatments at various temperatures. The heat treatment caused a transition from approximately spherical particles to polyhedral-shaped, "graphitized" particles. Rounded steps appeared in the isotherms taken using the heat treated samples, and at least three steps were seen in samples that were treated at the highest temperatures. A gradual transformation from isotherms of type (a) in Fig. 1.1 to type (b) was seen, and the sharpness of the steps varied directly with the average crystal size of the particles in the sample. Thus, adsorption isotherms could be used to study the homogeneity of a surface as well as the surface area, by measuring the number and sharpness of steps.

A major transformation of the field of adsorption studies occurred in the late sixties and early seventies with the pioneering work of Thomy and Duval[5, 6, 7], who were the first to measure adsorption isotherms on a form of carbon called exfoliated graphite foam, now known as grafoam[8]. Grafoam is formed by chemically separating graphite planes by intercalating gas between the planes of a crystal and then heating. The result is then recompressed to various degrees to produce either grafoam or the denser grafoil.

Using methane, krypton, and xenon for adsorbates, isotherms were measured yielding five very sharp steps, indicating that the graphite surface produced is extremely uniform[5]. The isotherms were found to agree well with the a theoretical prediction now known as the Frenkel–Halsey–Hill (FHH) equation[2, 3]. The FHH equation assumes that the atoms adsorbed in a multilayer film act approximately

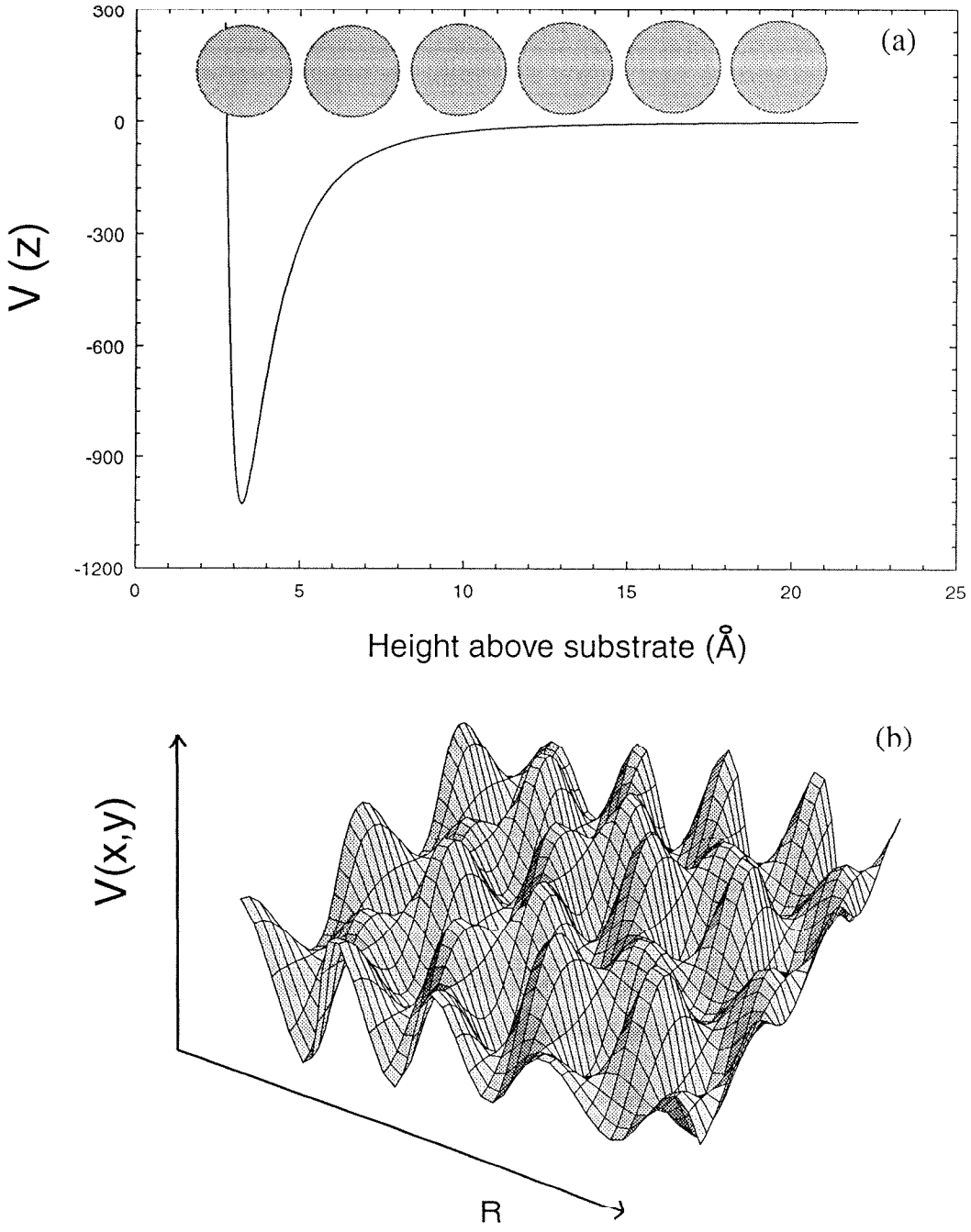

Figure 1.2: (a) The Steele potential for methane adsorbed on graphite. The approximate average positions of molecules in layers one through six are shown. (b) Approximate representation of the corrugation potential that is due to the honeycomb graphite lattice.

like the atoms in normal bulk material. Thus the chemical potential, μ, of the film is equal to the bulk chemical potential, μ_0, plus the potential difference, ΔV between a semi-infinite region of adsorbate atoms and a semi-infinite region of substrate atoms. The attractive interaction of the substrate is due to Van der Waals forces that fall off as $1/r^6$ between atoms. By integrating over three dimensions, the substrate potential should vary as $1/z^3$[9], where z is the height above the substrate (Fig. 1.2). Therefore, the FHH equation is given by

$$\mu - \mu_0 = \frac{C_3}{z^3}, \tag{1.1}$$

where C_3 is a constant, depending on the substrate–adsorbate interaction. The height of the film, z, is related to the number adsorbed in the film, N, by $N = zN_0$, where N_0 is the monolayer coverage. If an isotherm is plotted as $(\mu_0 - \mu)^{-1/3}$ versus N, the FHH equation predicts a uniform staircase (steps spaced evenly along the ordinate) with average slope C_3.

1.2 Monolayer Studies

Perhaps the contribution made by Thomy and Duval most significant to the history of adsorption studies was the observation of two-dimensional monolayer phases[7]. Studies had previously shown the existence of a phase transition between an expanded phase and a condensed phase in the first layer of helium adsorbed on sintered copper sponges[10, 11]. The results of Thomy and Duval using exfoliated graphite were more reproducible and clearly showed the existence of three two-dimensional phases, solid, liquid, and gas, existing in the first layer and meeting at a 2D triple point. This experiment marked a turning point for adsorption studies at which the adsorbate, rather than the substrate, became the focus of experimental attention.

Although other substrates are now used in some types of experiments on adsorbed films (notably single-crystal substrates may be used in x-ray experiments),

exfoliated graphite is by far the most common. Three characteristics make it a nearly ideal substrate for monolayer studies, and an acceptable substrate for multilayer studies. First, the surface coherence length is on the order of $1000\mathring{A}$[12], large enough so that phase transitions in the films are not dominated by finite size effects. Second, a very large surface area of about twenty meters squared per gram results from the exfoliation process, allowing for accurate volumetric measurements of submonolayer quantities of gas. Third, grafoam is a good thermal conductor so that thermal equilibrium times are reasonably low, and high resolution heat capacity experiments are possible. To demonstrate the uniformity of the grafoam surface, Fig. 1.3 shows a heat capacity scan, taken during the course of this study, displaying a peak caused by the melting of 0.6 monolayers of CF_4 adsorbed on grafoam. The width of the peak at half max is about 0.3K, which is slightly greater than the thermal equilibrium time of the scanning measurement.

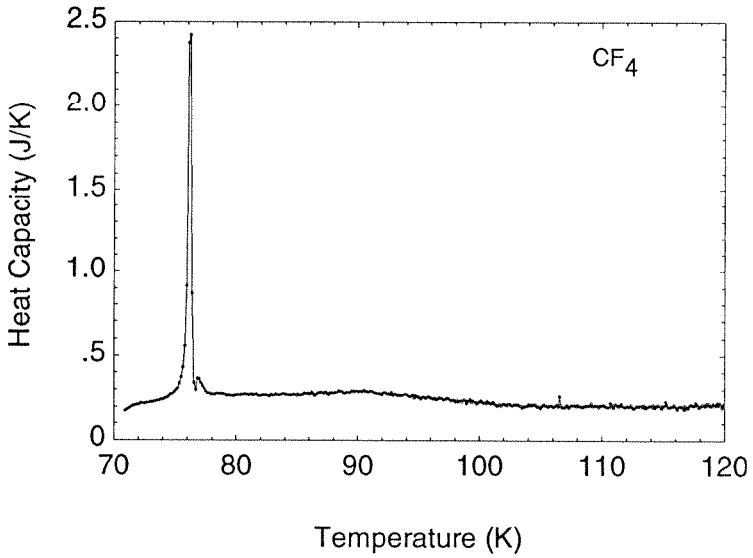

Figure 1.3: Heat capacity scan at 0.6 monolayers of CF_4 adsorbed on grafoam. The width of the peak at half max is $\sim$ 0.3K.

Much of the work with adsorbed films has concentrated on monolayer and submonolayer films because of the interest in two-dimensional phase transitions

that ensued from the theoretical work of Kosterlitz, Thouless, Halperin, Nelson and Young (KTHNY)[13, 14, 15, 16]. These authors proposed that melting in two dimensions may be a two-step process. At low temperatures, the two-dimensional solid is characterized by a quasi-long-ranged (algebraically decaying), positional order. At a continuous melting transition, the solid is transformed into a hexatic phase that is positionally disordered, but has a sixfold orientational order. At a second continuous transition, the orientational order is lost, and a completely disordered fluid phase results. The KTHNY theory suggests that it is possible for two-dimensional melting to be radically different from melting in three dimensions. Another mechanism for two-dimensional melting was proposed by Fisher et al. [17] and by Chui[18, 19]. The pair of continuous melting transitions predicted by KTHNY may be preempted by a single, first-order "grain-boundary melting" transition at which the proliferation of grain boundaries causes the solid to disorder.

The question to be answered by the experiments was whether one or both of these mechanisms for 2D melting occur in nature. Monolayer adsorption studies are candidates for experimental realizations of two-dimensional behavior, because the inverse cubic substrate potential is very steep at the first layer (see Fig. 1.2(a)), so that motion of the adsorbed molecules is confined to be in the plane. However, in adsorption studies using graphite, there is an additional complication that hinders this type of investigation. The graphite substrate potential is corrugated in the x–y direction (parallel to the plane of the substrate) by the honeycomb carbon lattice (Fig. 1.2(b)). The corrugation has two effects. First, the substrate will always induce some sixfold orientational order on the first layer. It may still be possible to observe the orientational disordering transition of the KTHNY theory, but it will be washed out like the ferromagnetic Ising transition in a small magnetic field. Second, the corrugation may give rise to registered phases in which adatoms sit exactly over the wells of the substrate potential. Because regis-

tered phases have different symmetry properties than continuous 2D solids, they are expected to undergo completely different types of order–disorder transitions characteristic of lattice gases. Scattering and heat capacity experiments have shown that three different solid phases occur in monolayer methane on graphite: a $\sqrt{3} \times \sqrt{3}$ registered phase in which there is one methane molecule per adsorption site, a low-density, incommensurate (unregistered) phase, and a high-density, incommensurate phase. Registry transitions occur between these various solid phases and can make for very complex monolayer phase diagrams.

Phase diagrams for monolayer argon, as determined by neutron diffraction [20, 21], heat capacity[22], vapor pressure isotherm [23], and x-ray scattering[24]; and for monolayer krypton, as determined by heat capacity[25] and x-ray scattering[26], are shown in Fig. 1.4 in both the (N,T) and (μ,T) representations (see also Ref. [27] for a review of monolayer phase diagrams.) All studies in the argon system, except the heat capacity study, found a continuous melting transition (shown with a dashed line in the figure) between high-density, incommensurate (HD) solid and fluid phases. In this view, HD solid, liquid and gas phases coexist at the critical endpoint of the order-disorder transition (marked with a triangle in the figure). The liquid-vapor coexistence region ends in a normal critical point (marked with a circle). The results of the heat capacity study, which found a small but sharp peak near the melting temperature at submonolayer coverages, cast some doubt upon this proposed phase diagram. In Section 3.2 , possible changes to the phase diagram in the extended monolayer region ($N > 1$ layer) are discussed. It was found in the present study that the melting transition at very high monolayer densities is most likely first-order and may occur from the registered instead of HD phase.

The krypton monolayer phase diagram is topologically different from that of argon and follows the "incipient triple-point" [27] behavior found in monolayer CO and N_2 on graphite. In the incipient triple-point model [25, 28, 29], the

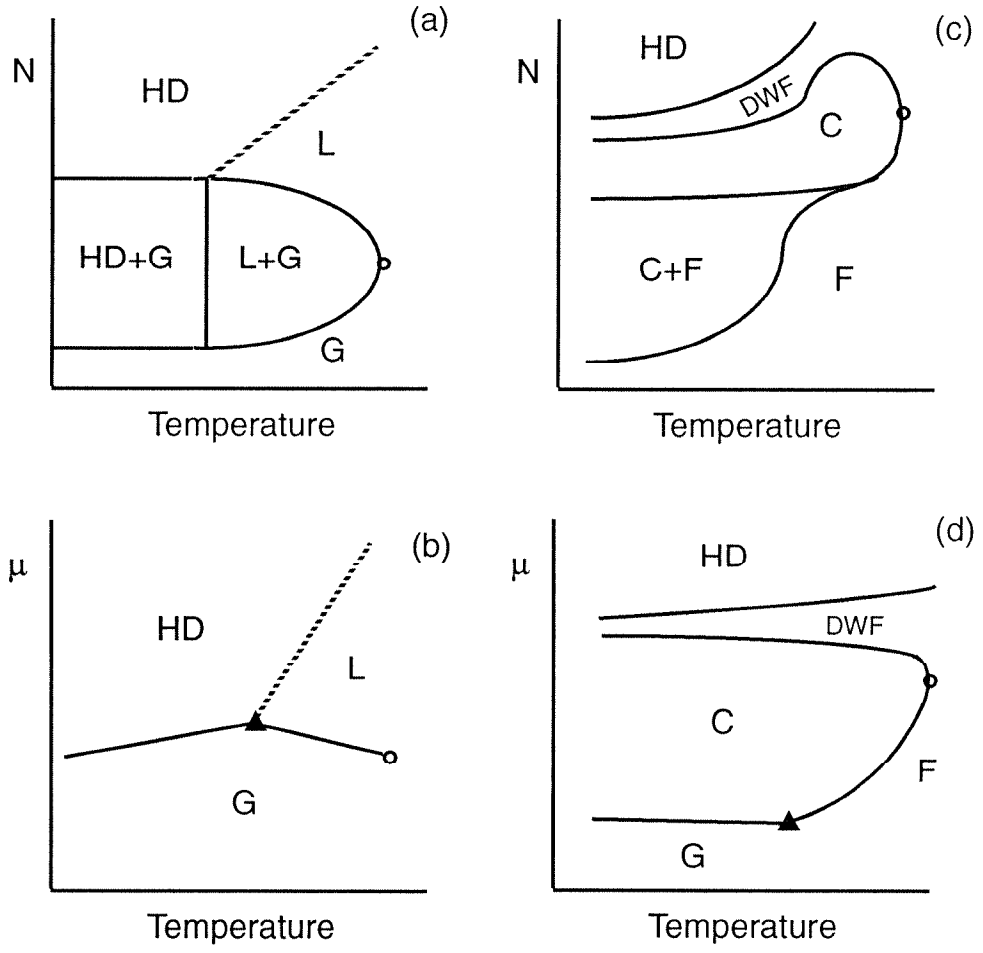

Figure 1.4: Monolayer phase diagrams from Ref. 26 for argon in (a) N vs. T, (b) μ vs. T, and krypton in (c) N vs. T, (d) μ vs. T. HD means high-density, incommensurate solid; L means liquid; G means gas; C means commensurate solid; F means uniform fluid; and DWF means "domain wall fluid". The dashed line is the possible second-order melting transition in argon. Circles show the locations of the Ising critical point in argon and the Potts critical point in krypton.

registered solid is stabilized by the substrate to a higher temperature than is allowed for two-phase coexistence between liquid and gas phases. Thus, there are no separate liquid and gas phases, but only a uniform fluid. It is believed that a tricritical point exists in the extended monolayer at which the melting of the registered solid changes from first-order to second-order[27]. Also a "Potts critical point" is thought to exist at the high-temperature limit of the commensurate solid phase[27]. At higher coverages, the registered solid is found to give way to a HD solid, which then becomes the substrate for the multilayer film. Between the HD and registered solid phases, the x-ray studies find evidence of a "domain-wall fluid" (also known as reentrant fluid or well-oriented fluid.) The monolayer krypton phase diagram is shown here only for completeness. No modifications to it are made in this work, although the possibility that the second layer of krypton induces disorder into the first layer in a region of the multilayer phase diagram is discussed in Section 5.1.

1.3 Wetting Phenomena and the Approach to Three Dimensions

The study of multilayer films ensued from the widespread interest in monolayer studies and a systematic progression to higher coverages. The stated purpose of many experiments on multilayer films was to study the transition from two-dimensional to three-dimensional behavior. For example, if the melting behavior in 2D is continuous, at what point does it become first-order as the film thickness increases? Other experiments were focused on the behavior of surfaces and their influence on the behavior of the bulk. For example, heat capacity[30, 31] and neutron diffraction studies[32, 33] have concluded that three-dimensional melting is initiated with a fluid layer that forms at a surface at below the bulk melting temperature. The thickness of the liquid layer then increases divergently as the

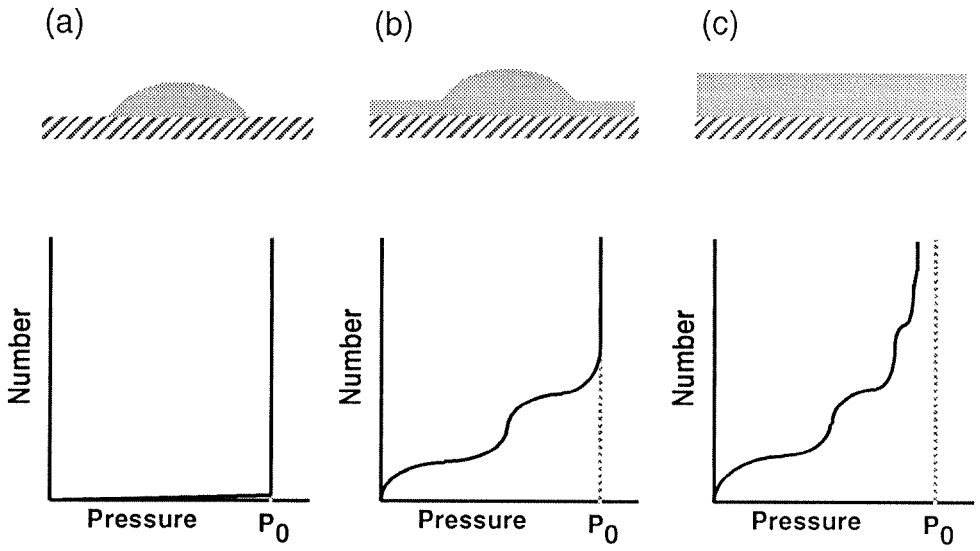

Figure 1.5: Different types of wetting behavior: (a) non-wetting, the adsorbate forms beads of bulk material on the substrate at the bulk vapor pressure; (b) incompete wetting, bulk material is formed after the film has reached a finite thickness; (c) complete wetting, an infinite thickness film is formed.

melting temperature is approached. It will be argued that previous multilayer film studies (except possibly for helium) have not shown a crossover from two- to three-dimensional behavior. However, heat capacity data gathered in this study will be interpreted in terms of a crossover from two-dimensional behavior in thinner films to bulk interfacial behavior in thicker films.

The first issue that must be considered in a study of multilayer films is the wetting behavior of the particular adsorbate on the particular substrate used. An adsorbate is said to wet a substrate when a film forms at the substrate-vapor interface. In the case of non-wetting, the adsorbate will form beads of condensed material on the substrate only when the bulk vapor pressure is reached (Fig. 1.5(a)). Two types of behavior are classified under the term wetting, complete wetting and incomplete wetting. The FHH equation applies to a completely wetting film. As the bulk vapor pressure is approached, the film thickness will diverge (Fig. 1.5(c)). In the case of an incompletely wetting film, the thickness

will remain finite at the bulk vapor pressure (Fig. 1.5(b)). The class of wetting of a particular substrate–adsorbate systems is known to depend on a delicate balance between the parameters u, the adsorbate–substrate interaction strength and v, the adsorbate–adsorbate interaction strength[34]. For large u/v, wetting is expected to be complete for a fluid film, and for small u/v, wetting should be incomplete. For a solid film, the mismatch between the lattice constants of substrate and adsorbate must also be taken into account[35, 36, 37]. In the case of a large mismatch, non-wetting or incomplete wetting behavior will result. For very large u/v, the first layer may be highly compressed, creating a mismatch between it and the bulk lattice spacing. Therefore, complete wetting in solid films may be realized only for intermediate values of u/v. An analysis of the wetting behavior in the systems that have been studied so far seems to confirm this hypothesis[38].

Ellipsometry studies are best at determining wetting properties when the vapor pressure is high. Ellipsometric isotherms[39, 40] have shown evidence of the formation of at least eleven layers of argon adsorbed on highly oriented pyrolytic graphite (HOPG). A volumetric isotherm study [41] showed the existence of at least five steps on exfoliated graphite powder. In krypton on HOPG, an ellipsometry measurement [42] has resolved seven steps between 55 and 95K and did not see scattering that was due to bulk crystalites until 16 layers were adsorbed. Thomy and Duval[5, 6] observed five sharp steps in volumetric isotherms on exfoliated graphite foam. On the other hand, vibrating fiber experiments, in which the frequency of a graphite fiber is measured to determine the amount adsorbed, have shown a maximum of only four layers of krypton at 78K[43] and six layers of argon at 61K[44]. The significance of these results is questionable because it was found that the maximum film thickness depends on the quality of the graphite fiber.

It was recently shown [45, 46] in the methane study conducted in our laboratory that the maximum number of film layers that may be formed on grafoam is signif-

icantly smaller than the number that may be formed on single-crystal graphite or HOPG. The difference is not due to wetting behavior (the same crystal face of the graphite is exposed in each case). Instead, it turns out that capillary condensation becomes important at around three layers on grafoam. Capillary condensation occures when bulk material becomes nucleated in pores and cracks in the substrate. The bulk material is able to condense below the bulk-saturated vapor pressure by forming a negative radius of curvature, and therefore a pressure differential, between itself and the vapor. This phenomenon will be discussed in greater detail in section 3.1. In the methane study, it was found that the maximum film thickness was effectively limited to a little over four layers, because after this point, all additional gas admitted to the cell would enter the capillary condensate instead of the film. In this work, it is demonstrated that it is actually possible to form a maximum of about six layers of both argon and krypton on grafoam by letting large amounts of gas into the cell. Because the substrate potential becomes very small by about four or five layers (Fig. 1.2(a)), it may be possible to study some aspects of surface behavior in films only six layers thick.

1.4 Multilayer Phase Diagrams

Phase diagrams for multilayer films, as for monolayer films, were first drawn from the results of volumetric isotherm experiments. These phase diagrams are typically drawn in either the (N, T) plane, where N is the number adsorbed, or the (μ, T) plane, where μ is the chemical potential derived from the pressure and temperature of the vapor. In Fig. 1.6(a), the thick, solid lines correspond to phase transitions in the bulk material. The multilayer film coexists with the vapor phase in the lower region of the phase diagram. Double lines in the figure correspond to first-order phase transitions in the film called "layering-transitions". The layering-transitions are the step discontinuities found in the isotherms at low temperature

and indicate the pressure at which a layer abruptly condenses on the surface. In the case of a completely wetting film, the layering-transitions become more closely spaced as the bulk-saturated chemical potential is approached because of the $1/z^3$ form of the substrate potential. It was found that as the temperature is increased, the steps in the isotherms disappear. Thus, past a certain temperature, film growth becomes a continuous process, so the first-order layering-transitions are expected to end at "layering critical points" (shown with circles in the figure). It is believed that the layer critical points must converge at bulk coexistence either at the triple point or somewhere along the solid-vapor boundary, because very thick, liquid films should not be able to support layering-transitions.

Figure 1.6(b) shows the same behavior in the N vs. T plane. In this representation, the first-order layering-transitions become "coexistence regions" where two phases are stable. At low temperatures, starting at zero coverage, a small amount of two-dimensional gas forms on the substrate. The density of 2D gas increases until a critical density, depending on the temperature, is reached. At this point, patches of 2D solid begin to form, and these patches grow until they cover the whole layer. As further molecules are added to the system, a small amount of two-dimensional gas will form on top of the first layer, and the process will repeat. As the temperature is increased, the density difference between the gas and solid phases in a given layer decreases and finally vanishes at the layering critical point. This picture of film growth, as derived from the isotherm results, has been called the "lattice-gas adsorption model"[47], because there is no change in symmetry between, for example, the gas and solid phase of the second layer. That is, it is possible to traverse the path shown from point A to point B in Fig. 1.6(a) without passing through a phase transition. These phase diagrams have been shown to occur in mean-field[48] and renormalization group[49, 37] calculations to be discussed further in Chapter 4.

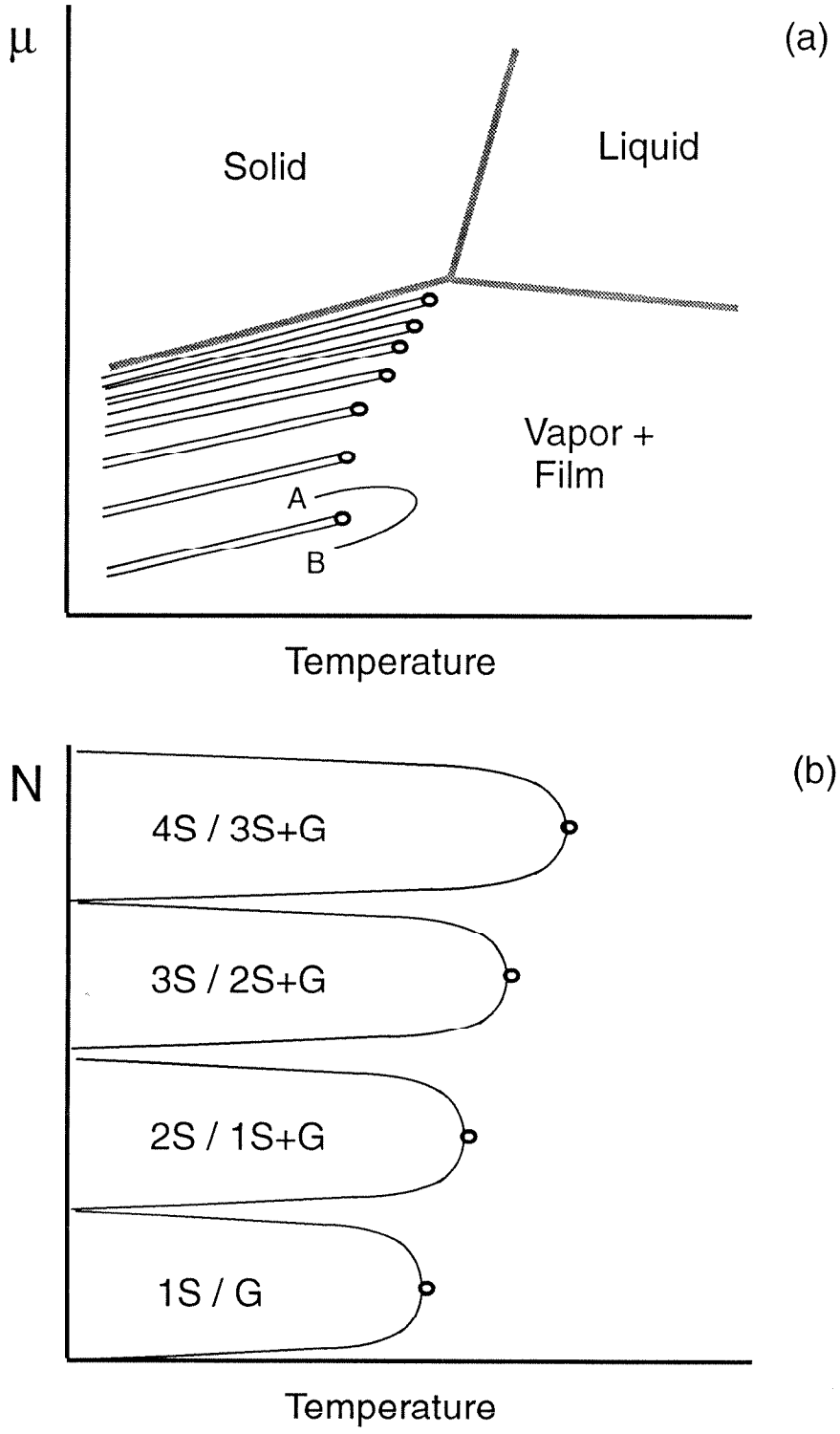

Figure 1.6: Phase diagrams of the lattice-gas adsorption model. (a) is the μ vs. T representation. Double lines are layering-transitions, and circles are layering critical points. (b) is the N vs. T representation. (N+1)S/NS+G means coexistence between dense and diffuse phases on top of N solid layers.

1.5 Observations of Layering in Heat Capacity Measurements

Whereas isotherm measurements increase film thickness at constant temperature, heat capacity scans increase temperature at nearly constant coverage. In this respect, heat capacity scans provide complementary information to the isotherm studies. According to Onsager's famous result, the exponent β governing the shape of the coexistence boundary is 1/8 for the two-dimensional lattice gas (Ising model), so the layering coexistence regions are expected to be very blunt-ended. For this reason, heat capacity experiments are expected to be of more utility in examining layering-transitions around their critical points. Zhang *et al.* [50]; Kim *et al.* [51]; and Chan *et al.* [52] found heat capacity peaks around the second-layer critical-point temperatures of C_2D_4 and CO on graphite that they interpreted as being due to the crossing of the coexistence boundary. They measured β to be .125 for C_2D_4 and .127 for CO in apparent agreement with the 2D Ising value, although the error bars were large. At higher coverages in C_2D_4, peaks were seen that were ascribed to the third, fourth, and fifth layering-transitions, although the rounded shapes of the coexistence boundaries were not apparent.

The positions of the layering critical points in argon for the second and third layer were found to be $T_{c,2} = 70.0 \pm 0.5$K and $T_{c,3} = 68.0 \pm 0.5$K from volumetric isotherms[53]. In a heat capacity study of multilayer argon, Zhu and Dash (ZD)[54, 30, 31] found a series of small heat capacity peaks around these temperatures at all coverages. No structure could be resolved in these peaks, but ZD did notice that some of the peaks were rounded, while others were sharp. They speculated that the sharp peaks were from scans passing close to layer critical points where the heat capacity is expected to diverge logarithmically by analogy with the 2D Ising model. The rounded peaks, they assumed, were from scans farther away from the critical densities where the critical behavior is expected to

be washed out.

The heat capacity study of methane on graphite by Lysek *et al.* [45, 46] added a complication to the simple multilayer phase diagram that had hitherto prevailed. This study observed triple points along the second, third, and fourth layering-transitions (Fig. 1.7). These triple points were interpreted as points at which 2D solid, liquid, and gas phases coexist in the topmost layer. The existence of these melting transitions implies that at least in methane, the topmost layer does not act like a lattice gas, because there is a change of symmetry between the dense and diffuse phases. A triple point had been observed previously in the second layer of CO on graphite[55, 52], and two-dimensional phases had been observed in the second layer of ^{4}He on graphite[56] and in the second layer of H_2 on MgO[57], but these results are not so surprising because the second layer has different symmetry properties than the upper layers[47] (this point will be discussed further in Chapter 5). Also, individual-layer melting transitions in argon and neon on graphite had been observed in the heat capacity study of ZD [54, 30, 31], but it was not clear how they tied into the multilayer phase diagram. The phase diagram for multilayer methane is shown schematically in Fig. 1.7. layering-transitions are shown with double lines. Layer melting transitions are shown with single, solid lines. Dashed lines indicate that it was impossible to trace where the melting transitions went, and it is unlikely that they simply end.

1.6 Ellipsometry Data

A series of very interesting ellipsometry studies were recently carried out by Youn, Hess, *et al.* [58, 59, 38]. These studies found a variety of phenomena in multilayer film systems and showed that deviations from the generic multilayer phase diagram are actually the norm. Ellipsometry is an optical technique that can probe the thickness of an adsorbed film by measuring the shift in the polarization

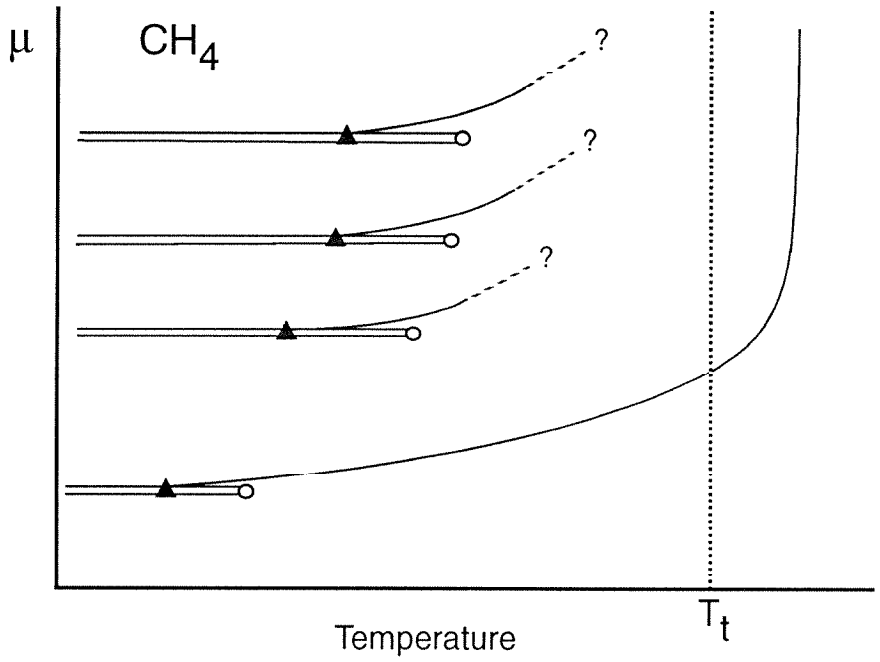

Figure 1.7: Schematic phase diagram for multilayer methane on graphite, showing layering-transitions (double lines) and melting transitions (single lines). The triangles are layer triple points. The first-layer melting temperature was found to increase beyond the bulk triple-point temperature, T_t, but the melting transitions for the higher layers could not be traced.

of light reflected from the film. Using this technique, the chemical potentials of the layering-transitions may measured by finding where the polarization of the reflected light changes abruptly with pressure. The method cannot be used to find melting transitions or other phase transitions that are not accompanied by a large change in density in the film. In argon and krypton, a particularly interesting phenomenon was seen. In these systems the steps in ellispometric isotherms were found to disappear at approximately where the layering critical temperatures were previously believed to be. However, at slightly higher temperature, the steps reappeared, shifted in coverage and chemical potential by around half a layer. Finally, at higher temperatures, but below the bulk triple point, the steps again disappeared. The heat capacity data taken during this study, described in Chapter 3, confirms the reentrant layering behavior and suggests other new phase

transitions in the multilayer region.

Chapter 2

Experimental Apparatus and Methods

The calorimeter used in this study was built by Mark Lysek, who was the graduate student in the Low Temperature Physics group at Caltech preceding me. The construction of the apparatus took several years. The goal was to build a calorimeter approximately one hundred times more sensitive than the one used by Lysek's predecessor, and this goal was met. I joined the LTP group toward the latter stages of the construction and participated in the experiment's development, and also in Lysek's study of CH_4 multilayer films. After I took over the operation of the experiment, and prior to the Ar, Kr and CF_4 work described in this study, the entire sample gas-handling system was rebuilt from scratch. However, the cryogenics and the instrumentation are essentially the same as that in Lysek's study.

In this chapter, a description of scanning ratio calorimetry and a brief overview of the experiment will be given. A much more expanded presentation may be found in Refs. [46] and [60]. The experimental procedures will be described, and noise in the data will be analysed at the scan rates and in the temperature ranges used in this study. Finally, I will describe the desorption correction used in the data analysis, which differs from the one used in the CH_4 study.

2.1 Scanning Ratio Calorimetry

Previous heat capacity studies of monolayer and multilayer films have used either discrete-pulse calorimetry or high-precision AC calorimetry. In the discrete-pulse method, a predetermined amount of heat is put into the sample cell, and the change in temperature is measured after equilibrium is reestablished. Because it is impossible to maintain the sample's environment at the sample temperature while it is changing rapidly, an unknown amount of heat is exchanged between the sample and its environment during the measurement. For this reason, discrete-pulse techniques are generally an order of magnitude less sensitive than the one used in this study.

In AC calorimetry, the sample heater power is varied sinusoidally, and the thermal environment is kept at fixed temperature. The heat capacity is derived from the temperature variation of the sample cell, and corrections that are due to the thermal link between the sample and its environment can be subtracted. The advantage of this technique is that elaborate thermal isolation for the cell is unnecessary. Long integration times can give very high-precision data. A disadvantage of the AC method is that to achieve high precision, the temperature must be stabilized at each point at which data are to be collected. Because of this requirement and the necessity of long integration times, each data point requires a considerable time investment.

Scanning calorimetry eliminates the need to stabilize the sample temperature for each data point, while keeping the sample at all times close to thermal equilibrium with the environment. Figure 2.1 illustrates a simple scanning calorimeter. The heat capacity of the cell is compared with a standard heat capacity (or comparison thermal mass, CTM). In the usual arrangement, the CTM is heated at a constant rate, and the temperature difference between the cell and CTM is measured with very high precision. The cell heat capacity follows by measuring the

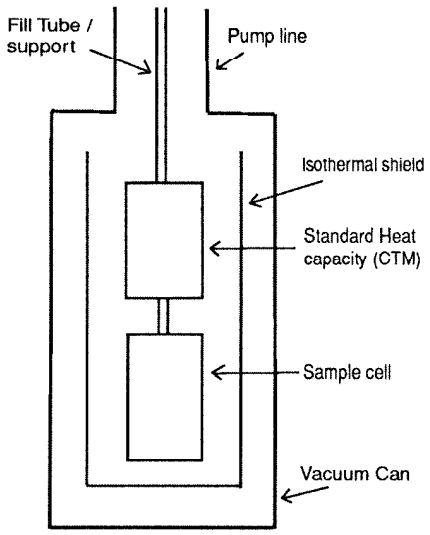

Figure 2.1: A scanning ratio calorimeter.

amount of heat needed to keep the cell at the same temperature as the CTM. Ignoring stray heat leaks, the differential equations for both bodies are

$$\frac{dT_0}{dt} - \frac{W_0 + K(T_1 - T_0)}{C_0(T_0)}, \tag{2.1}$$

$$\frac{dT_1}{dt} = \frac{W_1 - K(T_1 - T_0)}{C_1(T_1)}, \tag{2.2}$$

where T_0, C_0, W_0 and T_1, C_1, W_1 are the temperatures, heat capacities, and heat inputs to the cell and CTM, respectively, and K is the thermal coupling between the cell and CTM. For small K and $\delta T = T_1 - T_0$, we have

$$C_0 = \frac{W_0 C_1}{W_1 - C_1 \frac{d\delta T}{dt}}. \tag{2.3}$$

The heat capacity of the cell is just the ratio of heat inputs multiplied by the CTM heat capacity, with a small correction because of the difference in drift rates between the two masses. The equithermal shield surrounding the experiment is controlled at either the cell or CTM temperature, so that heat leaks are not only small, but very smooth. A similar arrangement, known as differential scanning

calorimetry, compares two nearly identical sample cells to each other, with the hope of cancelling stray heat leaks. That arrangement is not practical for adsorbed, multilayer film studies. The ratio calorimeter described here uses a CTM with a heat capacity approximately five times that of the cell, which makes the temperature control much easier. An analysis of the effect of stray heat leaks and errors in the temperature measurements was given in Refs. [46] and [60].

The advantage of scanning calorimetry is that by using moderate scan rates, large quantities of data can be accumulated in less time. The scan rate must be slow enough to ensure that the sample is close to equilibrium at all times. Non-equilibrium effects can be easily checked for by varying the scan rate. Slow scan rates improve the temperature resolution, approximately the scan rate multiplied by the thermal-relaxation time of the sample. Very slow scan rates are undesirable because the effect of stray heat leaks varies as the inverse of the scan rate. The scan rate used in most of this work is between $3/2 - 2$ Kelvin per hour to ensure that the sample is close to equilibrium while keeping the noise level low. The temperature resolution of a scanning technique depends on the thermal time constant of the sample cell. Lysek[46] estimated the time constant, on the basis of the thermal diffusivity of graphite, to be approximately three minutes. Using the relation

$$R = S \cdot T_{cell} \tag{2.4}$$

with $S = 3$ Kelvins per 2 hours, and $T_{cell} = 3$ minutes, we find that the resolution of the data is 75 mK, which compares well with the other techniques. In other systems, it has been shown that AC techniques can achieve much higher resolution. However, the applications of AC calorimetry to adsorbed films have always produced data of equal or less temperature resolution, and less calorimetric precision, than the scanning method used in this study.

2.2 The Experimental Apparatus

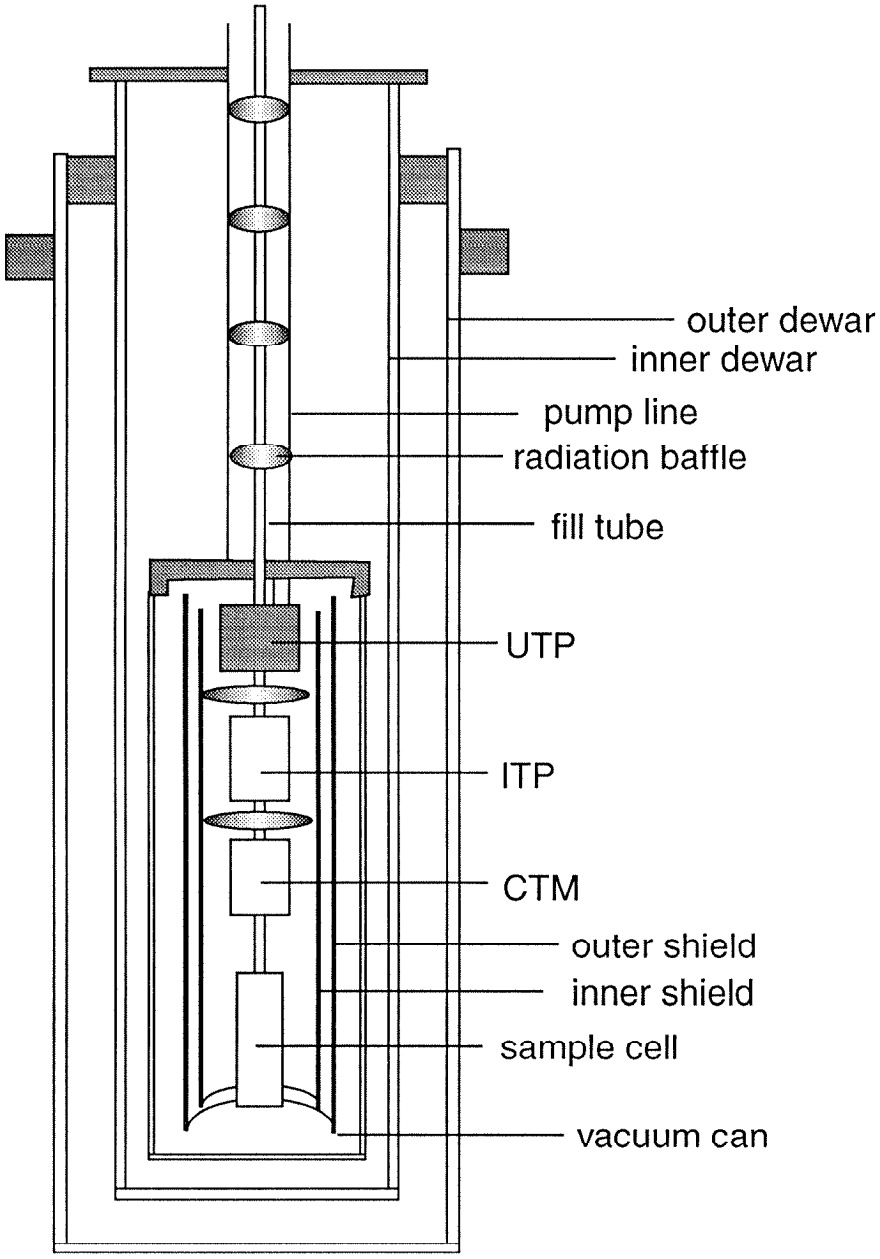

Figure 2.2: Schematic diagram of the calorimeter probe, vaccuum can, and cryogenic dewars.

Figure 2.2 is a schematic diagram of the calorimeter probe, vacuum can, and cryogenic dewars. The probe assembly consists of four thermal masses supported by the sample-gas fill line. The sample cell is filled with 28.9 grams of Union Carbide Grafoil Mat[8], which was outgassed at 1000 C untill the pressure was below 1×10^{-6} torr. The purpose of the CTM has already been described. A platinum resistance thermometer (PRT) on the cell measures its temperature. An additional PRT on the cell, and one on the CTM, measure the temperature difference between these two bodies. The upper thermal platform (UTP) serves as the thermal tie-down for the nearly one hundred wires needed for the thermometers and heaters. This body, controlled at about two degrees above the temperature of the CTM, serves to smooth out the large thermal fluctuations coming down from room temperature. The isolation thermal mass (ITP) is a second stage of thermal isolation that along with the inner and outer radiation shields, provides the thermal environment for the cell and CTM. Two thermal shields are used because thermal gradients may exist in the outer shield, which would otherwise be seen by the sample cell. The temperatures of the CTM, ITP, UTP, and shields are monitored with diode thermometers. Heaters on all the thermal masses plus the fill tube are made of evenohm wire wound non-inductively.

The calorimeter probe is enclosed in a vacuum can that may be evacuated to about 3×10^{-7} torr, using a liquid-nitrogen-trapped diffusion pump. Several radiation baffles are used to prevent room-temperature radiation from coming down the pump line. The inner bath is filled with a mixture of nitrogen and oxygen, to prevent freezing at the lowest attainable temperatures. This bath is completely closed off, to provide an additional layer of thermal isolation for the experiment. The pressure is monitored continuously by the computer. The outer bath is filled with liquid nitrogen and continuously pumped down to about 10 torr. The vacuum space to the inner dewar is filled with a small amount ($\sim 10^{-4}$ torr) of helium gas to provide a weak thermal link between inner and outer baths.

The reason for two baths, and for the static inner bath is that the outer bath must be filled during the course of the run, creating a huge thermal disturbance that might otherwise be noticeable in the heat capacity data. The calorimeter has been run as low as 62K using this arrangement.

2.3 Instrumentation and Interface

A block diagram of the instruments related to the heat capacity measurement is shown in Fig. 2.3. The three PRTs are labelled T0–T2, diode thermometers are labelled D0–D4, and the heaters are labelled H0–H5. The temperature difference between sample cell and CTM is measured using an AC Kelvin resistance bridge. Thermometers T1 and T2 make up two arms of the bridge, and a manual primary ratio transformer sets the ratio for null output across the bridge. A secondary ratio transformer is used to correct for the finite resistance of the copper wire between T1 and T2. The excitation frequency for the bridge is generated by a programmable frequency-phase board, that also provides the reference signals for the lock-in amplifier. The "excitation source" of the bridge converts the square wave into a sine wave at the same frequency with an amplitude that is set by the output of an 18-bit rate multiplier. The output of the bridge is amplified and filtered with a preamplifier located in the bridge chassis before being input to the lock-in amplifier. The output of the lock-in is digitized using a voltage-to-frequency (V/F) converter, opto-isolated, and then read by a 16-bit counter that is interfaced to the metrabus isolated computer interface. Much of the interfacing is done using the same V/F converter scheme for digitizing analog signals. The advantages of this arrangement are that V/F converters are much less expensive than (14-bit) D-A converters; they require only one opto-isolator to isolate ground signals; and their output represents a true integral of the analog input over the time interval counted. This scheme, of course, is suitable only for slowly varying

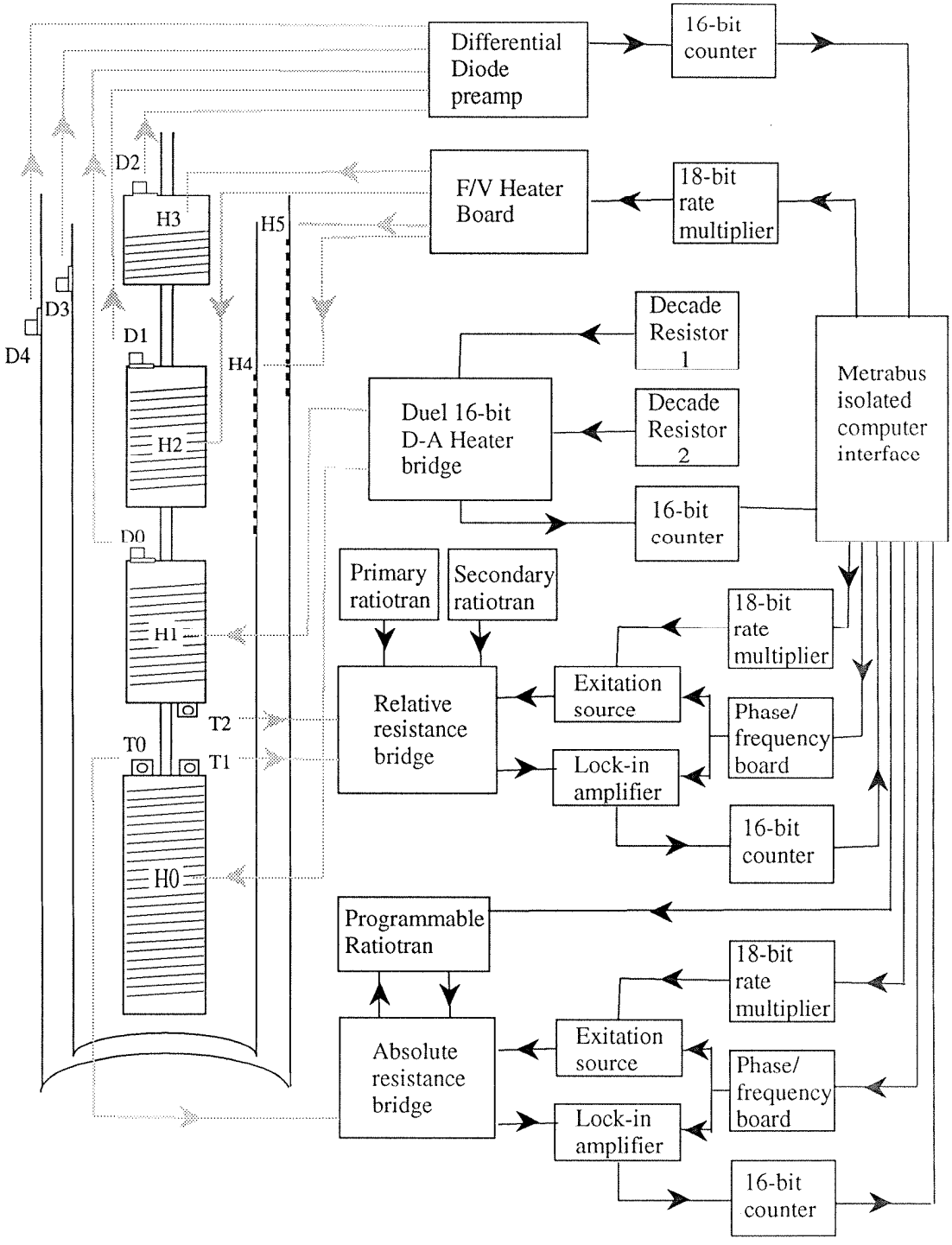

Figure 2.3: Block diagram of the instrumentation related to the heat capacity measurement.

signals.

The absolute resistance bridge, used to measure the temperature of the sample cell, is a modification of an active, 4-wire A.C. resistance bridge devised by A. C. Anderson. The bridge uses only one programmable ratio transformer, and is completely automated by the computer. The bridge excitation and measurement of the off-balance signal are handled in the same way as for the relative bridge. During operation, the computer adjusts the ratio-transformer ratio to stay close to balance, and every 10 minutes the ratio is tweaked to produce a two-thirds full-scale output in order to recompute the bridge sensitivity. To reduce the susceptibility to room-temperature fluctuations, the bridge circuit is mounted inside of a copper box, inside a styrofoam box, inside an aluminum chassis. The copper box is temperature controlled to within ± 0.1 K so that the standard resistors remain stable to .5 ppm. The noise in the bridge output corresponds to a noise in the temperature measurement of about 25 μK at 100K.

The temperatures of the thermal bodies used to provide thermal isolation for the calorimeter are measured, using silicon diode thermometers. Instead of trying to measure each diode independently and then subtracting from the CTM diode output to produce a control signal, the voltages across diodes D1–D4 are subtracted in the hardware from the voltage across the "master" diode D0. The difference is digitized with the same F/V converter to a 16-bit counter scheme, and read by the computer. The temperature of the CTM is measured by comparing the voltage across diode D0 to that of a 16-bit D-A converter controlled by the computer. The computer determines the temperature from the output voltage using a $4^{\underline{\text{th}}}$ order, Chebychev-polynomial fitting function. Using a proportional-integral-derivative (PID) feedback algorithm, the computer is able to control the temperatures of the ITP, UTP, and shields to within 0.5 mK of their setpoints relative to the CTM. Commercial temperature controllers may be able to provide better absolute accuracy, but this circuit can provide much better relative

temperature stability, and therefore better thermal isolation for the experiment.

The largest term in the equation for the heat capacity is the ratio between the power put into the cell and CTM heaters, so these quantities must be known to as high an accuracy as possible. In order to measure the heater resistances continuously during operation, each heater is one arm of a D. C. Kelvin resistance bridge. The voltages of the bridges are set by the computer using two Digital to Analog (D/A) converters. The resistance of the heater is compared to that of a decade resistance box. As with the other bridges, the heater bridges are operated in the off-balance mode, so that the heater resistance is derived from the voltage across the bridge. Given a desired power output, the computer calculates the voltage to be applied to the heaters each 1/2 second from the resistance calculated during the previous 1/2 second interval. The power outputs to the cell and CTM are known to at least $\pm.005\%$.

Because it is not necessary to know exactly the power output of the heaters on the bodies providing thermal isolation, frequency to voltage converters are sufficient because they are linear to .02% and are easily interfaced. The computer provides the frequency for each channel, using an 18-bit rate multiplier. An F/V converter generates the desired voltage, which is then input to a two-pole, low-pass filter to remove high-frequency components, and then to a current-booster circuit that drives the heaters. A digitally controlled switch allows the computer to choose between four voltage ranges, providing fine control for all circumstances.

Apart from the instruments already described, the computer is interfaced with two room-temperature thermometers, a Barocel pressure meter, an ion gauge controller, two cryogenic-liquid level sensors, and several automatic valves for the gas-handling system, a heat switch, and the bath filling. The software used to read and control all of these devices consists of three main parts. First, control routines devoted to each of the instruments are written in the "C" language and compiled. These routines run in the background and are coordinated using a non-preemptive

multitasking kernel adapted by Lysek[61]. The instrument-handler routines are awakened and run every half second by an externally generated interrupt signal. To control the sequencing of an experiment, at a higher level, Lysek developed a special purpose reverse polish notation (RPN) language interpreter. This is a stack-oriented language that provides the control structures and commands that run a given type of experiment. The interpreter also runs in the background and communicates with the instrument handler routines via a "status-variable display structure" that resides in a commonly accessible block of memory. Finally, a foreground user interface allows access to the RPN command file, the interpreter stack, and the "status-variable display/editor." The experiment software allows experiments to be run with a high degree of reproducibility, while making it very easy to change the experimental procedures and parameters.

2.4 Sample Gas Handling System

Because the gases used in this study are available with very high purity (99.9995% for argon and 99.9999% for CF_4), a new, ultrahigh purity, automated, sample gas handling system (GHS) was constructed. Figure 2.4 is a schematic drawing of the gas handling system. Valves are denoted by circles with crosses. Those valves equipped with air actuators for automatic operation are shown with a rectangle over the circle.

The main part of the GHS was built inside an oven that allows a periodic "bakeout" of any impurities in the system while under high vacuum. Five of the valves inside the oven are of all-metal construction, allowing a bakeout of up to 350 centigrade. The other (leak) valve is also of all-metal construction and can actually be baked to an even higher temperature. All permanent vacuum joints, except for a few that do not come into contact with sample gas, were made with welds. All others were made with silver solder. Other vacuum joints were made

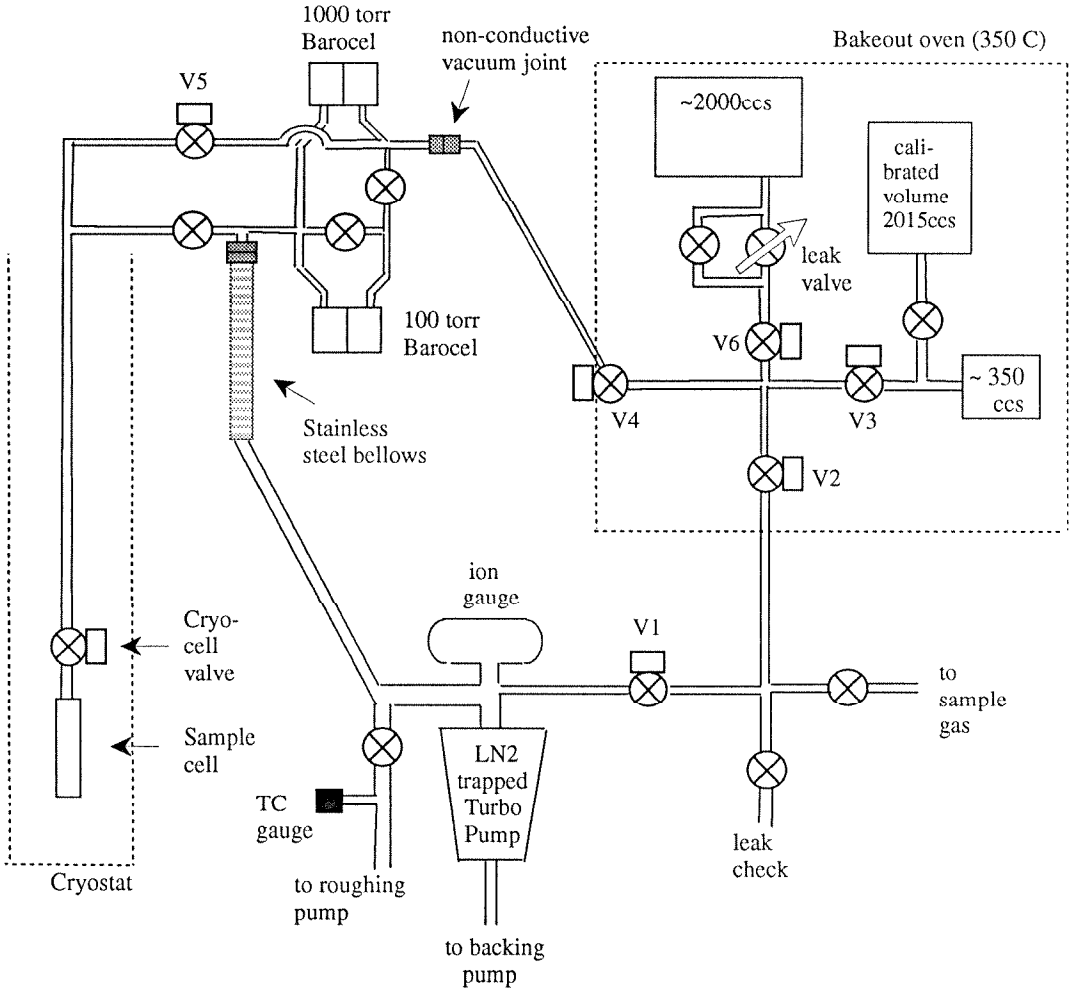

Figure 2.4: Automated ultrahigh purity gas handling system

using Cajon VCR[62] fittings with silver-plated nickel gaskets. Three stainless-steel cans are used to store and measure quantities of gas. The first (2015 cm^3) is the primary calibrated volume from which all the other volumes in the system are measured. A second, smaller volume is connected as shown in the diagram, so that one automatic valve may access either $\sim$ 2390 cm^3 or $\sim$ 375 cm^3 volumes. A third volume is connected to a variable leak valve and an automatic valve to meter out precise quantities of gas during isotherm runs. All of the automatic valves inside the oven are normally open so that the cell will be open to as large a volume as possible in the event of a power failure. Because the actuators contain viton and must be removed during bakeout, one of these valves, V4, was mounted with its air actuator outside the oven, so that the valve could be kept closed. Otherwise, contaminants could collect in the line leading up to the barocels.

Because the barocel heads are not bakeable, they are mounted on a heavy (for temperature stability) aluminum board external to the oven. A 1000 torr barocel is always connected to the system, to minimize the number of valves. The 100-torr head may be shut off from the system with a soft-seated bellows valve for operating at high pressures. The scaffolding supporting the cryostat and barocel heads is electrically isolated from the rest of the system in order to prevent ground loops through the pipes. The one electrically non-conducting vacuum joint in the part of the GHS open to the sample gas was made using a kel-F gasket and a Cajon VCR-style, female restraining nut made of some hard brown material we found lying around the lab. A separate, large-diameter line goes from the pump to the sample cell, for the purpose of pumping out the cell. The non-conducting vacuum joint on this line was made using a pair of KF flanges with a viton O-ring and one insulating support made of the brown material.

To test a gas handling system, it is necessary to perform an outgassing test by closing off the pump from the system and measuring the leakup rate. After the initial bakeout, the leakup rate of the sections of plumbing inside the oven was

immeasurable using the barocel. The leakup rate of the barocel heads themselves, however, was found to be around 1 mtorr/ 2 hours into a volume of 50 cm^3, corresponding to 3×10^{-5} stpccs/ hour. At this rate, the sample gas should remain sufficiently pure over the course of a typical experiment.

2.5 Experimental Procedures and Data Reduction

The grafoam substrate used in this study was the same as was used by Lysek in his study of methane. The grafoam was initially prepared by outgassing at 1000C until the pressure was below 10^{-6} torr, after a 1500C heating in a chlorine atmosphere when it was manufactured. After the methane study, the sample cell was raised to room temperature and disassembled in order to fix a leak. After reassembling, the cell was pumped for several days, until the pressure was below 3×10^{-7} torr, to remove as much contamination as possible. Between the argon and krypton studies, and also between the krypton and CF_4 studies, the cell was warmed to 120K, where it was pumped to below 3×10^{-7} torr. The sharpness of the heat capacity peaks found in Kr and CF_4 was taken as evidence that this procedure removed a sufficient amount of the previous sample gas.

Most heat capacity runs in the argon study were taken between 62K and 90K. The upper temperature limit was imposed by high vapor pressure of argon at around 90K. Pressures higher than about 1200 torr cannot be tolerated for fear of damaging the barocel head. Using a 10000-torr head would not solve this problem because the maximum pressure sustainable by the sample cell would soon be reached. Runs at lower coverages, where the vapor pressure is much lower than bulk-saturated vapor pressure, could be extended to slightly higher temperatures. Heat capacity runs for krypton were made between 80K and 120K, and runs for CF_4 were between 64K and 120K. The krypton runs (except for a few exploratory

runs) were not extended to lower temperature, because it takes a very long time to cool the calorimeter when its temperature becomes close to the bath temperature.

The scan rate used for argon was 3K/ 2 hours, because of the relatively narrow temperature range studied. The scan rate for krypton and CF_4 was 2K/ hour, which was the same as was used in the methane study. The next section gives a comparison of the noise in the data taken at different scan rates. For all of the heat capacity runs, the sample cell is controlled at between 50 and 150mK below the temperature of the CTM, accomplished by setting the relative bridge ratio-transformer ratios to .49920 and controlling the sample cell temperature to null the bridge. As the calorimeter warms, the temperature difference between cell and CTM will change by about 0.1K, because the platinum thermometers of the relative bridge have slightly different temperature versus resistance characteristics, but this effect is not noticeable in the data. The ITM was controlled, for all runs, at .1 K above the CTM, and the UTP was controlled at 2K above the CTM temperature. The purpose of the temperature gradient through the calorimeter is to insure that at all times, the cell is the coldest part of the system, to prevent condensation of vapor in the fill tube. The UTP was controlled as far as it was above the CTM in order to improve the reproducibility of the data at the lowest temperatures accessed in the argon study. At temperatures below about 66K, it was impossible to keep the UTP closer to the cell temperature, once the helium exchange gas was removed from the vacuum can, because of the large heat load coming down the wires and the fill tube, from room temperature. The UTP would warm faster than the chosen scan rate, leading to irreproducible thermal gradients. It was found that it was possible to keep the UTP under control at about 2K above the CTM, so a reproducible thermal gradient was tolerated. This compromise was made because the data are analyzed more for small deviations from a smooth background rather than in terms of the absolute accuracy of the background itself.

Films of a precise coverage were formed by opening the cell to the calibrated volume and cooling until a predetermined quantity of gas was left outside the cell. For the majority of the runs in this study, we wanted to keep the system on the adsorption branch of the capillary-condensation hysteresis loop (see Section 3.1). Accordingly, films were always formed by adding gas to the system, never by removing gas. Of course, a certain amount of gas always leaves the film because of thermal desorption during the course of a heat capacity scan, but this cannot be helped. The film-forming program first precooled the cell, open to the barocel but not the calibrated volume, until the vapor pressure was about 1 torr below that of the gas stored in the calibrated volume. The calibrated volume valve was then opened, and the cell cooled, until the number left in the volume, the manifold, and the fill tube, subtracted from the total number in the system, was equal to the desired film coverage. Films were routinely formed in this way to within about 1 stpcc (1/200th of a layer) of the target coverage. In the case of CF_4, the vapor pressure in the temperature range of interest was much too low to use this procedure. In that study, films were formed by dosing, admitting a quantity of gas to the manifold, shutting off the volume, and then opening to the cell. Using this method, it was much more difficult to produce films of a prechosen coverage.

At the completion of the filling sequence, the cryogenic cell valve located just above the UTP was closed, and the film was rewarmed to 90K for argon and 120K for krypton and CF_4. The purpose of this annealing process is, in part, to raise the vapor pressure high enough to ensure that the adsorbate is able to diffuse throughout the cell, so a uniform film may be formed. The other purpose of the anneal stage is to start the final cooldown at the same temperature every time for better reproducibility. As the vapor pressure of CF_4 at 120K is only 100 torr, the data taken in that study may be slightly less reproducible than in the Ar and Kr studies. The sharpness of heat capacity features in CF_4, however, suggest that the

films formed were just as uniform as the Ar and Kr films, which were annealed at over 1000 torr. After the anneal, the sample cell was recooled according to a power-law temperature versus time protocol. The temperature of the cell was controlled during cooldown, so that the cooling rate satisfied

$$\left|\frac{dT}{dt}\right| < C(t_1 - t)^3, \tag{2.5}$$

where t_1 is the final time, and C is a constant. Any cooling schedule that slows the cooling rate at low temperature where diffusion times are large should aid in the formation of uniform films. The constant, C, was chosen to produce a minimum cooling time of 12 hours. For scans starting below about 70K, the actual cooling time was often more than 24 hours.

Except for the various types of calibration runs, the other measurements commonly performed with the apparatus were the upwards and downwards isotherm measurements. The purpose of an isotherm, as described in Chapter 1, is to measure the vapor pressure versus number adsorbed in the system. The program used for the isotherm measurement makes use of the experiment's ability to automate complex, repetitive tasks. The upwards isotherm program measures out doses of a precise amount by opening valve V6 (Fig. 2.4) with the fill-tube valve, V5, closed, and waiting until the pressure leaks up to a calculated value. The cell is precooled (by admitting helium gas into the vacuum can) by about .3K before V5 is reopened, because the cell temperature will rise when the cell is dosed. After the dose, the temperature is recontrolled at the isotherm temperature by increasing the cell setpoint according to an exponential temperature-versus-time rule. After the isotherm temperature is reached, the program enters a loop while it waits for the film to reach equilibrium. Every 10 minutes the pressure is read and compared with the last measurement. If the pressure has remained constant to a preset tolerance, the program leaves the loop. During the loop and the subsequent measurement phase, the temperature is controlled at the setpoint to better than

0.5 mK. If the temperature rises by more than that amount, a short burst of helium gas is allowed into the vacuum can and then immediately pumped out. The measurement phase consists of 10 minutes over which the pressure is measured, and then the process starts over. Downwards isotherms are conducted in much the same way, except that gas is expanded from the cell into the manifold or small volume and then pumped out. The isotherms conducted in this way typically take about one week to 10 days to perform. Because of the computer automation, these are some of the most complete isotherms (the most experimental points) ever recorded.

The data from the heat capacity and isotherm programs are stored in binary files of from three to seven megabytes. Along with the data items required to make the relevant measurement, many other data items, such as shield temperatures and the bath pressure, are recorded for the purpose of debugging at a later time. Data items are measured every 1/2 second, but then are averaged over a second and a half before being recorded. The heat capacity is calculated according to Eqn. 2.3, using a series of data-reduction programs. The heat capacity of the bare sample cell, measured during a separate background run, is then subtracted from total heat capacity to obtain the film heat capacity. The background heat capacity is fit to a fourth-order polynomial to avoid adding noise to the data.

Vapor pressures are averaged over time intervals of about three minutes, by fitting to a least-squares line over the time interval. The pressure and its time derivative, the slope of the least-squares line, are reported at the midpoint of each interval. The chemical potential at each point is calculated from the nearly ideal gas formula,

$$\mu = k_B T \ln \left[\frac{1}{k_B} \left(\frac{2\pi\hbar^2}{m k_B} \right)^{3/2} \frac{P}{T^{5/2}} \right] + B(T)P, \tag{2.6}$$

where B(T) is the second virial coefficient, k_B is the Boltzman constant, m is the molecular mass, P is the pressure, and T is the temperature. For a non-monatomic

	Ar		Kr	
	$T < T_t$	$T > T_t$	$T < T_t$	$T > T_t$
A_0	-9.55992×10^2	-1.0294×10^3	-5.75267×10^2	-4.8970×10^2
A_1	1.76558×10^1	2.2749×10^1	7.70741×10^1	6.9688×10^1
A_2	0.0	-6.9464×10^{-2}	0.0	0.0
A_3	0.0	2.3063×10^{-4}	0.0	0.0

Table 2.1: Saturated vapor-pressure fit coefficients

gas such as CF_4, a rotational contribution should also be added. The chemical potential of the film must be equal to the chemical potential of the vapor, because the system is in thermal equilibrium. For computing $\mu - \mu_0$, tabulated values for the bulk saturated vapor pressure were used[63]. The tabulated values were fit to the form

$$P_{sat}(T) = e^{A_0/T + A_1 + A_2 T + A_3 T^2}. \tag{2.7}$$

The fitting coefficients used are given in Table 2.5.

2.6 Background Runs and Noise in the Heat Capacity

Background runs are used to calculate the bare sample cell plus substrate heat capacity as well as the CTM heat capacity. The background runs also allow for computation of the various figures of merit that apply to the heat capacity data. The three background runs, shown in Fig. 2.5, were made at scan rates of approximately 2K/hour, 3K/2hours, and 1K/hour, corresponding to constant CTM heater outputs of 0.045, 0.034, and 0.0225 watts. The data from runs with different scan rates agree only to a few percent. These data are the only available means to test the absolute accuracy of the heat capacity measurement. Background data from scans using the same scan rate agree much more closely, to about .1%[46], so it is likely that the disagreement between the curves shown in the figure is due to heat leaks. The absolute accuracy of the data is not

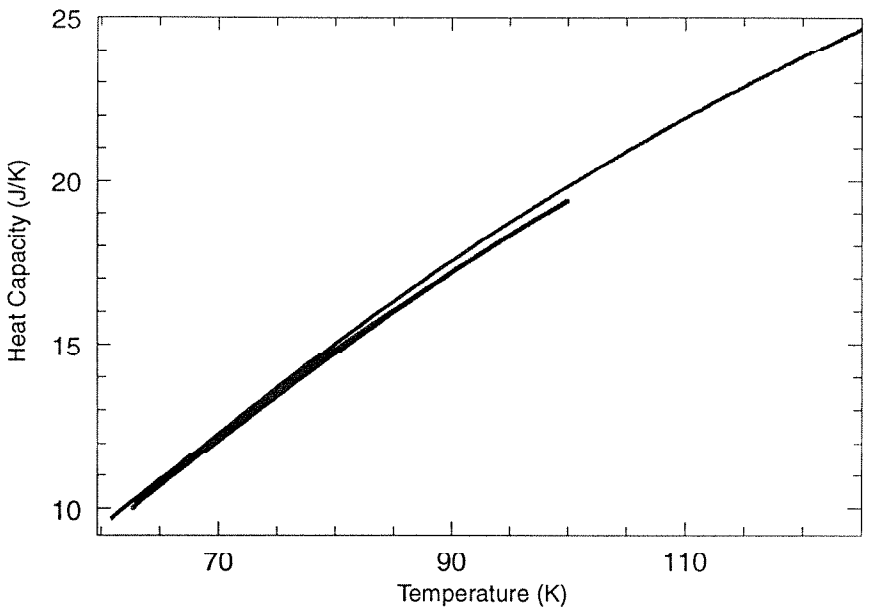

Figure 2.5: Background heat capacity of the sample cell for three different scan rates.

important, because the data are always analyzed in terms of small deviations from the baseline. The estimated, absolute accuracy of a few percent is actually better than that estimated for other heat capacity studies of adsorbed films (which typically cite about 10% absolute accuracy). The difference between the results at different scan rates makes it necessary to perform a background run at each scan rate used to take data. As the film heat capacity is only about 10% of the background, subtracting a background scan with a 2% error would cause an error in the film heat capacity of 20%.

The scatter in the data may be found by subtracting the raw data from a background run from a fit to those data. The scatter in the background runs at the three different scan rates is shown in Fig. 2.6. As was expected, the run at the slowest scan rate shows the most scatter. Also apparent is a steady increase in the noise level with temperature. This behavior is not fully understood. The percent RMS deviation of the data, which is a measure of the sensitivity of the calorimeter,

is shown in Fig. 2.7. These plots were made by integrating the raw data of Fig. 2.6 over 1 degree intervals and taking the root mean square. The lines are linear fits to the result. It is found that the sensitivity varies from around .02%, at low temperature to about .045% at higher temperature. The sensitivity also varies inversely with the scan rate. At 75K, the sensitivities are .020, .025, and .039%, for the scan rates of 2K/hour, 3K/2hours, and 1K/hour. The middle scan rate represents a reasonable tradeoff between sensitivity and temperature resolution. Increasing the resolution with the 1K/hour scan rate decreases the sensitivity markedly.

2.7 Desorption Correction

A large part of the heat capacity signal at higher temperatures, where the saturated vapor pressure is high, is due to desorption of the film. As the temperature increases, atoms leave the film and enter the vapor, so additional heat, equal to the heat of desorption per atom, must be put into the sample cell. The heat of desorption, q_d, is defined by

$$C_0 = C_{film} + C_{gas} - q_d\left(\frac{\partial N_{film}}{\partial T}\right)_{N_0},$$

where C_0 is the total measured heat capacity with the sample cell and bare substrate heat capacities subtracted, and N_0 is the total amount of krypton in the system, film plus vapor. Thus,

$$q_d = T\left(\frac{\partial S_{gas}}{\partial N_{film}}\right)_T - T\left(\frac{\partial S_{film}}{\partial N_{film}}\right)_T,$$

where $S_{gas(film)}$ and N_{film} are the entropy of the gas (film) and the amount adsorbed. The entropy of the gas may be calculated from the virial equation of state. To calculate the film term we use the Maxwell relation:

$$\left(\frac{\partial S_{film}}{\partial N_{film}}\right)_T = -\left(\frac{\partial \mu}{\partial T}\right)_{N_{film}}.$$

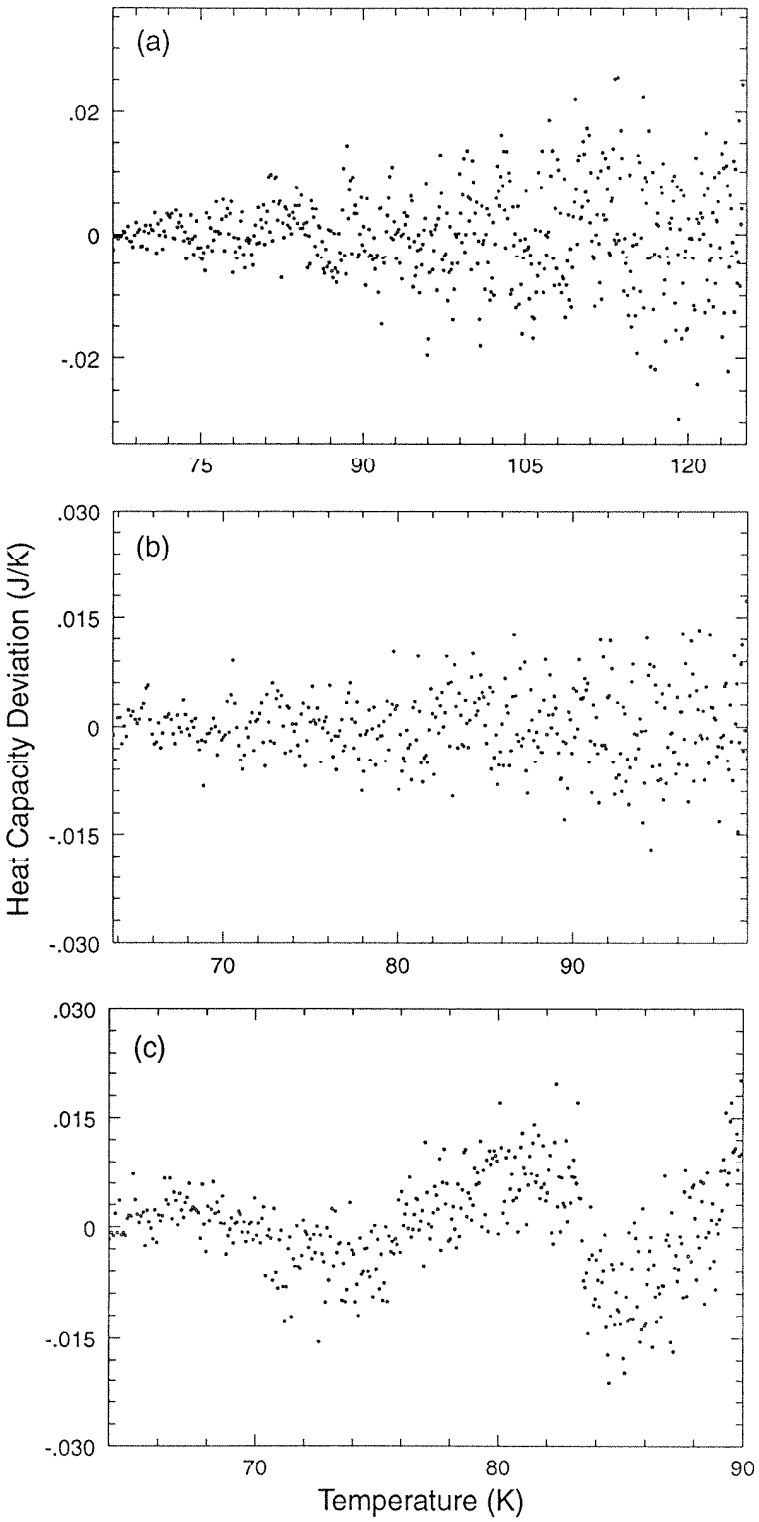

Figure 2.6: Scatter in the heat capacity data from background runs at (a) 0.045 watts, (b) 0.034 watts, and (c) 0.0225 watts

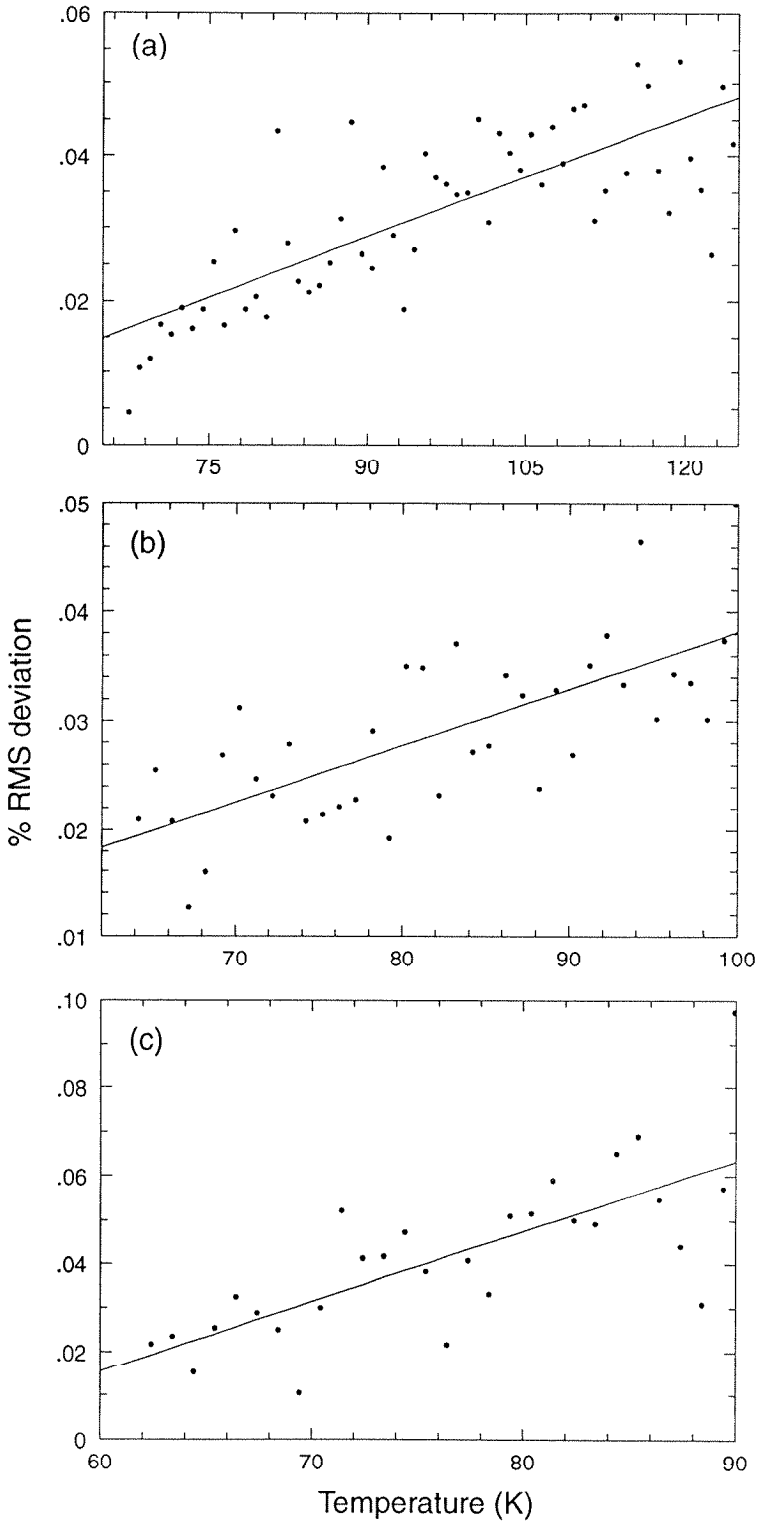

Figure 2.7: Percent RMS deviation in the heat capacity data at scan rates of (a) 0.045 watts, (b) 0.034 watts, and (c) 0.0225 watts.

This quantity may be calculated exactly if isotherms at closely spaced temperatures are available. In the present situation, we only know μ along the experimental paths of constant N_0. We have found the approximation

$$\left(\frac{\partial \mu}{\partial T}\right)_{N_{film}} \approx \left(\frac{\partial \mu}{\partial T}\right)_{N_0}$$

to be adequate for our purpose. This approximation produced better results than the Frenkel Halsey Hill approximation[2, 3]

$$\left(\frac{\partial \mu}{\partial T}\right)_{N_{film}} \approx \left(\frac{d\mu_0(T)}{dT}\right)$$

where μ_0 is the bulk saturated chemical potential.

To avoid adding noise to the desorption corrected data, the correction for each scan was fit to a polynomial over the entire temperature range. The purpose of this procedure is to subtract the large desorption background in order to present more clearly the sharp peaks due to phase transitions in the film. It should be noted that part of the film heat capacity peaks may be due to desorption, because a phase transition in the film that results in a change in density may cause atoms to desorb. This contribution to the heat capacity peaks is not subtracted when the correction is fit to a smooth function.

Chapter 3

Results

This chapter contains the results of 132 heat capacity scans and two volumetric, isotherm measurements of argon and krypton on graphite. The isotherms are used mainly to characterize the two adsorption systems, so the results of these measurements are presented first. The heat capacity scans are used to study two forms of condensed matter present in the system: capillary condensate and film. The heat capacity peaks that are due to the melting of the capillary condensate were the focus of previous studies, where they were erroneously believed to be due to the melting of the film. For the first time in these two systems, the positions of these melting peaks are measured in the temperature vs. chemical potential plane, and the data are compared to a simple theory predicting the melting curve of capillary-condensed matter[64]. Finally, data are presented showing layering and layer-by-layer melting transitions in both systems. The multilayer phase diagrams are drawn for up to the sixth film layer. Comparison with theoretical models of film behavior is made in Chapters 4 and 5.

The argon and krypton heat capacity scans presented in the figures of this chapter are labelled chronologically by ar## and kr##, respectively. The heat capacity scans for CF_4, presented in Appendix B, are labelled cf##. Appendix C lists information about each of the heat capacity runs.

3.1 Isotherms

Because complete upwards- and downwards-going isotherms each take approximately ten days to run, and because our system is not properly optimized for isotherm data, only one complete upwards- and downwards-going isotherm was measured in argon, and only one upwards-going isotherm was taken in krypton. Two isotherms were judged sufficient because pressure data were also taken simultaneously with the heat capacity data. The temperature of the argon isotherm was chosen to be 77K in order to try to confirm in a volumetric measurement the reentrant layering behavior found in YH's ellipsometry study approximately between 72 and 79K. For the same reason, the temperature of the krypton isotherm was chosen to be 102K. The inflection point of the first step of an isotherm is generally used to measure the monolayer coverage. According to this method, the monolayer coverages are 220 stpccs (centimeters cubed at standard temperature and pressure) for argon, and 260 stpccs for krypton. These quantities of gas are henceforth defined to be the "equivalent" or "nominal" layer for each system.

3.1.1 Wetting Behavior

The isotherms are shown in number versus pressure in Figs. 3.1 and 3.2. Arrows show the locations of steps. For the argon isotherm, a total of 3395 stpccs of gas (about 15.4 equivalent layers) were adsorbed into the sample cell in doses of 15–30 stpccs, starting from a bare substrate. At the completion of the upwards-going isotherm, one heat capacity scan was performed to measure the behavior of a very thick film. The downwards isotherm was taken, starting at the final coverage of the upwards isotherm, by withdrawing doses of 15–30 stpccs until reaching a coverage of 215 stpccs, slightly under one layer. The upwards and downwards isotherms joined exactly at a coverage of about 1.1 layers (relative pressure, $P/P_0 = 0.30$). For the krypton isotherm, a total of 3696 stpccs were adsorbed into the cell, using

doses of the same size. Both isotherms show approximately the same behavior. The fourth and fifth steps in each system occur well over four and five total layers adsorbed, suggesting the presence of capillary condensation. At the maximum coverage of each isotherm, the pressure is still about five torr below the bulk-saturated vapor pressure. The data show that wetting in both systems occurs up to at least five layers because steps are observed. We cannot show that wetting occurs at higher coverages because of capillary condensation.

Figures 3.3(a) and 3.4(a) show the isotherms plotted as number adsorbed versus $(\mu_0 - \mu)^{-1/3}$ to demonstrate the effect of capillary condensation on the system. According to the Frenkel-Halsey-Hill theory, the isotherm should approximate a straight line (the dashed lines shown), but with steps at even intervals that are due to layer condensation. When capillary condensation is nucleated, the adsorption isotherm curves sharply upwards from the straight line. Once capillary condensation is nucleated in this system, the number adsorbed in pores is expected to vary approximately as the number in the film to the sixth power[65]. By fitting the argon isotherm in Fig. 3.3(a), it was found that the deviation from the straight line equals approximately the film thickness to the 5 ± 1 power.

The locations of the layering steps are shown in Table 3.1.1. The steps are located by finding the peaks in the derivative of the isotherm data shown in 3.3(b) and 3.4(b). The three highest steps are labelled $3\frac{1}{2}$, $4\frac{1}{2}$, and $5\frac{1}{2}$, because these steps correspond to the reentrant layering transitions in the YH's ellipsometry data[58]. The locations of the layering-transitions from the ellipsometry data are also shown in Table 3.1.1. The discrepancies are due to the accuracy of the pressure measurements and the values used for μ_0. Close to the bulk-saturated vapor pressure, small errors in P_0 will cause large errors in $(\mu_0 - \mu)^{-1/3}$. Because the experiment is not set up to measure P_0, tabulated values were used to calculate μ_0 in the table.

By considering the spacing between the steps $3\frac{1}{2}$ and $4\frac{1}{2}$ and between $4\frac{1}{2}$ and

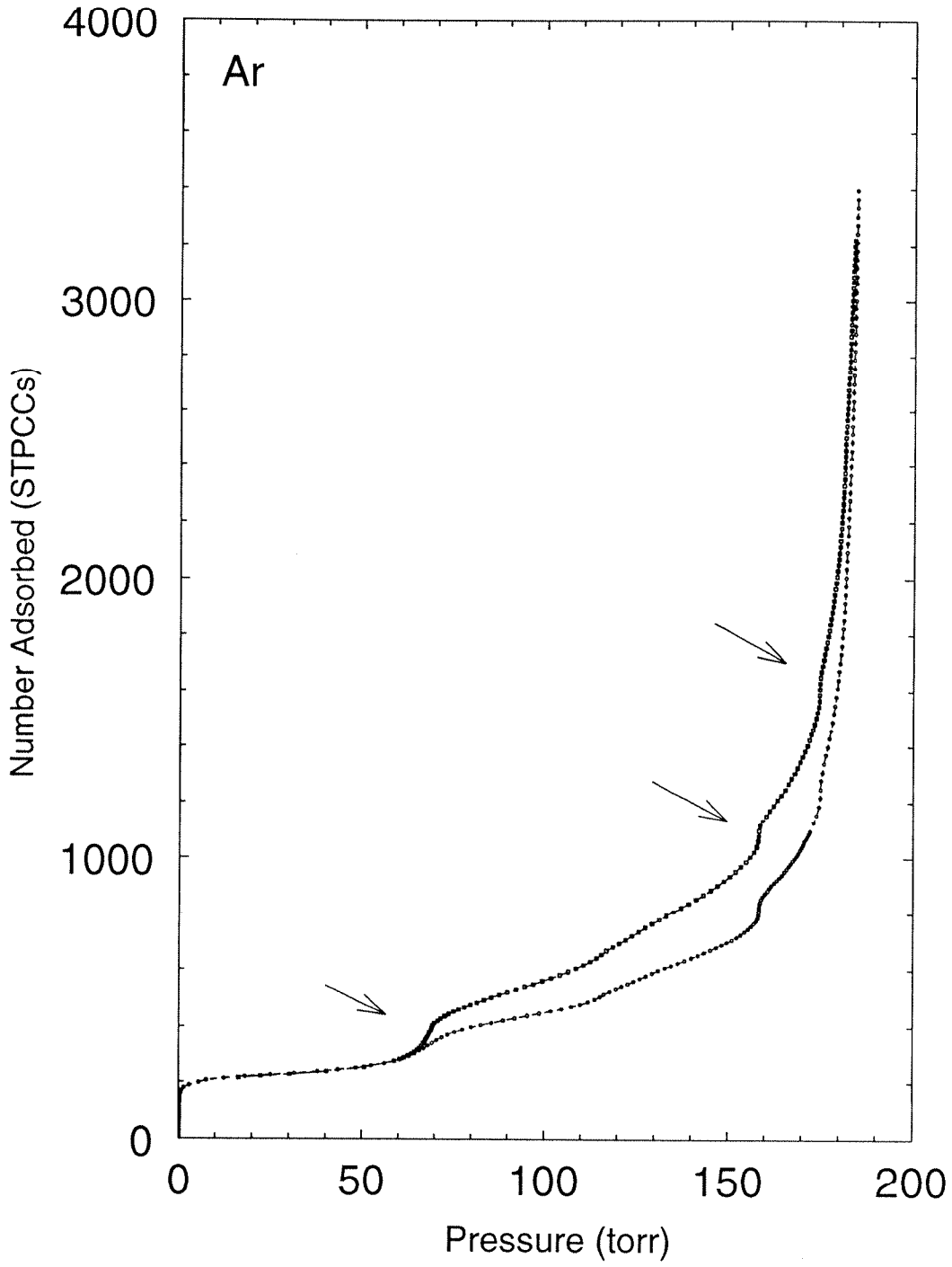

Figure 3.1: Argon isotherm at 77K. The lower curve is the adsorption branch, and the upper curve is the desorption branch. Arrows point to steps, the locations of which are the same on both branches.

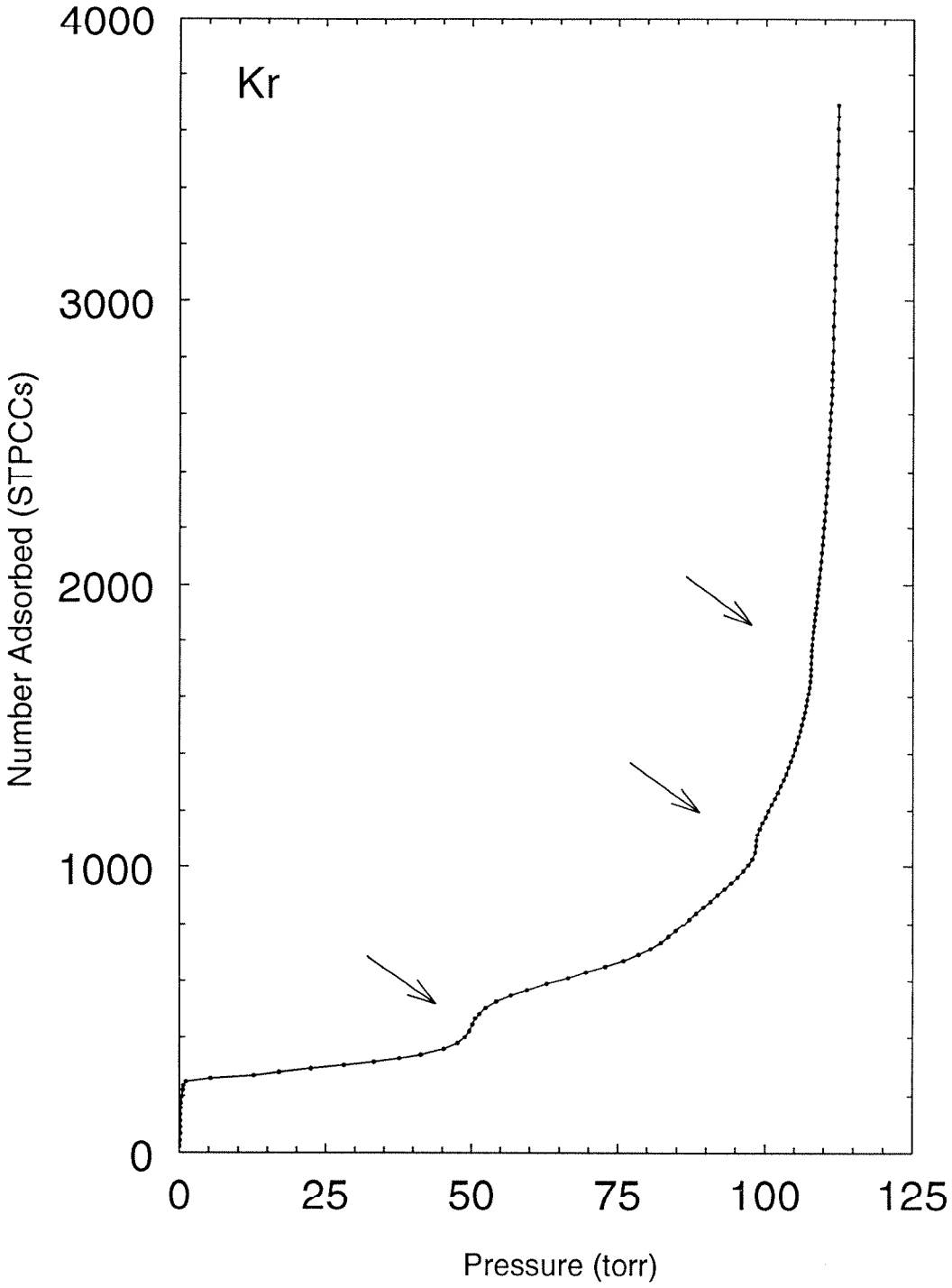

Figure 3.2: Krypton isotherm at 102K. Only adsorption branch data were taken. Arrows show the locations of steps.

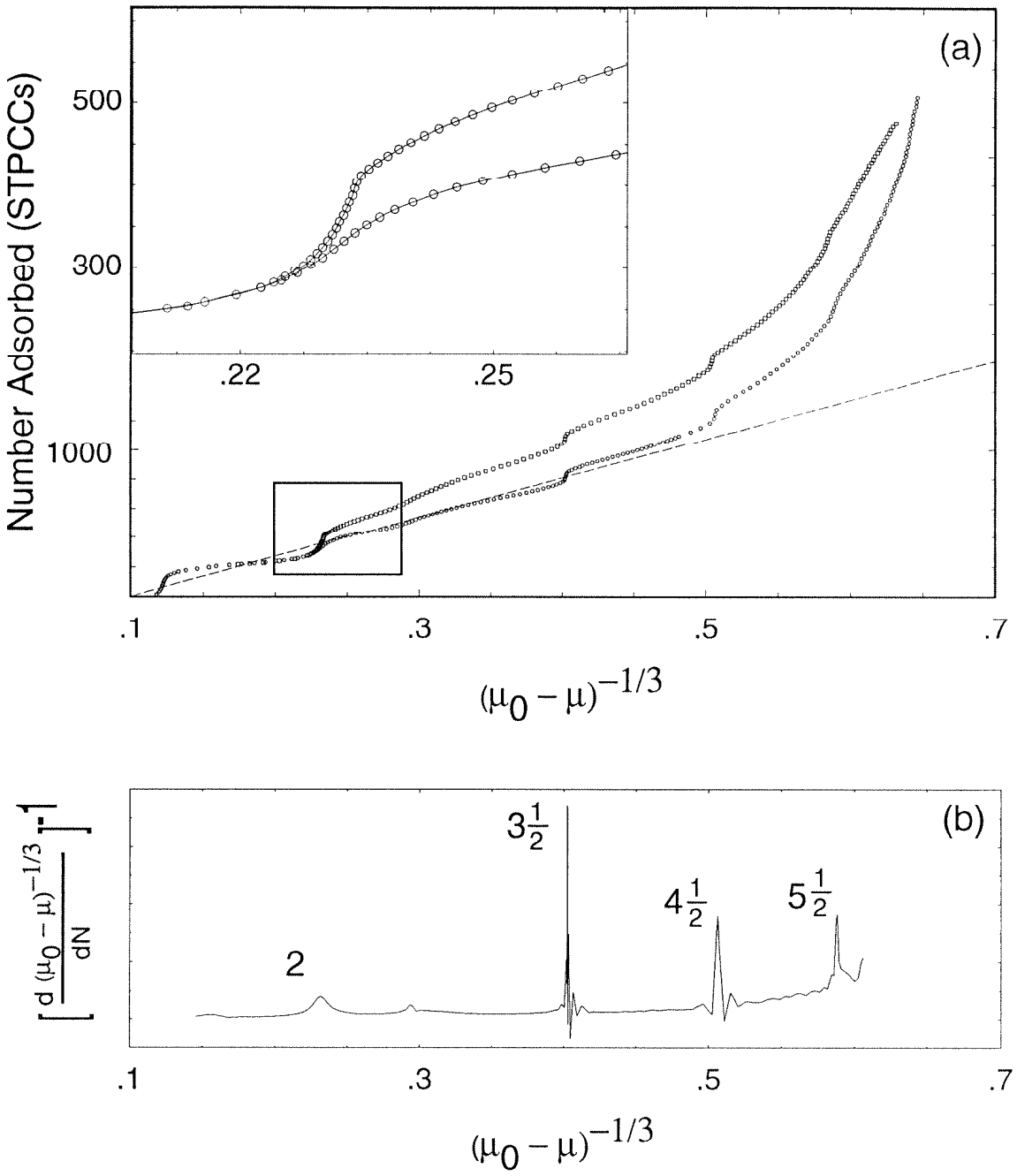

Figure 3.3: (a) Argon isotherm in μ versus N. The straight line is a fit to the low coverage data. The inset shows the two branches joining at about 1.1 layers. (b) Derivative of the adsorption branch isotherm data shown in (a) (in arbitrary units).

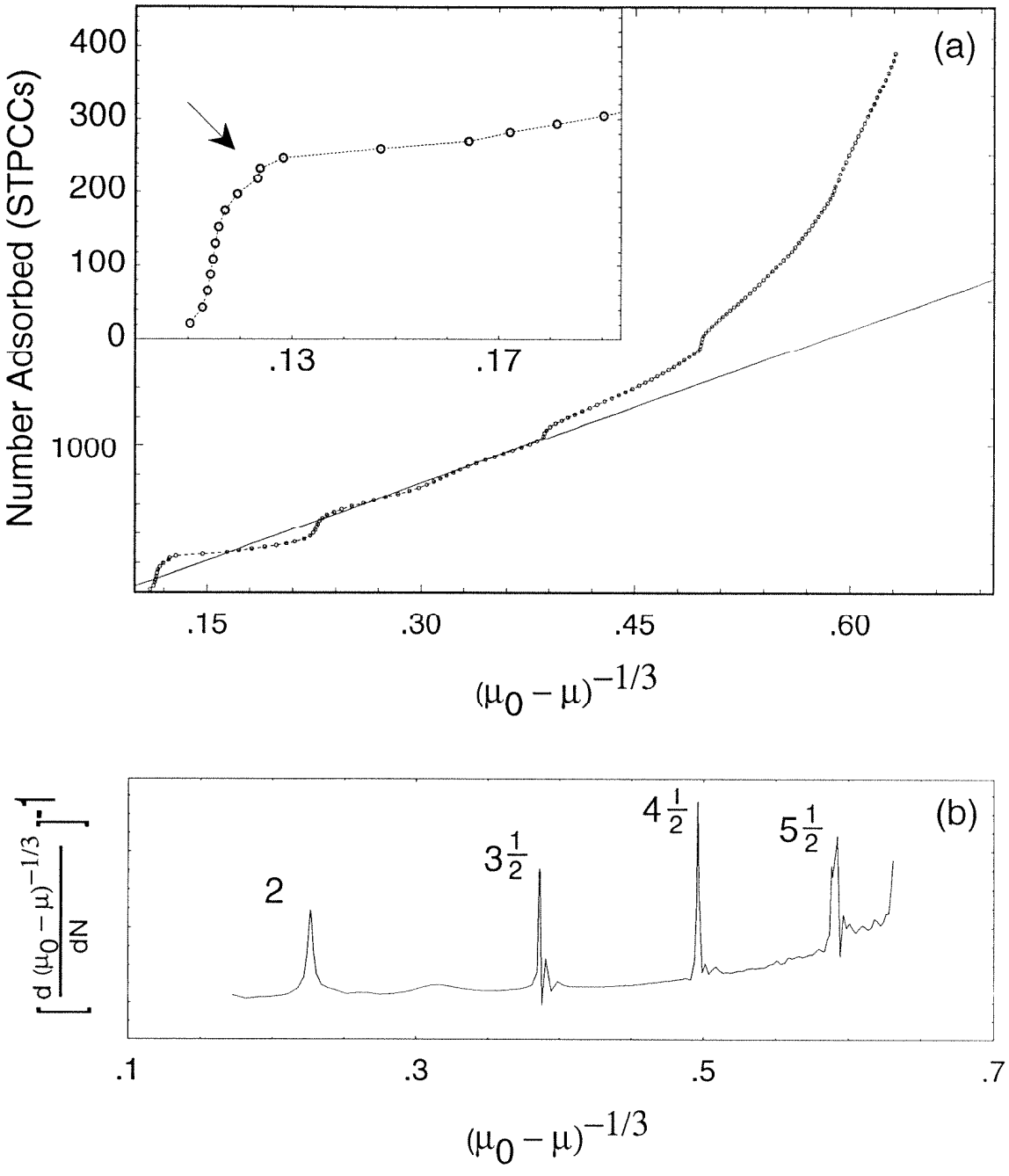

Figure 3.4: (b) Krypton isotherm in μ versus N. The straight line is a fit to the low coverage data. The inset shows the small notch in the first layer step that is due to the transition from registered solid to HD solid.

	Ar		Kr		YH: Ar
step #	$(\mu_0 - \mu)^{-1/3}$	(FWHM)	$(\mu_0 - \mu)^{-1/3}$	(FWHM)	$(\mu_0 - \mu)^{-1/3}$
2	.233	.013	.236	.003	.244
$3\frac{1}{2}$	.421	<.001	.386	.002	.43
$4\frac{1}{2}$	.559	.006	.496	.001	.58
$5\frac{1}{2}$	.700	.004	.591	.005	.73

Table 3.1: Locations of isotherm steps.

$5\frac{1}{2}$, we can estimate that the next steps, $6\frac{1}{2}$ and $7\frac{1}{2}$, would occur at about $(\mu_0 - \mu_{6\frac{1}{2}})^{-1/3} \sim 0.84$ and $(\mu_0 - \mu_{7\frac{1}{2}})^{-1/3} \sim 0.98$ for argon and $(\mu_0 - \mu 6\frac{1}{2})^{-1/3} \sim 0.69$ and $(\mu_0 - \mu_{7\frac{1}{2}})^{-1/3} \sim 0.80$ for krypton. Extrapolating the isotherms, this corresponds to approximately 30 equivalent layers for the $6\frac{1}{2}$ step and more than 100 layers for $7\frac{1}{2}$. Therefore, while it may be possible to find the $6\frac{1}{2}$ step by putting large amounts of gas into the sample cell, it is not likely that it will be possible to form thicker films on grafoam (because the entire cell volume would be filled with condensate).

The data are consistent with the observations made on single-crystal substrates of films of over ten layers in both systems. For an incompletely wetting film, the distance between the layer steps should increase dramatically going to higher coverages, because the bulk vapor pressure (at $(\mu_0 - \mu)^{-1/3} = \infty$) must be reached at a finite film thickness. A completely wetting film, on the other hand, should show evenly spaced steps. The experimental observation is that the separation between steps decreases slightly going from $3\frac{1}{2}$—$4\frac{1}{2}$ to $4\frac{1}{2}$—$5\frac{1}{2}$. The decrease is likely to be due to the error in the pressure measurement.

The peaks labeled $3\frac{1}{2}$, $4\frac{1}{2}$, and $5\frac{1}{2}$ in Figs. 3.3(b) and 3.4(b) are very sharp and probably correspond to first-order phase transitions in agreement with YH's ellipsometry data and our own heat capacity data (Section 3.6). Figure 3.3(b) shows a rounded maximum in the compressibility around the second layer for argon. The layering critical-point temperature is found to be 69.7 ± 0.1K from the heat capacity measurements. The observed maximum in the compressibility

is consistent with passing through the layering critical density at above T_C. There is still a step in the isotherm at this temperature, where the second-layer density changes most rapidly with temperature, but the process is continuous, so the step is not vertical. In the krypton isotherm, the compressibility peak appears to be sharp even though the temperature (102K) is higher than the temperature of the second layer critical point (98.1K), as measured in the heat capacity. There are two possible explanations for this behavior. The exponent δ, governing the shape of the critical isotherm, is 15 in the two-dimensional Ising model, so the isotherms slightly above criticality should be very steep. This fact means that it is very difficult to locate layering critical points using isotherm data, because the compressibility may show very sharp behavior even above the critical point. Another possibility, based on the results of a recent x-ray experiment on krypton, is that a higher order transition exists after the first order layering-transition ends in the second layer. The peak, labeled 2 in Fig. 3.4, is also consistent with this interpretation. This scenario, in which the second layering critical point is actually a multicritical point, is discussed further in chapter 5.

3.1.2 Hysteresis

Clearly there is hysteresis between the upwards and downwards going isotherms in Fig. 3.4. Previous studies have cited hysteresis of this sort as evidence for capillary condensation[66], but it was only recently, in Lysek's methane study, that conclusive proof was given. Lysek made heat capacity scans for systems formed along both the adsorption and desorption branches of the hysteresis loop, mapping out the multilayer phase diagram in N versus T for each type of system. The resulting phase diagrams were shifted in N relative to one another, but could be made to match by subtracting the number difference between the adsorption and desorption branches from the desorption branch phase diagram. This procedure proves that the number difference between the two branches is condensed in some

form other than film, and that the film thickness depends only on the vapor pressure and not on the system history. Indeed, if the the adsorption and desorption branch phase diagrams are plotted in the pressure or μ versus temperature plane, phase boundaries that are due to phase transitions in the film fall directly on top of one another.

The fact that capillary condensation should cause a noticeable amount of hysteresis in an isotherm is far from obvious. However, given the fact that hysteresis occurs, it is possible to make some conclusions about the system being studied. Capillary condensation is a stable form of matter at below the bulk-saturated vapor pressure when a negatively curved interface may be formed between condensate and vapor. The inverse of the radius of curvature of the interface is proportional to the pressure difference across it:

$$\Delta P = -\frac{\sigma}{D}, \tag{3.1}$$

where $D^{-1} = R_1^{-1} + R_2^{-1}$ and R_1, R_2 are the Gaussian radii of curvature of the surface, and σ is the surface tension. For capillary condensation to be stable when the vapor pressure, P_g, is smaller than the saturated vapor pressure, P_0, its chemical potential, μ_c, must be equal to the chemical potential of the vapor, μ. The chemical potential of the vapor may be found by using the differential relation $d\mu = v_g dP$ at constant temperature, and integrating from the chemical potential at saturation, μ_0^g:

$$\begin{aligned} \mu = &\quad \mu_0^g + \textstyle\int_{p_0}^{p_g} v_g dP \\ = &\quad \mu_0^g + \textstyle\int_{p_0}^{p_g} k_B T \frac{dP}{P} \qquad \text{(ideal gas law)} \\ = &\quad \mu_0^g + k_B T \log\left(\frac{P_g}{P_0}\right). \end{aligned} \tag{3.2}$$

In the capillary condensate:

$$\begin{aligned} \mu_c = &\quad \mu_0^g + \textstyle\int_{p_0}^{p_g} v_s dP \\ = &\quad \mu_0^g - v_s \frac{\sigma}{D}. \end{aligned} \tag{3.3}$$

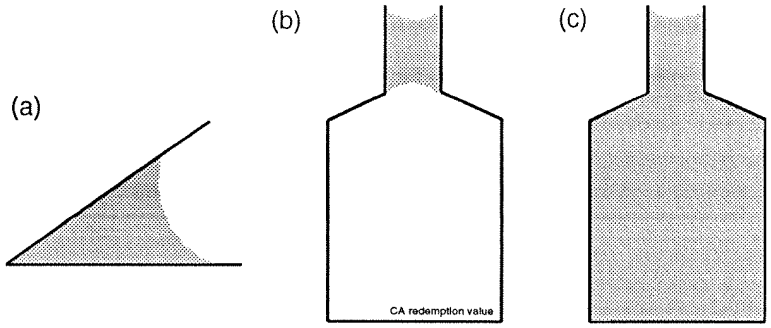

Figure 3.5: Examples of "capillaries" in a porous substrate: (a) perfect wedges should show no hysteretic behavior. (b) bottle-shaped capillaries on the adsorption branch. (c) bottle-shaped capillaries on the desorption branch.

Equating Eqns. 3.2 and 3.3,

$$P_g = P_0 \exp\left(\frac{-v_s\sigma}{k_B T D}\right). \tag{3.4}$$

D, of course, may never be smaller than the radius of a particular pore, so we expect matter to condense in smaller pores at lower pressures than in larger pores. It is not likely that perfectly uniform pores exist in grafoam. Instead, the capillaries are probably mostly wedges where graphite platelettes meet at a small angle. In the case of a wedge, shown in Fig. 3.5(a), the radius of curvature of the condensate-vapor interface is related to the amount of condensed matter. The angle at which the interface meets substrate is determined by the various surface tensions. In the case of wetting, the condensate-vapor interface must meet the substrate at zero contact angle. The amount condensed in a wedge is then determined by the radius of curvature, which is determined by the pressure, so no hysteretic behavior is expected.

To account for the hysteresis, we must also consider "bottle"-shaped pores as in Figs. 3.5(b) and (c). Such pores may be expected to occur in the densely packed array of graphite platelettes making up the grafoam. Starting from a bare substrate and low pressures, condensate may condense in the narrow "neck" of the bottle (Fig. 3.5)(b). As the pressure is increased, the radius of curvature grows

larger, and the bottle becomes completely filled. Then, as the pressure is reduced, the condensate remains stable until low pressures are reached, corresponding to R of the neck. Thus, the hysteretic behavior observed in the system suggests the presence of voids or "bottles" in the substrate.

Capillary condensation poses a problem for multilayer studies using high surface area substrates such as graphite, because the exact number in the film cannot be known for thicker films. The number in the capillary condensate may be minimized by attempting to keep the system on the adsorption branch of the hysteresis loop. That is, the film should always be formed by increasing, never decreasing, the coverage. However, during an experiment, such as a heat capacity run, the temperature of the cell is increased, resulting in molecules leaving the film and entering the vapor, so it is rarely possible in practice to keep the system strictly on the adsorption branch. Further, we found that for methane, argon, and krypton, capillary condensation is nucleated on the adsorption branch at around three and a half layers, and the amount condensed in capillaries increases rapidly with coverage. The problem may be partially surmounted by plotting multilayer phase diagrams in the μ versus T plane. N versus T phase diagrams may still be drawn if care has been taken to keep the system on the adsorption branch, but the utility of these phase diagrams is severely limited at higher coverages.

3.2 First-Layer Melting in Argon

The triple-point temperature of the first layer of argon on graphite was found to be 47.2K on the basis of the observation of small, sharp, coverage-independent peaks in a heat capacity study[67]. There is still some controversy over whether these peaks were correctly identified as melting. The small peak was followed by a much broader peak, tentatively identified as a transition from a substrate-induced, hexatic phase to a uniform fluid phase. The small, sharp peak was

labeled as "weakly first order", so the melting process was not believed to occur by the KTHNY mechanism. Other studies[68, 27] have concluded that the melting transition in monolayer argon is probably continuous. It is clear that the triple-point phenomena in monolayer argon occurs well below the minimum temperature attainable with our experiment. However, when the monolayer completes, the first-layer melting transition is pushed to much higher temperatures, so we are able to study melting in the "extended monolayer" regime.

Figure 3.6 shows peaks that are due to first layer melting for coverages of 1.00 to 1.88 nominal layers. None of the monolayer studies mentioned have examined first layer melting at these coverages. The tall, sharp peaks are clear evidence that the first-layer melting transition is first order at these coverages. The peak in the lowest coverage scan (1.2 layers) has some width, which may be due to crossing a liquid-solid coexistence region. As the phase boundary bends upward in the N–T plane, the peaks begin to resemble delta functions, indicating a very narrow coexistence region.

One possible reason for the apparent transition from continuous to first-order melting was suggested by Chan[27]. The continuous melting behavior in the monolayer may be due to the strong orientational effect of the substrate. The lattice constant of monolayer argon is about $4.0\mathring{A}$[24], only slightly less than the commensurate value of $4.26\mathring{A}$. It is expected that the substrate will tend to encourage the sixfold orientational symmetry of the hexatic phase in an overlayer that is close to the registered density[1]. As the monolayer is compressed by an overlaying film, the orientational effect is expected to decrease, possibly resulting in a change in the melting behavior.

We cannot confirm such a picture from our data because of an additional complication. Approximately six degrees before the first-layer melting peak, a small, sharp peak is observed. This peak resembles peaks in the methane/graphite sys-

[1]It seems to us that the lattice mismatch is rather large for this argument to be applicable.

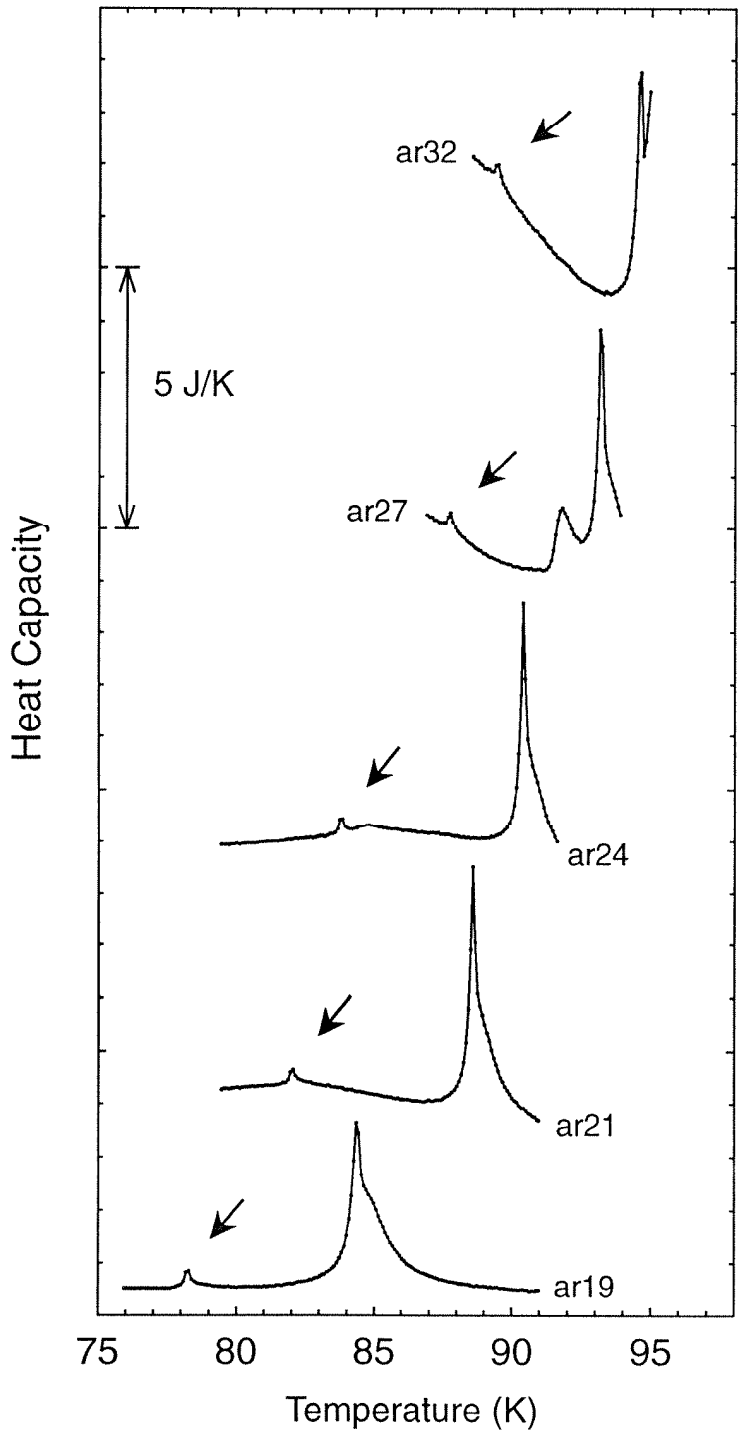

Figure 3.6: First layer melting peaks in argon on graphite. Heat capacities are uncorrected for desorption. Coverages, at the peak are 219.5, 250.8, 287.0, 348.4, and 414.6. The small peaks (arrows) are a possible CI transition.

tem that were identified as CI transitions[45, 51] by comparison with the results of x-ray experiments. Because CI transitions are common in the extended monolayer regime, and because the small peaks observed in argon/graphite are very similar to those in methane/graphite, we may identify the small peaks as being due to a CI transition between HD incommensurate and registered phases. A transition from HD to LD phases is not allowed because there would be no change in symmetry. The mechanism responsible for this transition may be simply the temperature-driven expansion of the first layer. If this interpretation of the small peak is correct, then the first layer melts from a registered phase (the same as methane at high coverages). In a registered phase, the substrate should induce a very strong orientational order, so the argument given in the previous paragraph should not apply. There is as yet no scattering evidence of a registered phase in the argon/graphite system. Understanding how this phase transition joins onto the monolayer phase diagram would be the key to unravelling the mystery of melting in the first layer of argon.

An additional peak is shown in Fig. 3.6 in scan ar27, between the CI and melting peaks, and in scan ar32, at about 95K. These peaks are not due to a phase transition in the film, because they actually cross the first-layer melting curve. Similar peaks were found in the methane study where they were found to be due to desorption in the film.[46]

3.3 Second-Layer Phase Diagrams

In both argon and krypton the second layer forms on top of a high-density, solid first layer. Because the substrate potential is still very strong around the height of the second layer, it is expected that the second layer may show two-dimensional behavior similar to the first layer. One difference between layers one and two is that the corrugation potential seen by the second layer is more likely to be close

to the second layer's natural lattice constant. The second layer should not form a high-density, incommensurate phase with respect to the first layer, because such a phase would be unstable to molecules leaving the second layer and entering the first layer. The neutron diffraction study by Gay *et al.*[33] found a more or less uniform (though temperature and coverage dependent) lattice spacing throughout the solid argon film, so it is likely that the second layer is commensurate with the first layer at most temperatures and coverages. Thermodynamic evidence will be presented in this section, suggesting the existence of a CI transition between a mutually commensurate bilayer and an incommensurate bilayer, where the second layer has a lower density than the first layer.

Figures 3.7 and 3.8 show the low-temperature region of several heat capacity scans around the formation of the second layer in argon and krypton respectively. The krypton scans are corrected for desorption, while the argon scans are not. At these coverages, there is no sign of a peak near T_t, so there is very little capillary condensation in the system.

Scans ar71, ar21, and ar22 show two separate features. First, a steplike feature in the heat capacity occurs at low temperature. The step occurs at the same temperature and chemical potential to within the experimental accuracy (0.1K), for each of these three scans. The same behavior is seen in scans kr46, kr06, and kr07, in Fig. 3.8, except that instead of a step, a well-defined peak is seen, again at the same temperature and chemical potential. This point, at $T_{t,2}^{ar} = 66.0$K for argon and $T_{t,2}^{kr} = 94.2$K for krypton, must be the intersection of two lines of phase transitions. One of these is the second layering transition, which is first-order. The intersection of first-order transitions is referred to as a triple point. The termination of a second-order line on a first-order transition is referred to as a critical endpoint. It is not clear which term applies to this situation, as we cannot determine with confidence the order of the other line of phase transitions. For the rest of this paper, we will refer to the features at $T_{t,2}^{ar}$ and $T_{t,2}^{kr}$ as second-

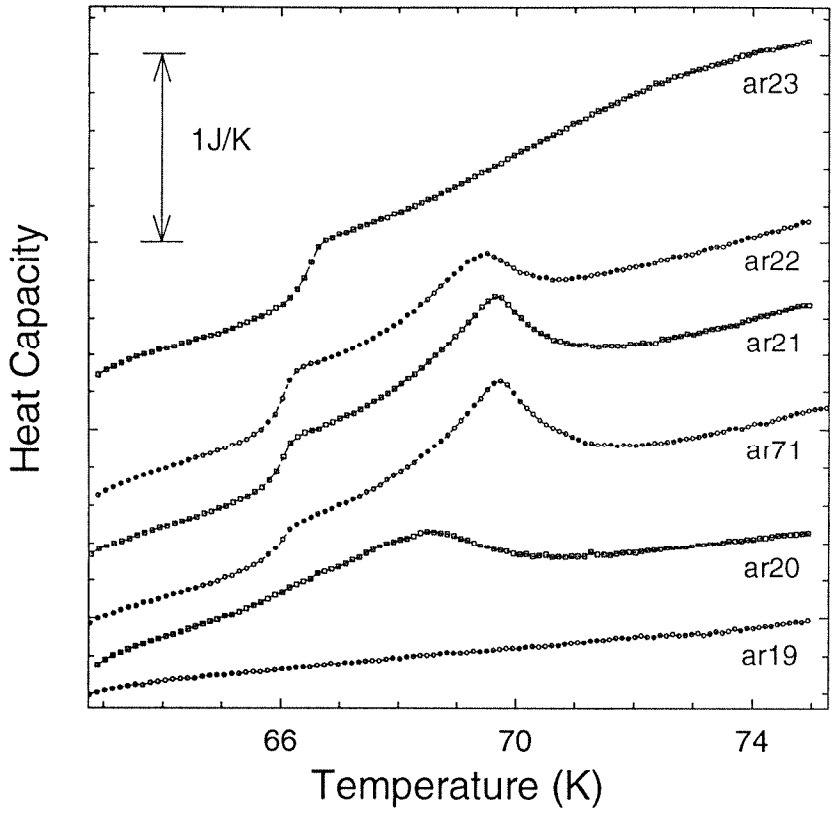

Figure 3.7: Second layer triple point peaks in argon. Heat capacities are uncorrected for desorption. Coverages are 264, 301, 359, 385, 400, and 440 stpccs.

layer triple points, because triple points are more common in nature, and it is really only a matter of terminology. The physical interpretation of these points are points in (μ, T) at which three different phases, in this case solid, liquid, and gas phases, may coexist. The layering transition corresponds to both the solid-gas and liquid-gas transitions. The solid-liquid (melting) transition is responsible for the step features in Fig. 3.7 and the low-temperature peaks in Fig. 3.8. In argon, the height of the step feature increases, going from ar71 to ar22, because the density of the second layer is increasing. Similarly, in krypton, the size of the peak increases from kr46 to kr07. The steplike features found in the argon scans

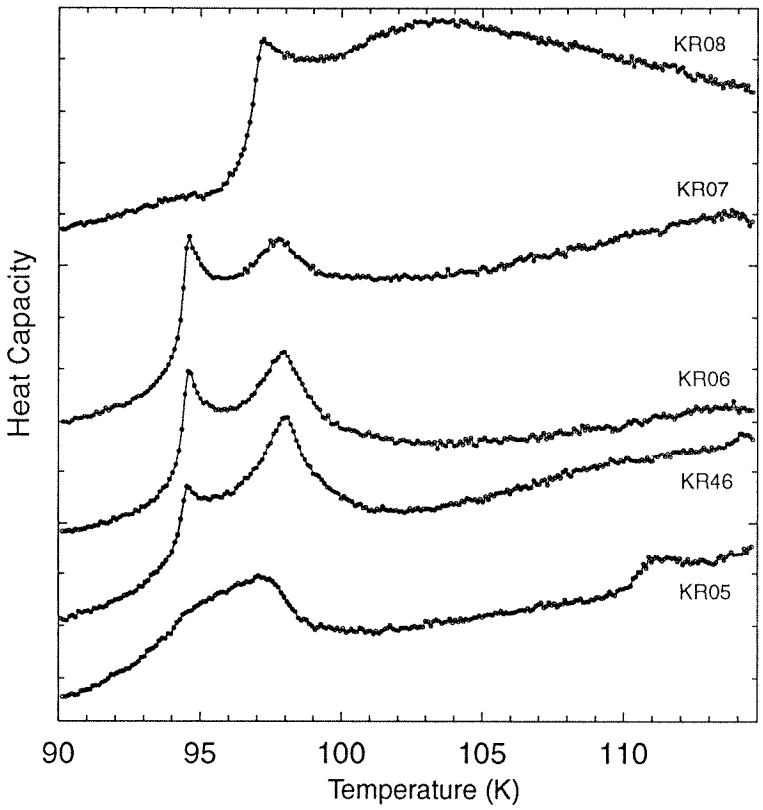

Figure 3.8: Second layer triple point peaks in krypton. Heat capacities are corrected for desorption. Coverages are 270, 305, 310, 348, and 390 stpccs.

may seem to suggest that melting at the second-layer triple point is continuous. However, considering the confusion in the literature as to whether the small, sharp peaks in monolayer argon represent a first order, a "weakly first order," or a continuous phase transition, it would be imprudent to form any such conclusion about second-layer melting on the basis of our data. It is also possible that a very small but sharp peak may be missed in a scanning measurement, although peaks are reported in this study with a full width at half max of $\sim 0.2K$.

The second feature seen in scans ar71, ar21, ar22, kr46, kr06, and kr07 is a cusplike anomaly at slightly above $T_{l,2}$. This feature is due to crossing the boundary between liquid-gas coexistence and uniform fluid. A feature in the heat capacity as this boundary is crossed has been shown to occur in other systems[50,

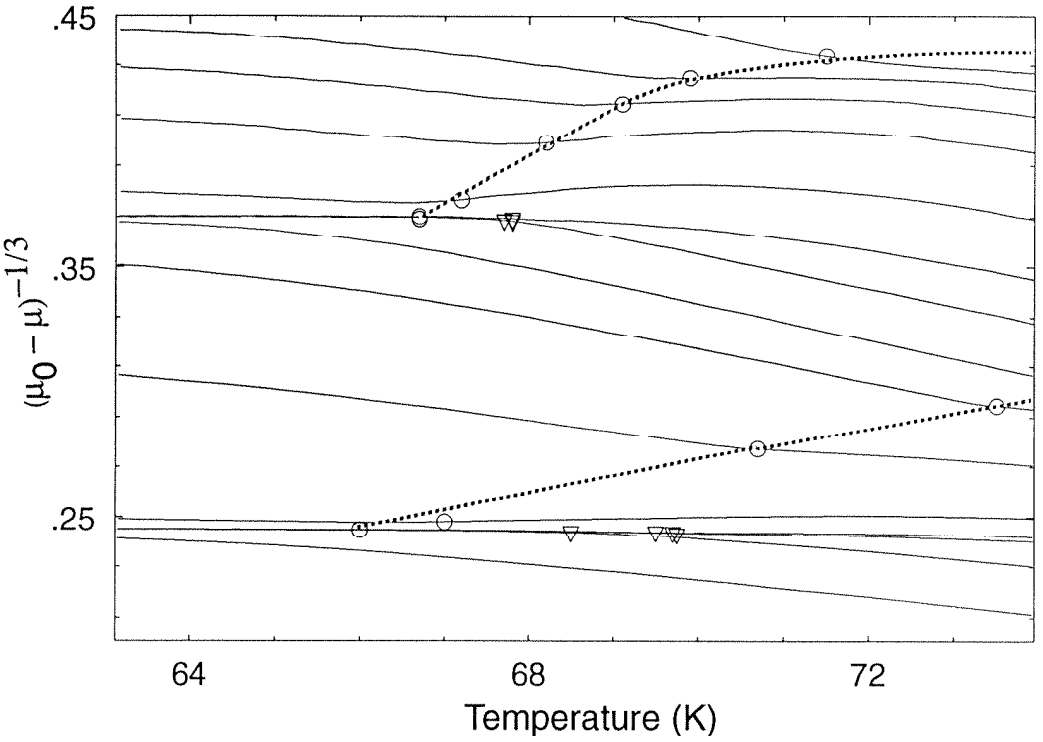

Figure 3.9: μ trajectories for scans around the second and third layering transitions in Ar. Places where trajectories collapse indicate layering-transitions. Dotted lines indicate melting transitions.

51, 52]. The heat capacity in the coexistence region may be expressed as:

$$C = \begin{cases} xC_{liquid} + (1-x)C_{gas} + \frac{dx}{dT}NL & ,T < T_0(x) \\ C_{fluid} & ,T > T_0(x) \end{cases} , \tag{3.5}$$

where x is the fractional density of the 2D liquid phase, N is the total number, L is the latent heat per molecule of transition between the two phases, and $T_0(x)$ is the boundary of the coexistence region. A discontinuity in the heat capacity may be expected as the coexistence boundary is crossed, because the latent heat term jumps abruptly to zero. In practice, this term is very small, so only a discontinuity in the slope of the heat capacity is expected. A second contribution to the heat capacity, in addition to that described by Eqn. 3.5, is expected if the experimental path passes close to the two-dimensional critical point. Around the critical point one expects a maximum in the heat capacity because of critical-point fluctuations.

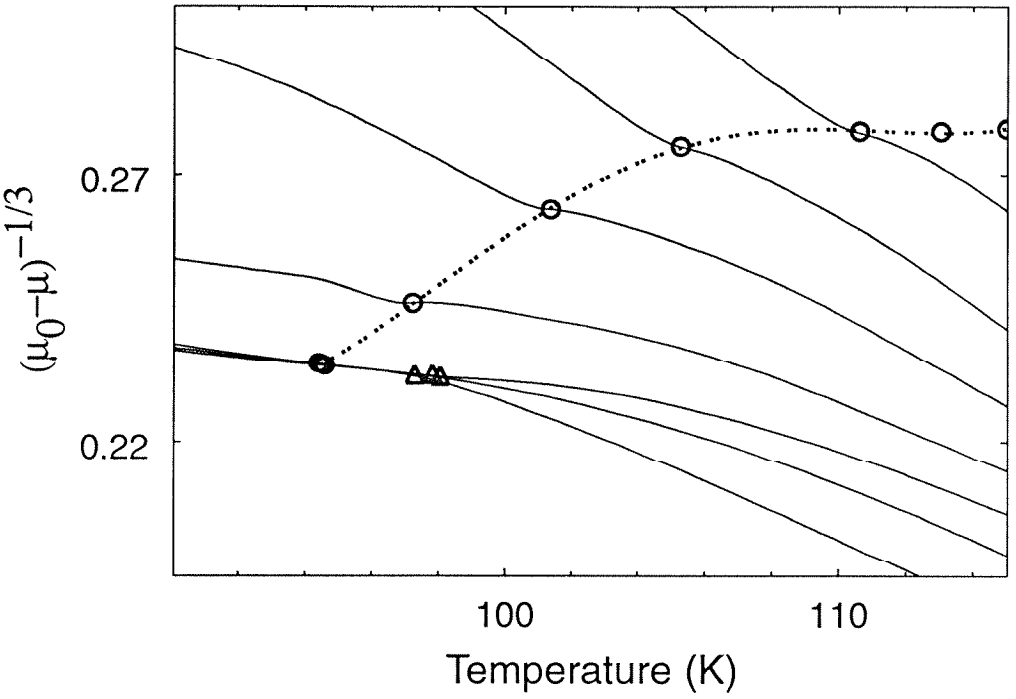

Figure 3.10: μ trajectories around the second layering-transition in krypton.

This maximum does not necessarily occur exactly as the experimental path crosses the phase boundary. At the critical point itself, a divergence should occur in the heat capacity, but the probability of a scan's passing exactly through the critical point is small, and the divergence should be rounded out because of substrate inhomogeneity and finite size effects. The measured heat capacities may be due to a combination of the two effects described. A best estimate for the temperature of the critical point is made by determining the location of the highest temperature cusp. For argon, the second layering, critical-point temperature, $T_{c,2}^{ar}$, is 69.7 ± 0.1K, and for krypton, $T_{c,2}^{kr}$ is $98.0 \pm 0.1K$. Because the coexistence region is very blunt ended, the error in T_C is taken to be the temperature resolution of the heat capacity data.

The interpretation of the second peaks is strengthened by the scans ar21, ar22 and kr07, which show the cusp at a lower temperature than in the scan

at the next lowest coverage. This behavior is consistent with monolayer studies and with the bilayer CO study and ethane multilayer study of Chan *et al.* that found rounded phase boundaries. These phase boundaries were interpreted as the boundaries of coexistence regions because the peaks occurred close to the critical-point temperatures found in isotherm measurements.

The case for cusped anomalies occurring in the heat capacity at the coexistence boundary is further strengthened by the simultaneous pressure measurements taken in this study. Figures 3.9 and 3.10 show the experimental trajectories plotted in $(\mu_0 - \mu)^{-1/3}$ versus T for around the second and third layer in argon and the second layer in krypton. Curves at different coverages that collapse in chemical potential indicate scans passing through coexistence regions and correspond to vertical steps in isotherms. We can easily locate the layering-transitions from these sorts of data. The locations of the cusp features are plotted as inverted triangles in the figures. It is observed that the cusp features occur exactly where the scans depart from the layering coexistence regions. In the highest coverage scans in Figs. 3.7 and 3.8, melting occurs at above the second-layer, triple-point temperature. The corresponding μ trajectories for these scans do not follow the layering transition.

3.4 Second-Layer Melting above the Triple Point

Figures 3.11 and 3.12 show representative heat capacity scans detailing the extension of the second-layer melting lines to high coverages. In Fig. 3.11, the high temperature peaks are the first-layer melting peaks shown in Fig. 3.6. The small peaks preceding first-layer melting by about six degrees are due to the CI transition in the first layer. The bottom left of Figs. 3.11 and 3.12 show the same scans as Figs. 3.7 and 3.8. The second-layer melting transition is the broad, mesalike feature in the center of the figures. The peaks increase in temperature with increasing

coverage to well beyond the bulk-triple-point temperatures (83.78 and 115.95K). In the argon data, the heat capacities for scans ar23, ar24, ar15, ar25, and ar26 show the same sort of step as was seen at the triple point. For higher-coverage scans, a peak begins to develop. In krypton, there is a peak for second-layer melting at all coverages. The broad plateau in the heat capacity following the melting transition is puzzling. For a system passing through a first-order transition at constant volume or area, a mesa in the heat capacity is expected, and the μ trajectory should follow along the melting line for a short distance. The heat capacity features observed are suggestive of this sort of interpretation, but the μ data are not found to follow the melting line. The initial peaks (and steps) may still represent first order phase transitions, or it is possible for melting to be second order. The plateaus, however, do not signify broad solid-liquid coexistence regions. One possible explanation for the plateau may be that the heat capacity of the liquid phase is higher than the solid, resulting in the step, and the falloff at higher temperatures may occur as the second layer depopulates because of desorption of the film.

For all but the first couple of scans above the 2D triple-point pressure in Figs. 3.11 and 3.12, a small peak is observed to precede the second-layer melting transition. Figures 3.13 and 3.14 show blowups of the risers to the second layer melting peaks for selected scans. The small peak is interpreted as a CI transition at which the second layer become expanded with respect to the first layer. There are two arguments for this identification. First, the size and shape of the peak are consistent with the CI-transition peaks in monolayer methane where scattering experiments have identified CI transitions. The second argument is reasoning by elimination. Given that the interpretation of the melting peak is correct, the small peak must represent a solid-solid phase transition. Because argon is a noble gas and "can't do anything a billiard ball can't do"[69], the only reasonable possibility for a solid-solid transition is a registry transition. As we have argued,

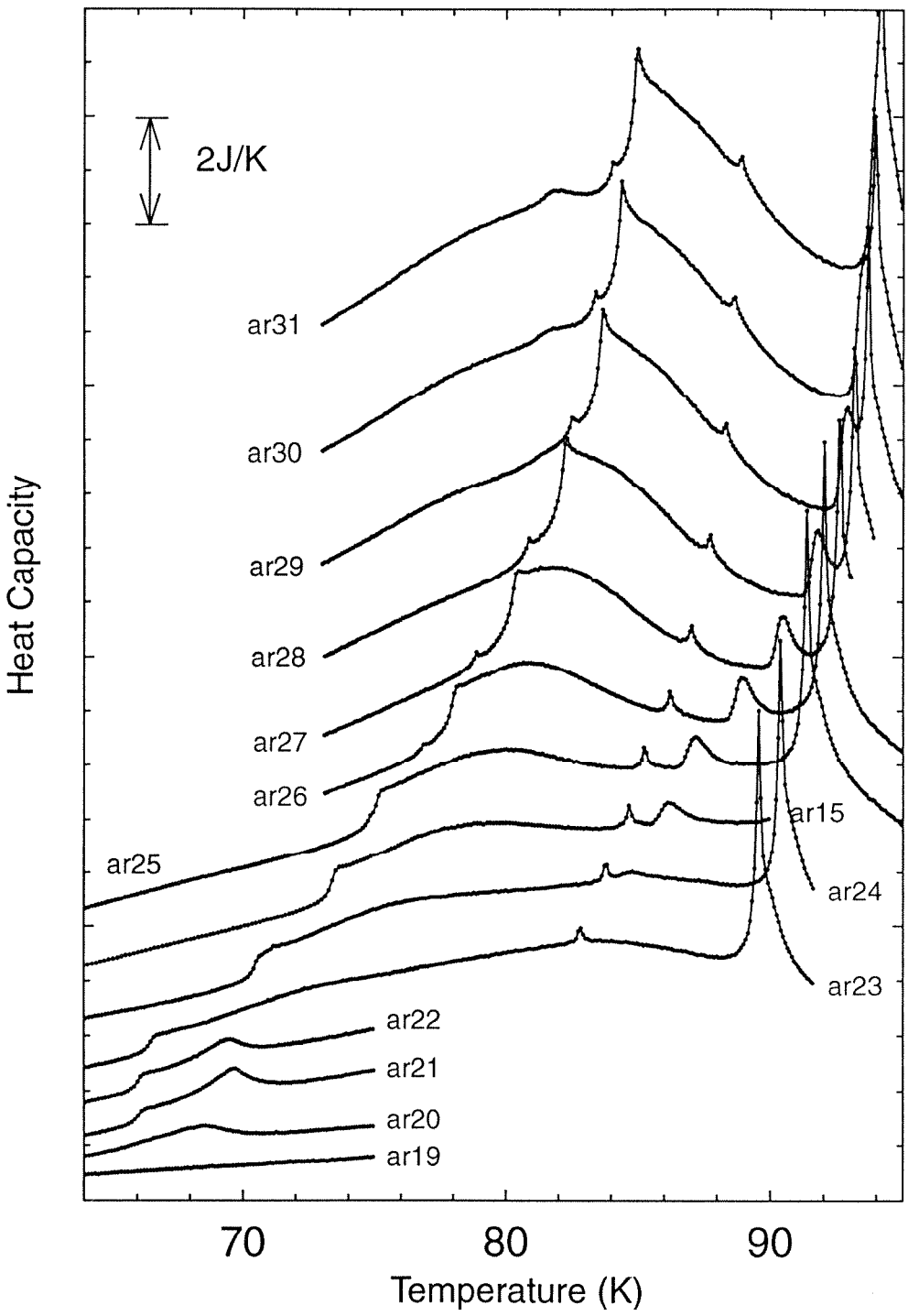

Figure 3.11: Second-layer melting above the triple point in argon. Heat capacities are uncorrected for desorption. Coverages are 1.34, 1.60, 1.72, 1.79, 1.96, 2.14, 2.26, 2.34, 2.42, 2.50, 2.57, 2.64, 2.70, and 2.74 equivalent layers at the second-layer melting peak.

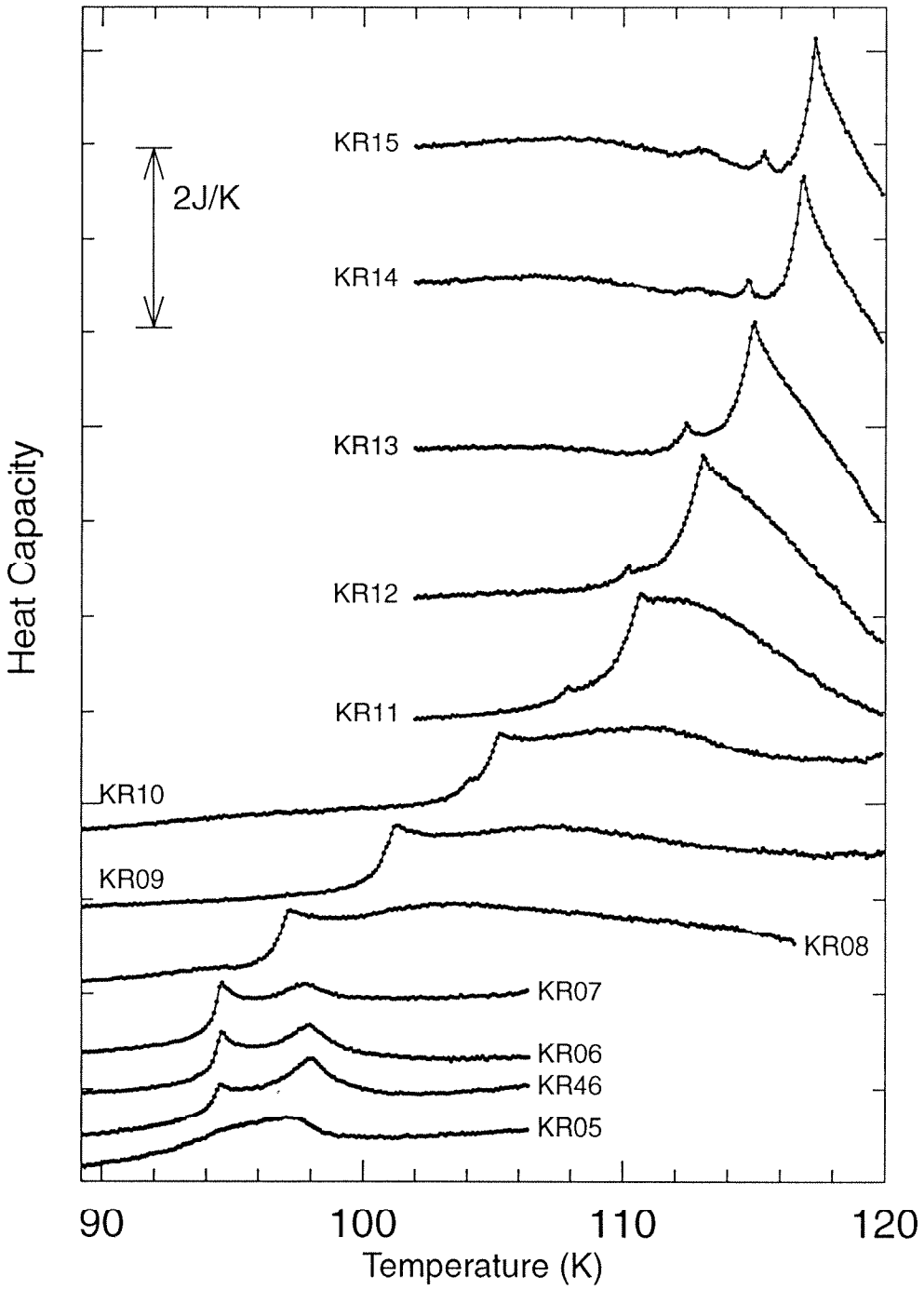

Figure 3.12: Second-layer melting above the triple point in krypton. Heat capacities are corrected for desorption. Coverages at the peak are 1.04, 1.17, 1.19, 1.34, 1.49, 1.62, 1.71, 1.77, 1.80, 1.82, 1.87, and 2.00 stpccs.

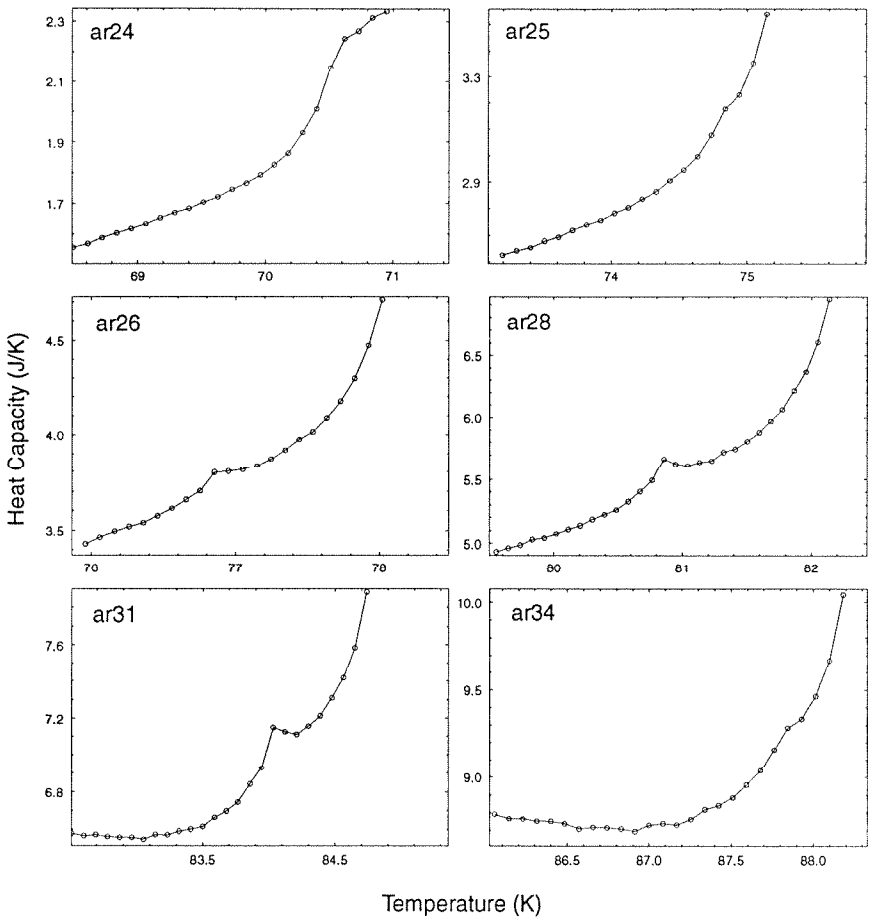

Figure 3.13: Rising edges of second-layer melting peaks in argon. Heat capacities are uncorrected for desorption. The small peaks observed in some scans may be a CI transition between the first and second layers.

a high-density incommensurate phase in the second layer is highly unlikely, so the only possibility left is a transition from a registered to a low-density phase.

Figure 3.15 shows some possible phase diagrams for the second layer of argon and krypton. In 3.15(a) and 3.15(b), the second-layer solid forms as an incommensurate phase and locks into registry only after the layer is complete. This behavior may be observed, for example, if the monolayer is highly compressed by the substrate potential. The second layer would not see as strong a potential as the first layer and may form an incommensurate phase until the pressure exerted

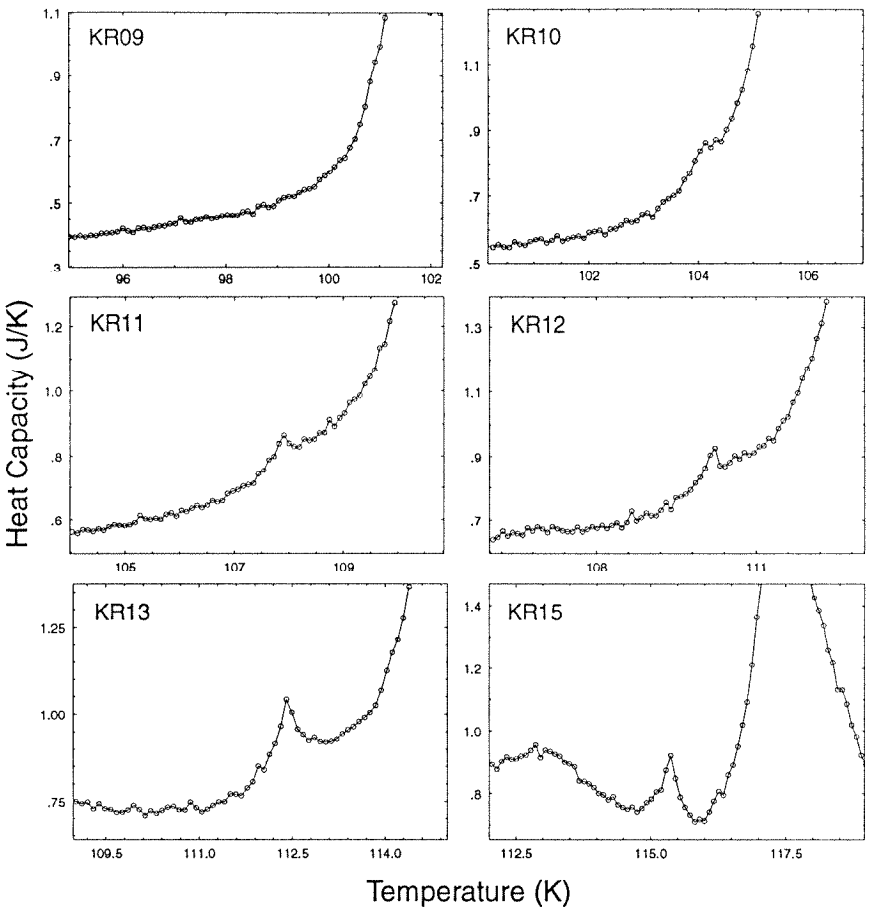

Figure 3.14: Rising edges of second-layer melting peaks in krypton. Heat capacities are corrected for desorption. The small peaks observed in some scans may be a CI transition between the first and second layers.

by the formation of higher layers becomes strong enough to lock it into registry. The argon and krypton data seem to suggest possibilities (c) and (d), respectively. Scan ar25 in argon and kr10 in krypton seem to show the CI transition peak emerging from the second-layer melting peak. At much higher coverages, the small peak seems to rejoin the melting peak in argon (see ar34) but not in krypton. In these cases, (c) and (d), the second layer forms as a registered phase, and the I phase occurs only as a sort of "premelting" transition at some coverages.

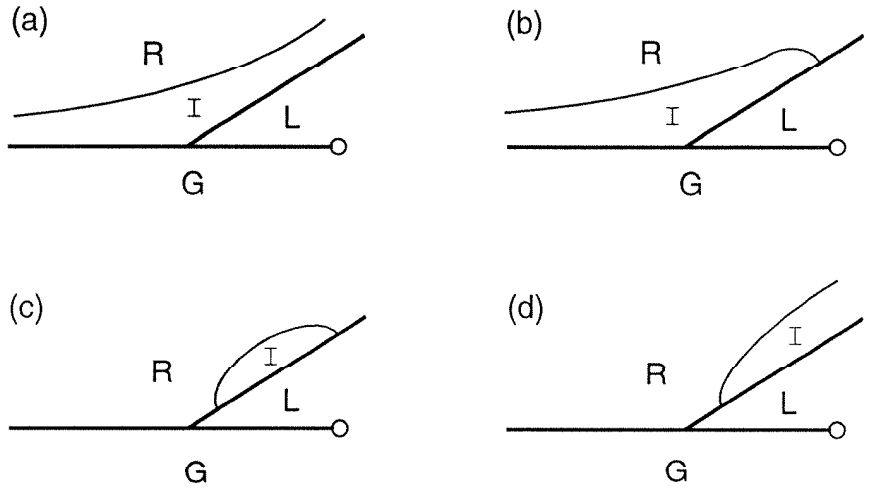

Figure 3.15: Possible phase diagrams for second-layer argon and krypton, including the proposed CI transition. "I" denotes incommensurate or LD phase. "R" is registered; "L" is liquid; and "G" is gas.

3.5 Third-Layer Phase Diagram

Figure 3.16 shows heat capacity scans for coverages around the completion of the third layer in argon. These data are very similar to the second-layer data in both argon and krypton. Scans passing along the third layering-transition, ar26, ar72, ar27, and ar73 (see Fig. 3.9) show two features, a sharp step that is due to triple-point melting at $T_{t,3}^{ar} = 66.7 \pm 0.1K$ and a cusp that is due to crossing the third-layer coexistence boundary. The critical temperature is estimated to be $T_{c,3}^{ar} = 67.8 \pm 0.1K$, so the liquid gas coexistence region is very narrow, about 0.8K. The relation $T_{t,2}^{ar} < T_{t,3}^{ar} < T_{c,3}^{ar} < T_{c,2}^{ar}$ suggests that phenomena in the higher layers may be qualitatively different.

The third-layer melting transition, above the triple-point pressure, is shown in Fig. 3.17. Above the maximum coverage of the third-layer liquid-gas coexistence, the melting transition becomes mesalike as in the second layer (Fig. 3.17(a), scans ar52 and ar28), suggesting that melting may be first order. Several differences are apparent in the third layer. First, the mesalike features are much narrower than

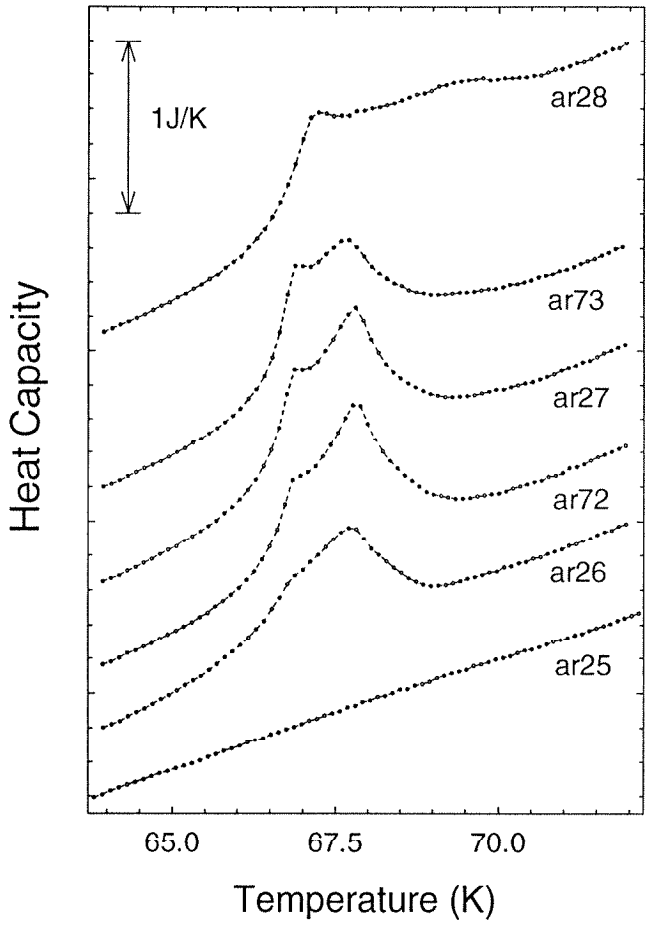

Figure 3.16: Heat capacity scans around the third-layer triple point in argon. Heat capacities are not corrected. Coverages are 2.60, 2.85, 3.00, 3.10, 3.16, 3.35 equivalent layers.

those that are due to second-layer melting, and they increase in temperature much less rapidly with coverage. Second, the mesas decrease in size with increasing coverage and change their shape entirely at a coverage of about 3.90 total layers adsorbed (Fig. 3.17(b)). At this coverage, a more complicated phenomenon presumably occurs as the melting transition joins the reentrant layering-transition, and we can no longer be sure of the order of melting. The heat capacity signatures of the reentrant layering-transitions are discussed in more detail in the next section. This behavior is consistent with Youn and Hess'[58] observation of first

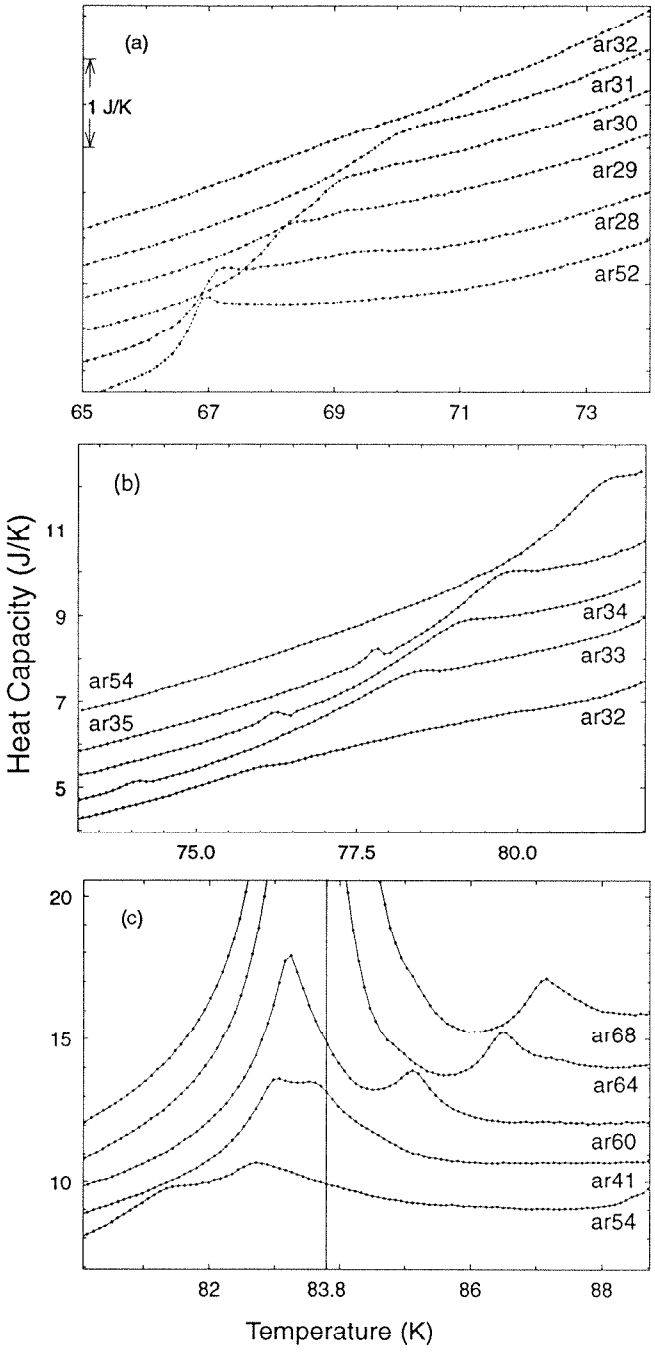

Figure 3.17: Third-layer melting in argon above the triple point. Coverages are (a) 3.15, 3.28, 3.50, 3.63, 3.75, 3.95; (b) 3.95, 4.18, 4.20, 4.23, and 4.32; (c) 4.32, 4.61, 5.26, 6.63, and 10.67 equivalent layers. The peaks describe a range of behavior as the coverage is increased.

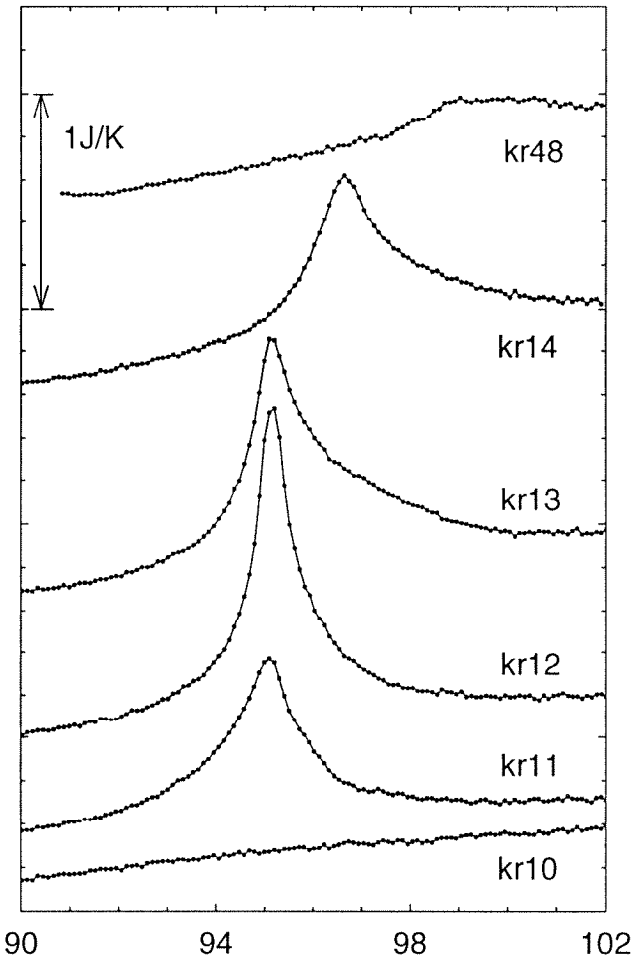

Figure 3.18: Heat capacity scans, corrected for desorption, around the formation of the third layer in krypton. Coverages are 504.92, 574.02, 613.20, 651.64, 700.26, and 781.47 stpccs.

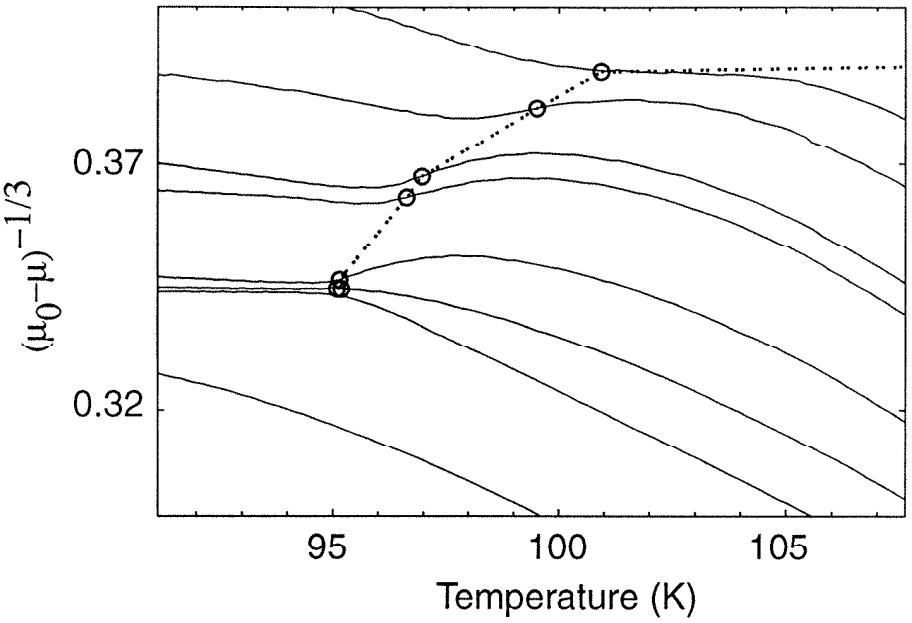

Figure 3.19: μ trajectories around the end of the third layering-transition in krypton. The dotted line is interpreted as the disordering of the third layer.

order reentrant layering-transitions for coverages above three layers. These are layering-transitions (see section 1.6) that seem to reappear at temperatures above that of the layer critical point.

Third-layer melting is observed above T_t (Fig. 3.17(c)), where it appears as a small, rounded peak in contrast with the high-coverage second-layer melting peak. The peaks around 83K in this figure are bulk melting. The coverages indicated for the high coverage scans in Fig. 3.17 are to be regarded as the total amount adsorbed in the system, including capillary condensation. The heat capacity peak near T_t in each of the curves of Fig. 3.17(c) shows that a considerable amount of capillary condensation is beginning to occur. As the third-layer melting transition crosses T_t, the chemical potential difference, $\mu - \mu_0$, is less than that of the fourth layering-transition, so the film thickness is still less than four layers at this point.

Figure 3.18 shows heat capacity features around the formation and completion of the third layer in krypton. The striking difference between these peaks and

those for the second layer of krypton and the second and third layers of argon is that scans that pass along the layering-transition (kr11, kr12, and kr13) have only one peak. The peaks for kr11, kr12 and kr13 occur at the same temperature and chemical potential to within the experimental accuracy, but this point cannot be a triple point, since it is not followed by a coexistence region at higher temperature. These peaks join onto a line of peaks (kr14 and kr48, Fig. 3.18) extending to higher temperatures and coverages. Figure 3.19 shows the μ trajectories for these scans. The three peaks from scans kr10, kr11, and kr12 occur at the endpoint of the third layering-transition, which is also the origin of the line of phase transitions shown with a dotted line in Fig. 3.19. We will label this point $T_{t,3}^{kr}$. The dotted line may be identified with melting in analogy with the second layer. Because there is no triple point in the third layer, there can be no separate liquid and gas phases. Instead, only solid and fluid phases exist. The phase diagram depends on the order of the melting transition above $T_{t,3}^{kr}$. The two possibilities are shown in Fig. 3.20. In case (a), the melting transition is first order, as suggested by the μ trajectories in Fig. 3.19. This case resembles the incipient triple-point behavior found in monolayer N_2[29]. The peaks at $T_{t,3}^{kr}$, in this case, would occur along the vertical portion of the phase boundary. In case (b), the melting transition is second order, and $T_{t,3}^{kr}$ represents a tricritical point at which the solid-fluid transition changes from first order to second order.

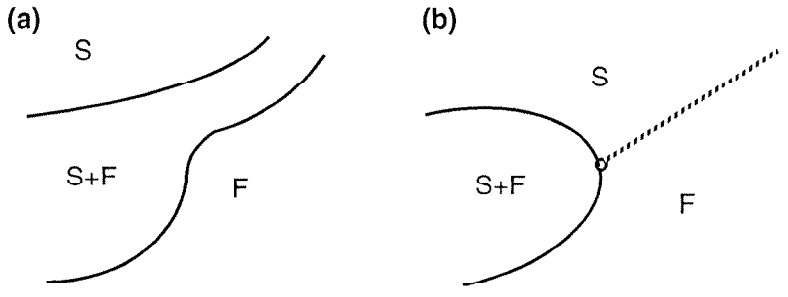

Figure 3.20: Possibilities for the third layer phase diagram in Kr: (a) the melting transition is first order; (b) melting is continuous.

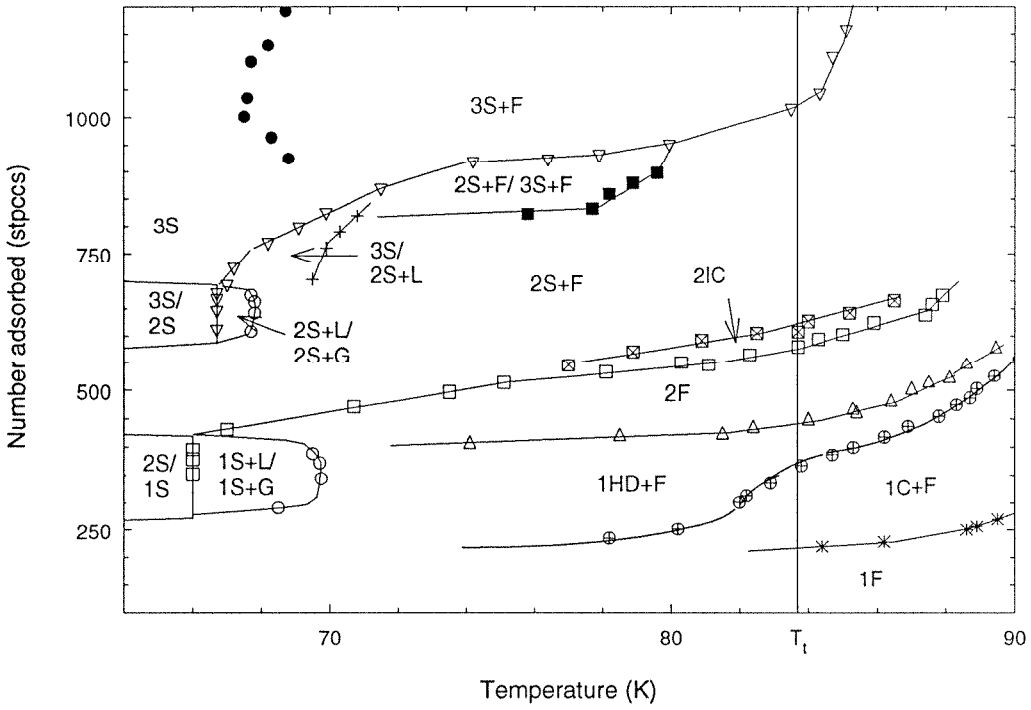

Figure 3.21: Phase diagram for the first three layers of argon/graphite in number adsorbed versus temperature.

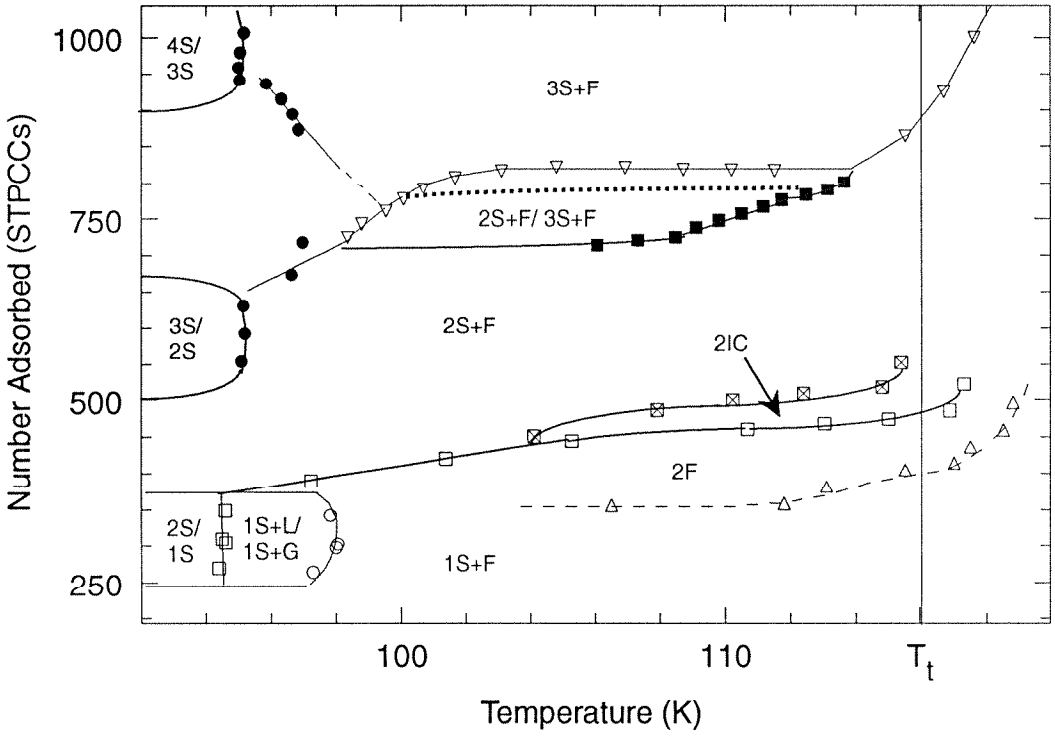

Figure 3.22: Phase diagram for the first three layers of krypton/graphite in number adsorbed versus temperature.

Figures 3.21 and 3.22 show the phase diagrams for the first three layers of argon and krypton plotted in the N versus T plane. N is the total number adsorbed including film and capillary condensation. Most of the phase diagrams are relatively undistorted, indicating that capillary condensation is not very important in the first three layers. Points show the locations of the various heat capacity features, and lines correspond to phase boundaries drawn, based on the heat capacity data. The dashed phase boundary is speculative. The meanings of the various symbols are as follows: open squares are second-layer melting, open circles are second and third-layer liquid/gas coexistence, upright triangles are the approximate ends of the mesas initiated by second-layer melting, crossed circles ($\oplus$) are the first-layer CI transitions, $*$s are first-layer melting, crossed squares are the second-layer CI transitions, inverted triangles ($\bigtriangledown$) are third-layer melting, +s are the end of the third-layer melting mesas, filled squares are the peaks found upon leaving the reentrant layering-transitions, filled circles are phase transitions in higher layers. NS means N solid layers. G means an uppermost layer of 2D gas. F is 2D fluid. 2I is the incommensurate, bilayer phase. In the argon phase diagram, the two monolayer solid phases are HD, high-density incommensurate, and C, $\sqrt{3} \times \sqrt{3}$ registered phases. 2F is the speculative bilayer fluid phase that will be discussed in Chapter 5.

3.6 Higher Layers

In Fig. 3.17, third-layer melting in argon was observed as mesalike peaks, but at a coverage of about 3.9 equivalent layers, two separate peaks were visible and the mesas had disappeared. In the region between the two peaks, the μ trajectories indicate that the scans pass through a coexistence region. Heat capacity scans between layers three and four in argon are shown in Fig. 3.23, and the positions of the peaks are plotted above in the μ versus T plane. Triangles correspond

to the third-layer melting peaks and also to the small peaks (shown with arrows in the bottom part of the figure). Filled squares correspond to the broad peaks at high temperature that occur as the μ trajectories leave coexistence. Filled circles correspond to the peaks moving backward in temperature with increasing coverage that join onto the endpoint of the fourth layering-transition (sharp peak, upper left of the figure). The coexistence region, shown with a double line in Fig. 3.23, is identified as the reentrant layering transition found in Youn and Hess' ellipsometry study[58, 38]. The chemical potential difference along the layering-transition is nearly constant and is equal to $\delta\mu$ of the step labeled $3\frac{1}{2}$ in Fig. 3.3. From the argon data, it is not clear whether or not the small peak in the heat capacity occurs exactly where the scan joins the reentrant layering transition. In the krypton data, described below, it is found that the small peaks occur at slightly smaller $\delta\mu$. For scans above about 4.8 equivalent layers (Fig. 3.17(c)), heat capacity scans again show only one peak for third-layer melting, which increases in temperature to above the bulk triple point. The fourth layering transition, shown at $(\mu_0 - \mu)^{-1/3} \sim .5$ in the figure, was located using the μ data. Our best estimate of the start of the reentrant layering-transition, which we will label $T^{ar}_{t,3\frac{1}{2}}$ is $70. \pm 0.5$K. We estimate the end of this layering-transition, which we label $T^{ar}_{c,3\frac{1}{2}}$, to be 79.8 ± 0.5K.

Heat capacity scans between coverages of four and five layers are shown in Fig. 3.24. These features are much smaller than those shown in Fig. 3.24, and there is no longer a separate feature near the point where a scan joins the coexistence region. In this case, the reentrant layering-transition was drawn in by joining the high-temperature peaks (filled squares) with the cusp in the low-temperature peaks (filled circles). The chemical potential difference is the same as that for the step labeled $4\frac{1}{2}$ in Fig. 3.3 and Table 3.1.1. We find $T^{ar}_{t,4\frac{1}{2}} = 70.5 \pm 0.5$K and $T^{ar}_{c,4\frac{1}{2}} = 80.5 \pm 0.5$K. Heat capacity features for reentrant layering-transition $5\frac{1}{2}$ (not shown) are barely noticeable against the large background signal that is due

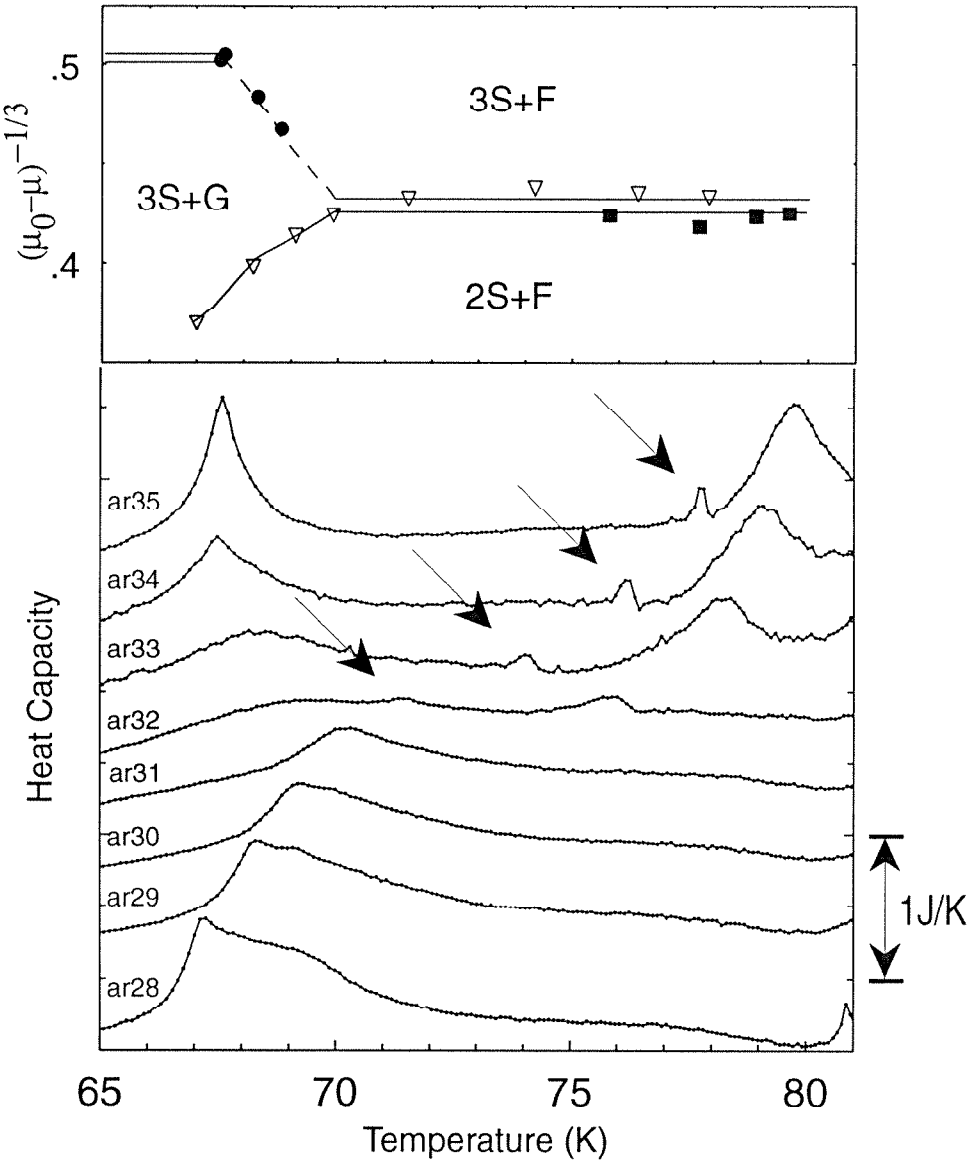

Figure 3.23: Bottom: Heat capacity scans, corrected for desorption, around reentrant layering-transition $3\frac{1}{2}$ in argon. Top: Peak locations for the scans show plotted in $(\mu_0 - \mu)^{-1/3}$ versus T. Symbols are described in the text.

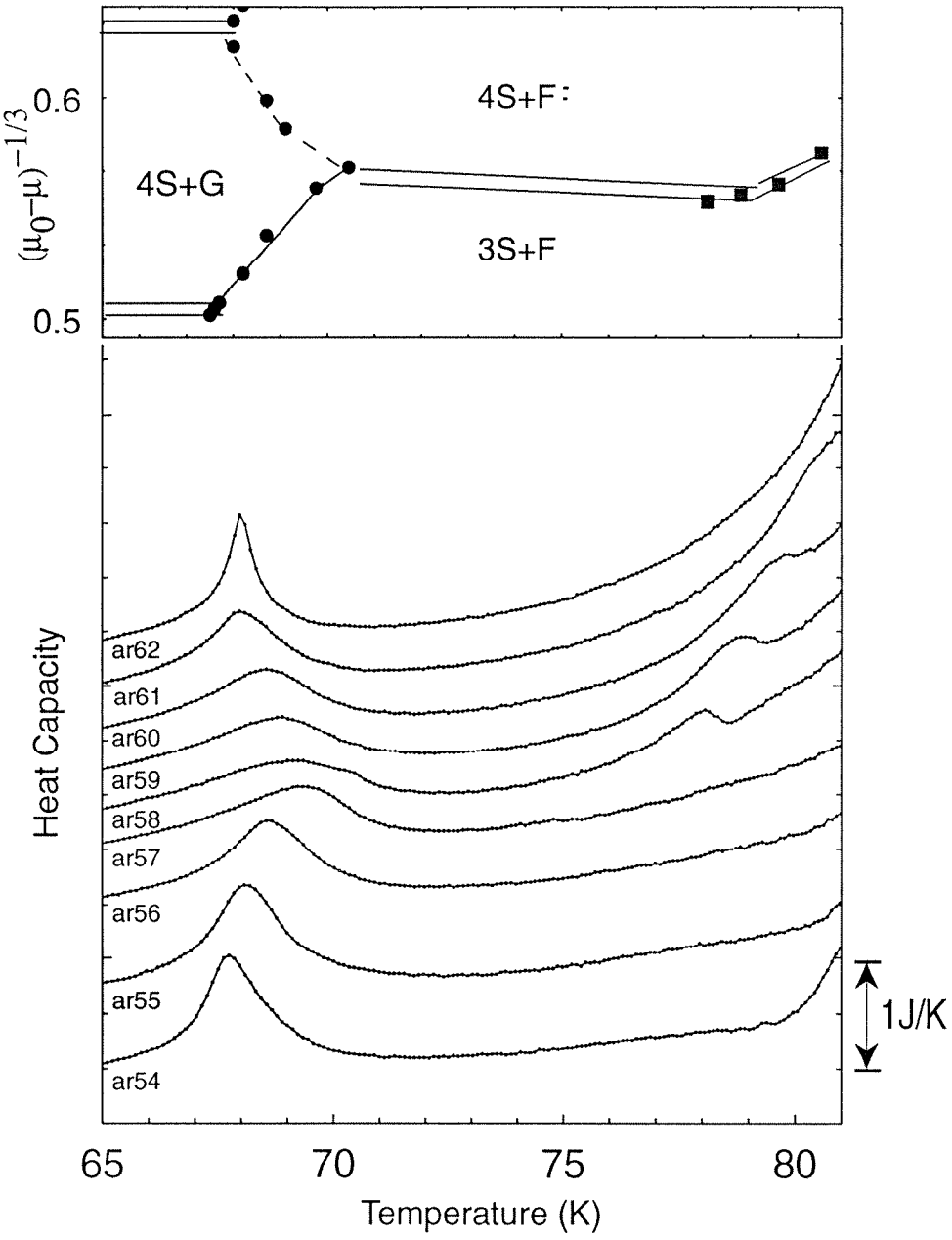

Figure 3.24: Bottom: Heat capacity scans, uncorrected for desorption, around layering-transition $4\frac{1}{2}$ in argon. Coverages at 65K are.... Top: Peak locations for the scans show plotted in $(\mu_0 - \mu)^{-1/3}$ versus T. Symbols are described in the text.

to desorption of the film and the bulk triple-point peak. At lower temperatures, however, we clearly observe the zigzag pattern of peaks (Fig. 3.25) that were found to join the endpoints of the low temperature layering-transitions with the starting points of the reentrant layering-transitions. In the next chapter we will argue that these peaks are due to a preroughening transition, so that to our knowledge, these data represent the first direct observation of preroughening.

We return now to our labeling of the various states that these phase transitions separate. The region above the third and fourth layering-transitions is labeled 3S+G in Fig. 3.23, indicating three complete solid layers and the small amount of two-dimensional gas that forms before the nucleation of the fourth layer. The forward-sloping, solid line in Fig. 3.23 was already identified as the disordering of the third layer. The phase on the other side of this line must be 2S+F, where F indicates 2D fluid. Likewise, we may label the phase at the top of Fig. 3.23 (also the phase at the bottom of Fig. 3.24) 3S+F, because this phase may be reached, from low temperature, by crossing the fourth-layer melting transition. The reentrant layering-transitions are, in general, transitions between NS+F and (N+1)S+F, between solid films with uppermost layers disordered. Youn and Hess[58, 38] find that the coverage of the film on either side of the reentrant layering-transitions is approximately half integer, so that the F actually corresponds to about one-half layer of disorder. We cannot estimate the coverages from our measurements because of the problem of capillary condensation, although we can tell that the coverages are non-integer, because the critical densities of the reentrant layering-transitions are intermediate to those of the low-temperature layering-transitions. The coverages are also difficult to estimate from the ellipsometry data, and values such as 1/3 or 2/3 are within the range of error.

The krypton data in the upper layers are nearly identical to the argon data. In Fig. 3.26 thirteen scans in the region of the $3\frac{1}{2}$ layering-transition are shown. These scans represent increments in coverage of about one tenth of a layer. The

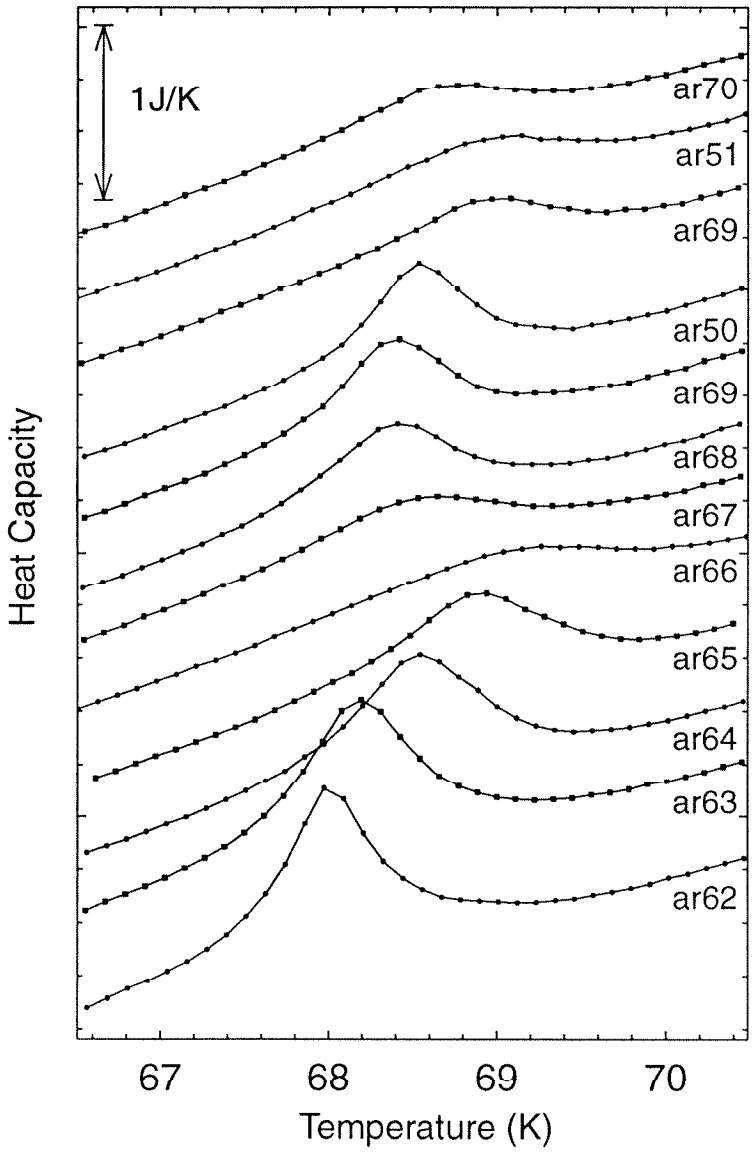

Figure 3.25: Heat capacity peaks in Ar at low temperatures for coverages higher than $3\frac{1}{2}$ layers. These peaks may be due to preroughening.

lowest coverage scans, kr47 and kr48, show the mesalike peak due to third-layer melting. Scans kr49 through kr57 show the small peak that occurs near the point where the scan enters the coexistence region, followed by the larger peak that occurs as the scans leave the coexistence region. In addition, scans kr52 and higher show the broad, rounded peak at lower temperature, which evolves into the tall, sharp peak that terminates the fourth layering-transition (scan kr59).

	Ar	Kr
$T_{t,2}$	66.0	94.4
$T_{t,3}$	66.7	95.2
$T_{t,4}$	67.5	95.1
$T_{t,5}$	68.1	95.6
$T_{t,6}$	68.4	95.8
$T_{t,7}$	$\sim$ 68.7	$\sim$ 96.1

Table 3.2: Layer triple points and endpoints of layering-transitions.

	Ar	Kr
$T_{t,3\frac{1}{2}}$	70.0	99.1
$T_{t,4\frac{1}{2}}$	70.5	97.8
$T_{t,5\frac{1}{2}}$	69.2	96.7
$T_{t,6\frac{1}{2}}$	69.0	96.3

Table 3.3: Starting points of reentrant layering-transitions.

	Ar	Kr
$T_{c,2}$	69.7	98.1
$T_{c,3}$	67.8	-
$T_{c,3\frac{1}{2}}$	79.9	113.6
$T_{c,4\frac{1}{2}}$	$\sim$ 80.5	$\sim$ 111
$T_{c,5\frac{1}{2}}$	$\sim$ 80.3	?

Table 3.4: Endpoints of reentrant layering-transitions.

The sharp rise in the heat capacity near the ends of the high-coverage scans in Fig. 3.26 is the beginning of the bulk-triple-point melting peak. The μ trajectories in Fig. 3.27 clearly show that the scans pass through a coexistence region. The locations of the small peaks are shown with filled circles in Fig. 3.27, and the broad peaks with open circles. The small peaks occur slightly before the layering-transition, and may not be directly related to it. Instead, it is likely that the small peaks are the continuation of third-layer melting, which is observed at higher temperatures and coverages. The small peaks are not seen before layering-transition $4\frac{1}{2}$, and neither is fourth-layer melting seen at higher temperatures.

Figure 3.28 shows the same zig-zag pattern of low-temperature peaks found in argon (see Fig. 3.25). These peaks may represent the preroughening transition of the 111 facet of krypton. Knowing that these peaks connect the low temperature layering-transitions to the reentrant layering-transitions, we may estimate $T_{t,n}$ and $T_{t,n+\frac{1}{2}}$ up to the sixth layer. These values, along with estimates of $T_{c,n+\frac{1}{2}}$, are given in Tables 3.2, 3.3, and 3.4 for both argon and krypton.

The multilayer phase diagrams derived from the heat capacity data are presented in Figs. 3.29 and 3.30. The meanings of the various symbols are as follows. Open circles are peaks that are due to crossing a the coexistence boundary of a low-temperature layering-transition. Open squares are second-layer melting. Crossed squares are the small peaks, tentatively identified as CI transitions, before second-layer melting. $\times$s are approximately the endpoints of the broad features that are due to second-layer melting. Inverted triangles are third-layer melting and also the small peaks before layering transition $3\frac{1}{2}$. Filled squares are the peaks observed upon leaving the reentrant layering-transitions. Filled circles are the zigzagging series of peaks at low temperatures. Double lines indicate layering-transitions, single lines are the melting of the topmost film layer, and dashed lines are the condensation of about half a disordered layer. It is not clear whether these peaks, between NS+G and NS+F, represent real phase transitions, or whether they are

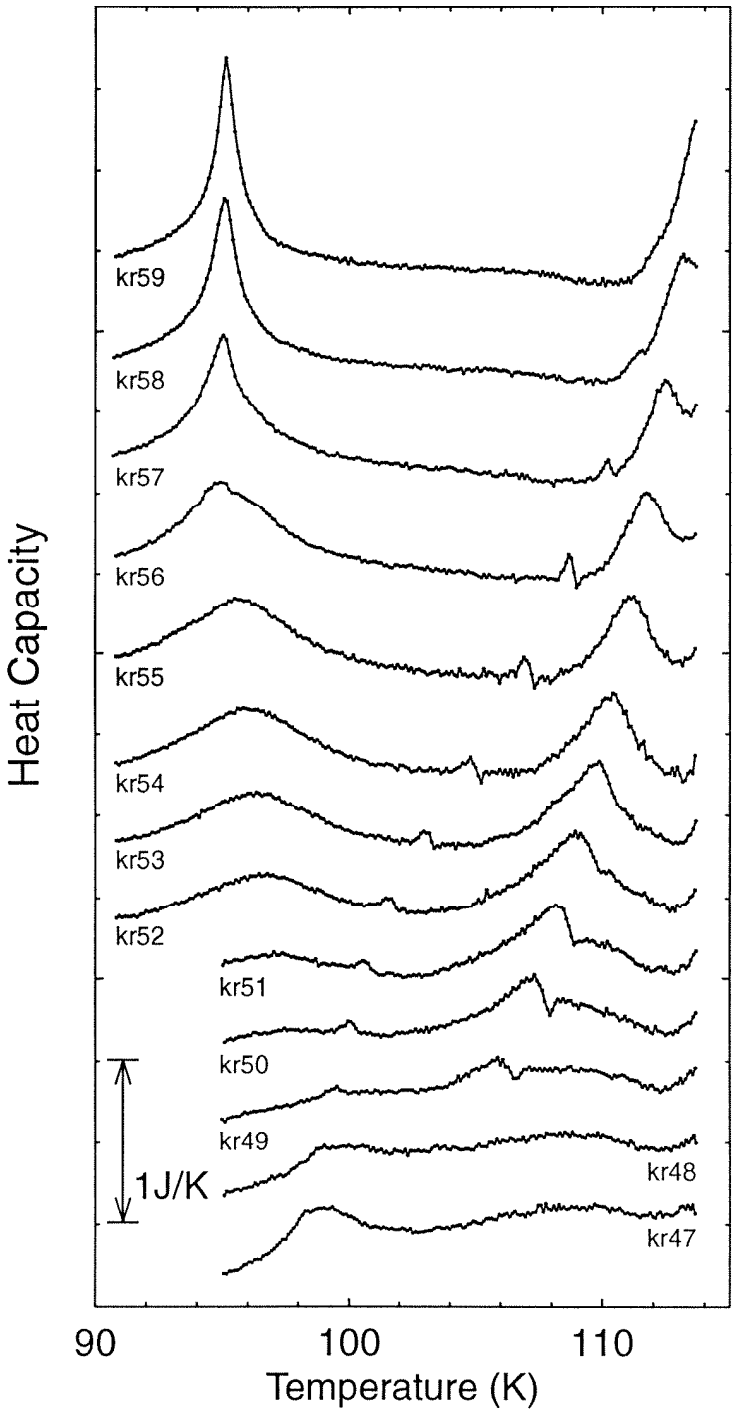

Figure 3.26: Closely spaced heat capacity scans, corrected for desorption, around reentrant layering-transition $3\frac{1}{2}$ in krypton.

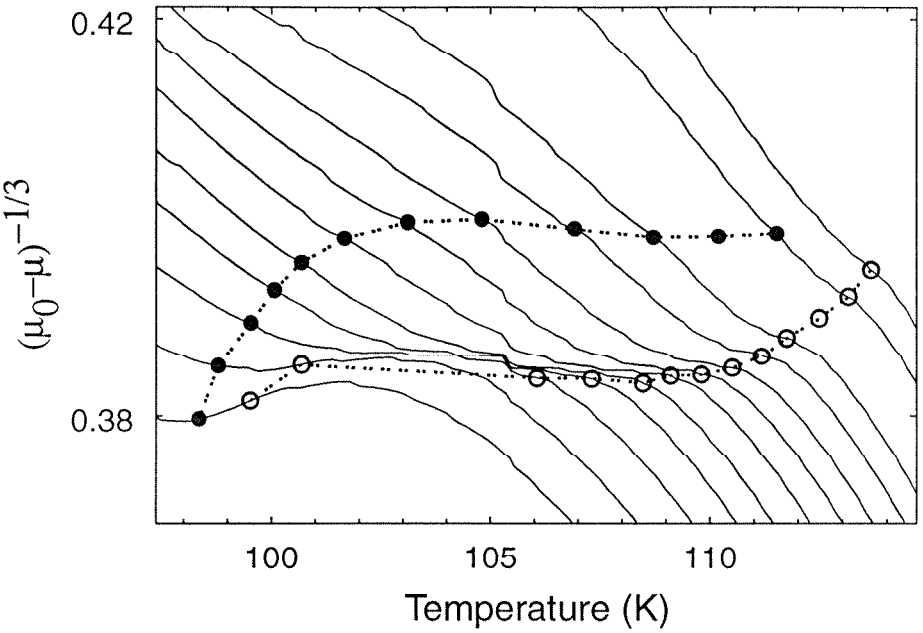

Figure 3.27: μ trajectories around reentrant layering-transition $3\frac{1}{2}$ in krypton. Open circles are the small peak in Fig. 3.26; filled circles are the peak caused by leaving the coexistence region.

just due to a rapid crossover region where about one-half layer continuously condenses.

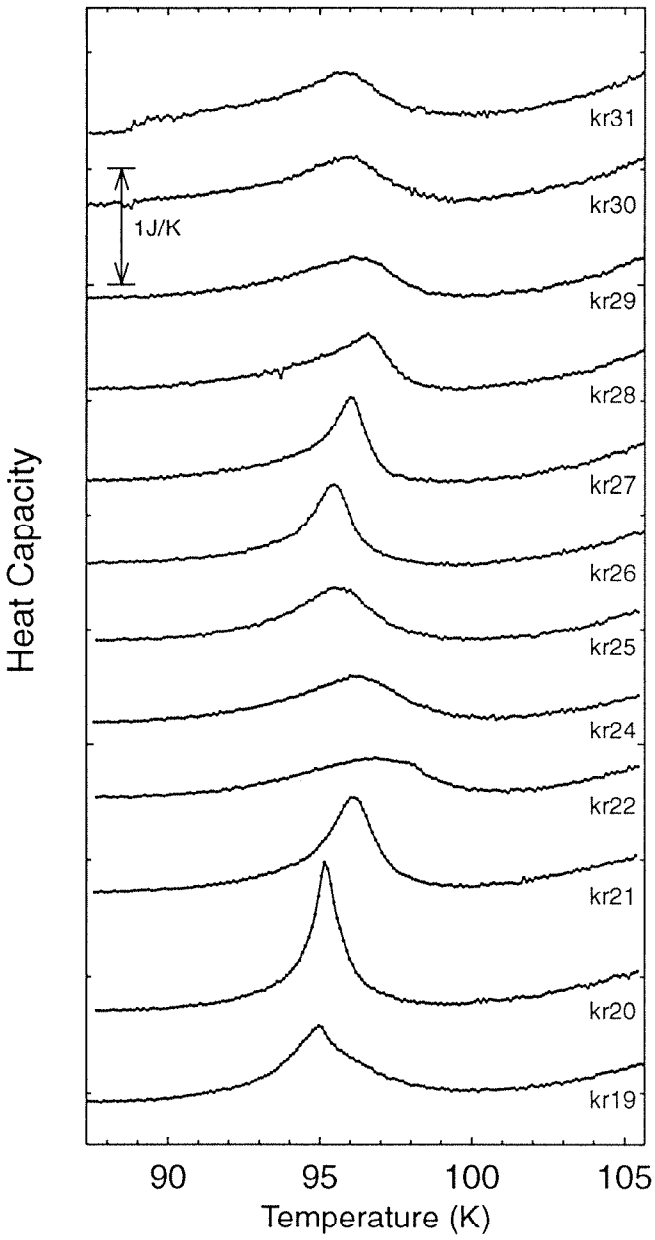

Figure 3.28: Low-temperature peaks for coverages higher than $3\frac{1}{2}$ in krypton. Heat capacities are corrected for desorption.

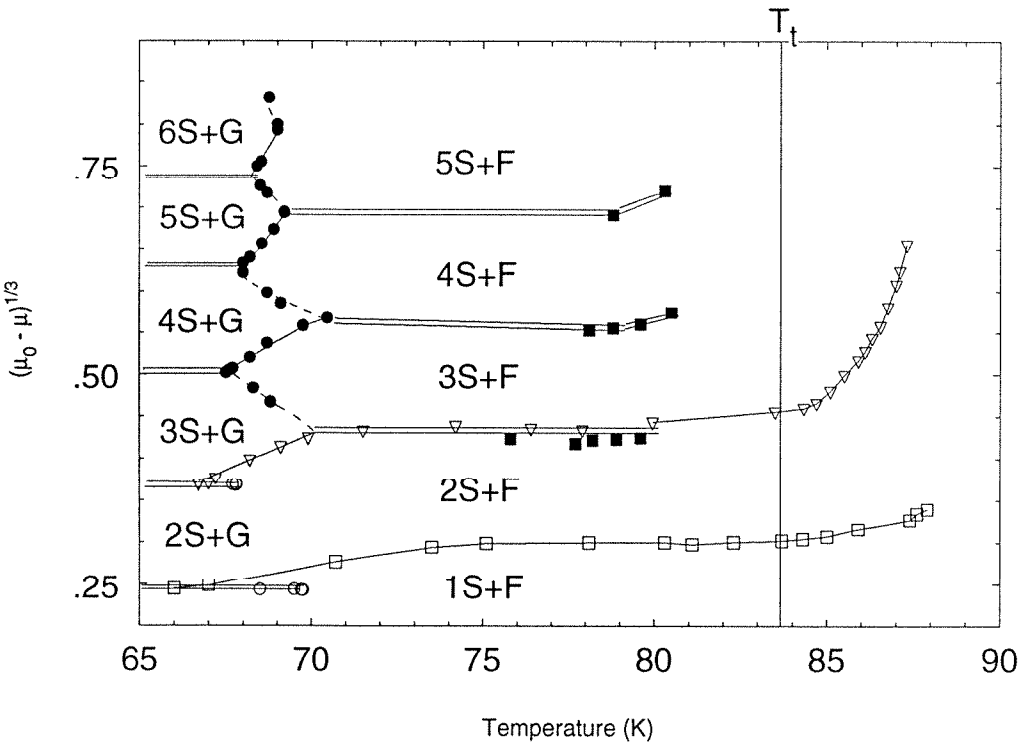

Figure 3.29: Argon/graphite multilayer phase diagram in $(\mu_0 - \mu)^{-1/3}$.

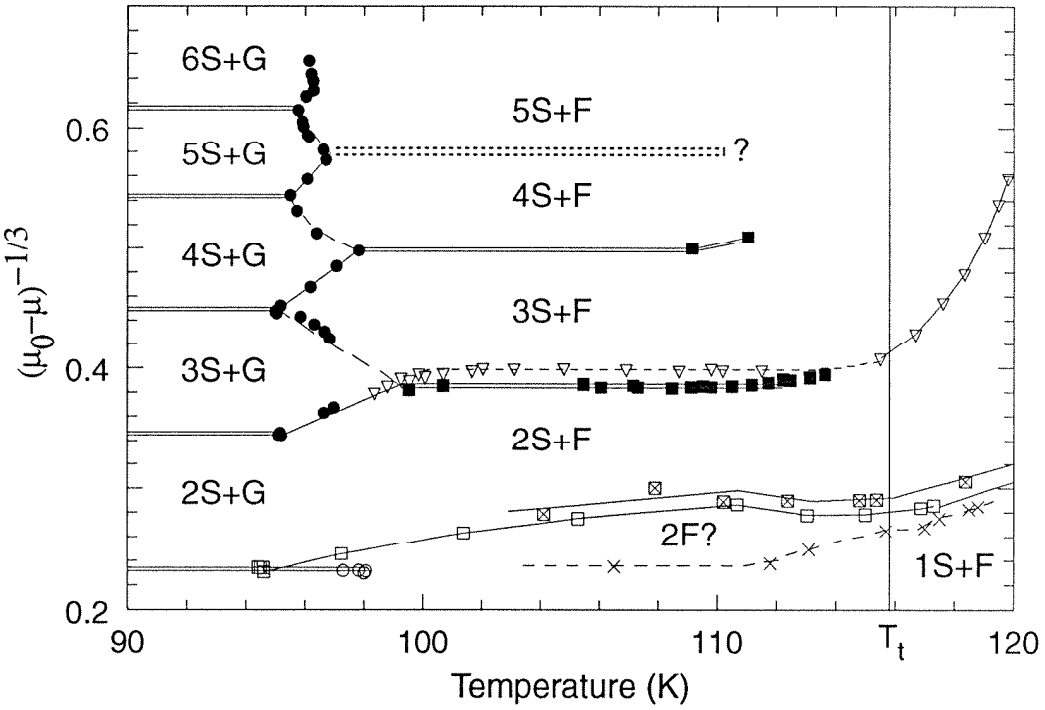

Figure 3.30: Krypton/graphite multilayer phase diagram in $(\mu_0 - \mu)^{-1/3}$.

Chapter 4

Roughening, Preroughening, and Multilayer Films

4.1 History of Roughening

The idea that a phase transition may occur at a crystal surface, independent of bulk phenomena, was due to Burton and Cabrera[70]. The idea was elaborated upon by Burton, Cabrera, and Frank (BCF)[71] in a classic paper on crystal growth. In this paper, BCF approximate the behavior of a surface with a two height model, in which the height of the surface at any point can assume only two values (Fig. 4.1). The problem is then equivalent to the 2D Ising model solved exactly by Onsager[72]. Below T_c, the 2D-Ising critical temperature, up-spins accumulate in domains because of the positive free energy of a Bloch wall between up and down spins. In the surface model, adatoms on the surface accumulate into patches(Fig. 4.1(a)). If the crystal surface were perfect, BCF expect crystal growth below T_c to occur very slowly and to depend exponentially on the oversaturation of the vapor, because growth may occur only at and around nucleation sites. At temperatures above T_c, the Ising spins no longer form domains, and the free energy of a Bloch wall has vanished . Equivalently, in the surface model, the adatoms no longer accumulate into clusters (Fig. 4.1(b)), and there is no longer a nucleation barrier to crystal growth. At these temperatures, crystal growth is expected to

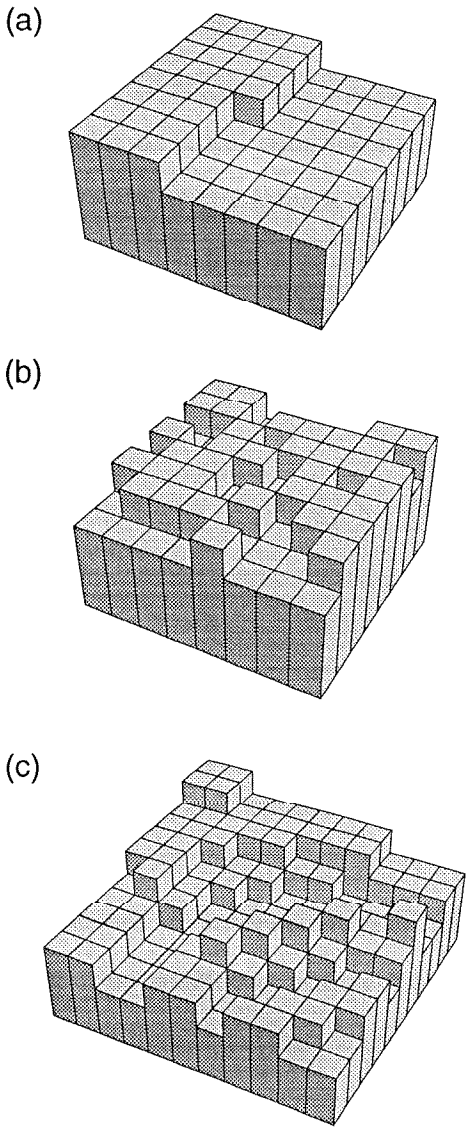

Figure 4.1: (a) The low-temperature phase of the two-height model. (b) The rough phase of the two-height model. (c) The rough phase of a general solid-on-solid model.

occur much more rapidly and to depend linearly on the oversaturation. At high temperatures the adatoms are disordered, and the surface is said to be "rough." The T_c of the 2D-Ising model is called T_R, the roughening temperature, in the surface model.

The two-height model, as BCF suggest, is not sufficient for modeling a crystal surface quantitatively. In order to study roughening, a more general model must be considered in which the height of the interface is allowed to take on any value, often restricted to integers, between plus and minus infinity. One such model is called the solid-on-solid (SOS) model. The Hamiltonian of a general SOS model is given by

$$H[\{h_i\}] = \sum_{(i,j)} V(\mid h_i - h_j \mid), \tag{4.1}$$

where $\{h_i\}$ is a two-dimensional array of column heights, and $V(\mid \delta h \mid)$ is some increasing function giving the energy between nearest-neighbor columns of different heights. A particular choice of the height-height potential, $V(\mid h_i - h_j \mid) = \mid h_i - h_j \mid$, gives the Hamiltonian of a "restricted" lattice-gas in which occupied sites may occur only above other occupied sites, so that "overhangs" are forbidden.

Monte Carlo simulations carried out on different SOS models [73] have shown a phase transition between smooth and rough surfaces. At low temperatures, the surface of the system chooses an integer average height out of the countably infinite set of such heights. The surface contains vacancies or adatoms, but the average height is fixed, and the height-difference correlation function

$$G(r) = \langle (h_0 - h_r)^2 \rangle \tag{4.2}$$

is finite in the $r \to \infty$ limit[74]. As the temperature increases, the size of clusters of adatoms and vacancies diverges, and clusters gain their own clusters of adatoms and vacancies. At temperatures above the roughening temperature, the surface contains a disordered array of steps (Fig. 4.1(c)), and the height of the interface is no longer defined for an infinite system. The roughening transition may be

characterized either by the divergence of $G(\infty)$, the interface width, or by the free energy (per unit length) of a step becoming zero[74].

More interest was developed in SOS models and roughening when it was shown that roughening is a Kosterlitz–Thouless transition. Chui and Weeks[75] first showed that the discreet Gaussian partition function

$$Z_{DG} = \int d\{h_j\} \prod_j W(h_j) \exp\left(-\frac{1}{k_B T} H_{DG}\right) \tag{4.3}$$

where

$$\begin{aligned} H_{DG} &= \tfrac{J}{2} \textstyle\sum_{j,\delta} (h_j - h_{j+\delta})^2 \\ \text{and} \quad W(h_j) &= \textstyle\sum_{n_j=-\infty}^{\infty} \delta(h_j - n_j) \end{aligned} \tag{4.4}$$

may be transformed into the partition function of a neutral 2D Coulomb gas with charges of $0, \pm 2\pi, \pm 4\pi, \ldots$. Ohta and Kawasaki[76] further showed that the partition function with

$$W(h_j) = \ln[1 + 2y_0 cos(2\pi h_i)] \tag{4.5}$$

may be transformed into a 2D Coulomb gas with charges of only $\pm 2\pi$. This partition function approximates the Sine–Gordon partition function when y_0 is small. The Sine–Gordon Hamiltonian,

$$H_{SG} = \frac{J}{2} \int dx (\nabla h)^2 - 2ya^{-2} \int dx \cos\left(2\pi h(x)\right), \tag{4.6}$$

where $h(x)$ is now a continuous variable, is used in Huse's treatment of the roughening transition in the presence of a substrate, described below. The cosine term in Eqn. (4.6) plays the role of the periodic delta function weights in Eqn. (4.4). The coefficient y of the cosine is related to the fugacity of the charges in the Coulomb-gas representation. For given fugacity, the charges are bound in + and − pairs at low Coulomb-gas temperatures. In the Sine-Gordon representation, this corresponds to the *rough* phase, so the temperatures in the two representations are inversely related. Conversely, at high Coulomb-gas temperatures, the charges unbind, and the Sine-Gordon interface localizes.

Finally, Jose *et al.*[77] showed that the SOS model was related to the planar XY model by an exact duality transformation. Thus, the roughening transition is expected to belong to a universality class, including the 2D neutral Coulomb gas, the planar XY model, and the superfluid transition in ^4He films.

The roughening transition has been verified experimentally in a study of the ^4He solid-superfluid interface[78]. Indirect evidence for roughening has also come from crystal-growth studies, where the morphology of crystals has been related to whether they were grown below or above the roughening temperature[79, 80]. Finally, some indirect evidence for roughening has come from studies of multilayer films, as will be described in the next section.

4.2 Roughening Near an Attractive Substrate

The addition of a substrate destroys the roughening transition for two reasons. First, the substrate localizes the interface and prevents the interface width from diverging. Second, the substrate provides a graduated potential that gives steps different free energies in different film layers. However, as a film grows away from the interface, the substrate has less and less influence on the surface (the Van der Waals potential falls off as $1/z^3$, where z is the distance away from the substrate), and the interface width is given more room to fluctuate. Therefore, even though a true roughening transition cannot exist in the presence of a substrate, we expect to see some related phenomenon at the surface of a thick film at around T_R, the roughening temperature of the bulk interface.

The first theoretical investigation relating the phenomenon of layering in multilayer films to the roughening transition was by De Olivera and Griffiths [48], who studied a lattice gas model of multilayer adsorption in a mean-field approximation. The effective potential used was given by

$$V_h = \begin{cases} \epsilon C/h^3 - \delta\mu\, h & \text{, for } h \geq 2 \\ \epsilon D - \delta\mu & \text{, for } h = 1 \end{cases} \tag{4.7}$$

where h is the height of the film above the substrate, $\delta\mu$ is the difference between the bulk-saturated chemical potential and the chemical potential of the system, and C and D are parameters of the Van der Waals potential. In their study they found layering transitions between films of thickness $n-1$ and n, each ending at a critical point, $T_{c,n}$. De Olivera and Griffiths found that the temperatures $T_{c,n}$ converged for infinite n to a temperature that they suggested was the roughening temperature of the bulk interface[1].

Nightingale, Saam, and Schick[49] performed a Migdal-Kadanoff approximate-renormalization group analysis of a triangular-lattice gas in the presence of a substrate. They were able to show analytically that the layering-transitions end in Ising-type critical points, as was expected. Further, they were able to show that the layering critical points should approach the bulk roughening temperature as

$$T_R - T_{c,n} \sim 1/(\log n)^2, \tag{4.8}$$

where n is the film thickness. It should be noted that this form is expected to hold only in the very thick-film limit, and is therefore impossible to verify in experiments. However, Eqn. (4.8) does predict that the layering critical points should increase toward the roughening temperature, at least for sufficiently thick films.

Perhaps the most intuitive treatment of the relationship between roughening and layering in multilayer films was given in Huse's renormalization group analysis of layering in solid films[37]. Huse considered a continuum Sine–Gordon model modified to include the substrate potential, which was essentially the same Hamiltonian considered in an approximate treatment by Weeks[81]:

$$H = \int d^2r \left[\frac{J}{2} \mid \vec{\nabla} h(\vec{r}) \mid^2 + V(h(\vec{r}))\right], \tag{4.9}$$

[1]In the De Olivera-Griffiths model, $\lim_{n\to\infty} T_{c,n} \to T_c^{bulk}$, the 3D critical temperature. De Olivera and Griffiths suggested that this result was an artifact of their mean-field approximation, and that the true limit should be T_R.

where

$$V(h) = -\delta\mu h + Ch^{-2} + ycos2\pi h + V_0. \tag{4.10}$$

The cosine term is basically the same as that of the Sine-Gordon Hamiltonian, and represents the effect of the crystal lattice that picks out integer film thicknesses. The other terms give the contribution from the substrate and the chemical potential difference. $V(h)$ is shown in Fig. 4.2. The substrate potential picks out one or two of the local minima from the infinite set of degenerate minima that would result in the limit $\delta\mu, C \rightarrow 0$. At low temperatures, the film thickness is confined to the lowest local minimum of $V(h)$. The first-order layering transitions occur at chemical potentials at which the lowest two local minima are degenerate. At these chemical potentials, the coverage increases discontinuously from N to N+1 layers.

To demonstrate that the layering transitions end in Ising critical points, Huse considered an approximation to $V(h)$ given by $V(h) \simeq -g\tilde{h}^2 + u\tilde{h}^4$, with $\tilde{h} = h - n + \frac{1}{2}$, which is a good approximation at the n^{th} layering-transition if n is small. With this potential, the problem reduces to a continuous-spin Ising model. The approximate potential limits the system to a two-height model, which should hold when large fluctuations of the interface are strongly discouraged by the substrate. In the limit that $\delta\mu \rightarrow 0$ (Fig. 4.2 (b)), it is no longer a good approximation to consider only two values of the height, and thus a crossover is expected between the Ising-like behavior in thin films to rougheninglike behavior in thick films. Further, the critical points of the layering-transitions should converge to the roughening temperature in the limit of infinite film thickness. The same asymptotic behavior of $T_{c,n}$ was found as in the Nightingale study.

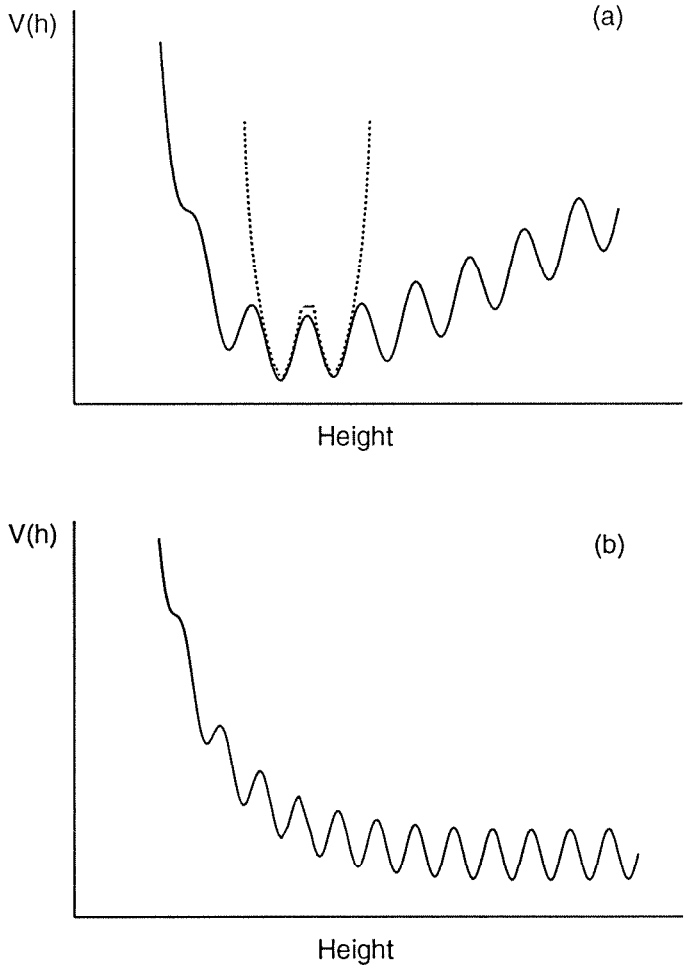

Figure 4.2: The pseudopotential used in Huse's treatment of the layering problem. (a) Near the layering-transition between 3 and 4 layer films. For thin films, fluctuations to other film thicknesses are suppressed, and the potential may be approximated by the dashed function shown. (b) For thicker films, several minima have nearly degenerate energies.

4.3 Preroughening at the Crystal Interface

A new phase transition, related to roughening, was recently proposed by Rommelse and den Nijs[82]; den Nijs[83, 84, 85]. In previous theories of roughening, the disordering of the surface layer was enough to cause the interface width to diverge. The new theory suggests that it may be possible for the surface to disorder at a preroughening transition (PR), but for the interface width to remain finite until the roughening transition occurs at a higher temperature. This scenario may be realized if a phase exists in which upsteps and downsteps have a sort of antiferromagnetic order. Figure 4.3 shows two surface configurations. Steps in the surface are denoted by lines with arrows, so that the height is greater by one unit to the right of an arrow. Figure 4.3(a) shows a configuration in which two upsteps are nested so that the height of the interface changes by two units. Figure 4.3(b) shows a situation in which an up-down step order persists so that the height of the interface fluctuates at most by one. Den Nijs suggests that configuration (b) may be thermodynamically preferred if a repulsive interaction exists between parallel arrows (steps in the same direction), but either no interaction or an attractive interaction exists between antiparallel arrows. In this case, surface configurations with an up-down step order will possess more meander entropy, because antiparallel arrows may approach each other and intertwine, whereas parallel arrows are forbidden to approach to within some interaction range.

The new phase is called the disordered flat phase (DOF) because the surface contains a disordered array of steps, but remains flat on the average. Den Nijs showed that the DOF phase exists in a restricted solid-on-solid (RSOS) model with second nearest-neighbor interactions. The restriction in this model is that nearest-neighbor heights differ at most by one. This restriction is imposed for technical reasons (so that the model may be treated with the transfer-matrix method, and because the model may be considered as a body-centered solid-

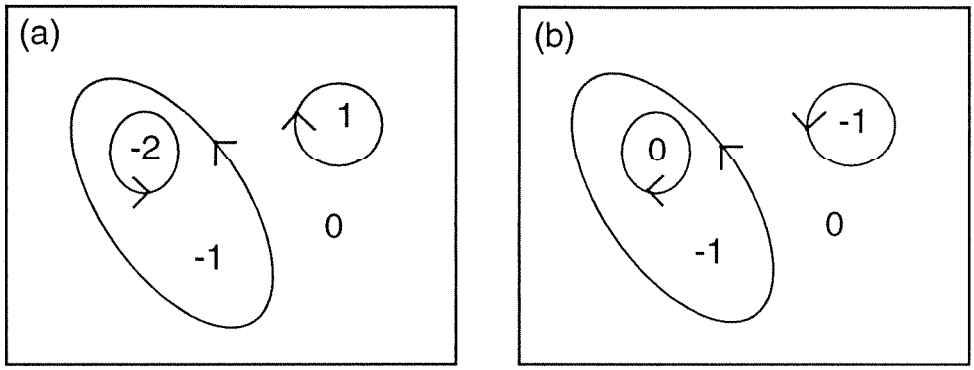

Figure 4.3: (a) A surface configuration showing a rough surface. (b) A surface with an up–down (DOF) step order.

on-solid (BCSOS) model on a bond-diluted lattice) and should not, by itself, stabilize the DOF phase. In this model, second nearest-neighbor interactions are introduced to generate the repulsion between up–up steps, as can be seen from Fig. 4.4. If only nearest-neighbor interactions were considered, the two plaquettes shown would have the same energy. The second nearest-neighbor interaction, however, causes the plaquette with the up–down step order to be energetically favored.

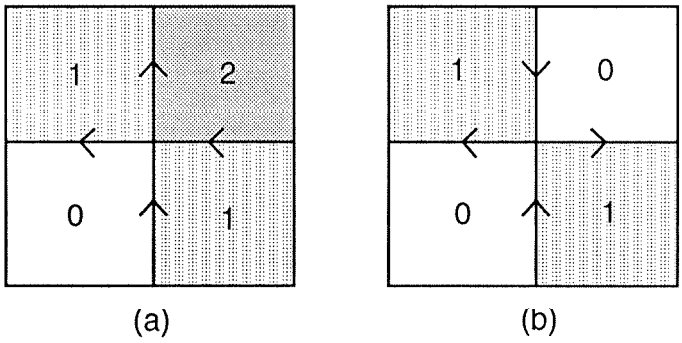

Figure 4.4: The energy difference between the two plaquette configurations is due to next-nearest-neighbor (diagonal) interactions. (a) parallel arrows (b) antiparrallel arrows.

At T_{PR}, the PR temperature, the surface changes from the ordered flat (OF) phase, with integer height, to the disordered flat phase, with average height equal

to $\frac{1}{2}$ mod(1) (because of the symmetry between up and down steps). At the roughening temperature, the interface width diverges, and the average height is no longer defined. The existence of preroughening in the RSOS model depends on the ratio between the next-nearest-neighbor and nearest-neighbor interaction energies. For ratios of $E(nnn)/E(nn)$ below a critical value, a system will go directly from the OF phase to the rough phase. For $E(nnn)/E(nn)$ above that value, the DOF phase will exist between OF and rough phases. Accordingly, it is expected that some crystal surfaces may support a DOF phase, while others may not, depending on the magnitudes of the microscopic interactions. The critical ratio depends on the symmetry of the specific system and also on more general terms that may enter the Hamiltonian (e.g., third nearest-neighbor interactions) so it is not possible to predict the category into which most real systems fall.

In the Coulomb-gas representation, the PR transition represents a natural extension of the roughening transition. den Nijs[84] considers a Sine–Gordon model given by

$$\mathcal{H} = \int d\vec{r} \left\{ \frac{1}{2} K_g (\vec{\nabla}\phi_r)^2 - (u_2^2 + H^2)^{1/2} \cos 2\pi(\phi_r - \theta) - u_4 \cos 4\pi\phi_r \right\} , \quad (4.11)$$

where ϕ_r is the average height of the interface and $\tan 2\pi\theta = H/u_2$. Here, H and θ arise from an extra term in the Hamiltonian that breaks the up down symmetry of the problem. For $H = 0$, Eqn. (4.11) is equivalent to a Coulomb gas with two types of charges, ± 2 charges with fugacity u_2 and ± 4 charges with fugacity u_4. The PR transition occurs when u_2 changes sign, where the ± 2 charges are absent, but the ± 4 charges are still bound.

A substrate may be regarded as having approximately the same effect as the symmetry-breaking field, H, in Eqn. (4.11). For non-zero H, the u_2 term does not change sign abruptly across the PR transition. Rather, the average height crosses smoothly from 0 mod(1) to $\frac{1}{2}$ mod(1). Thus, the preroughening transition becomes washed out as does the critical transition of a ferromagnet in a small magnetic field.

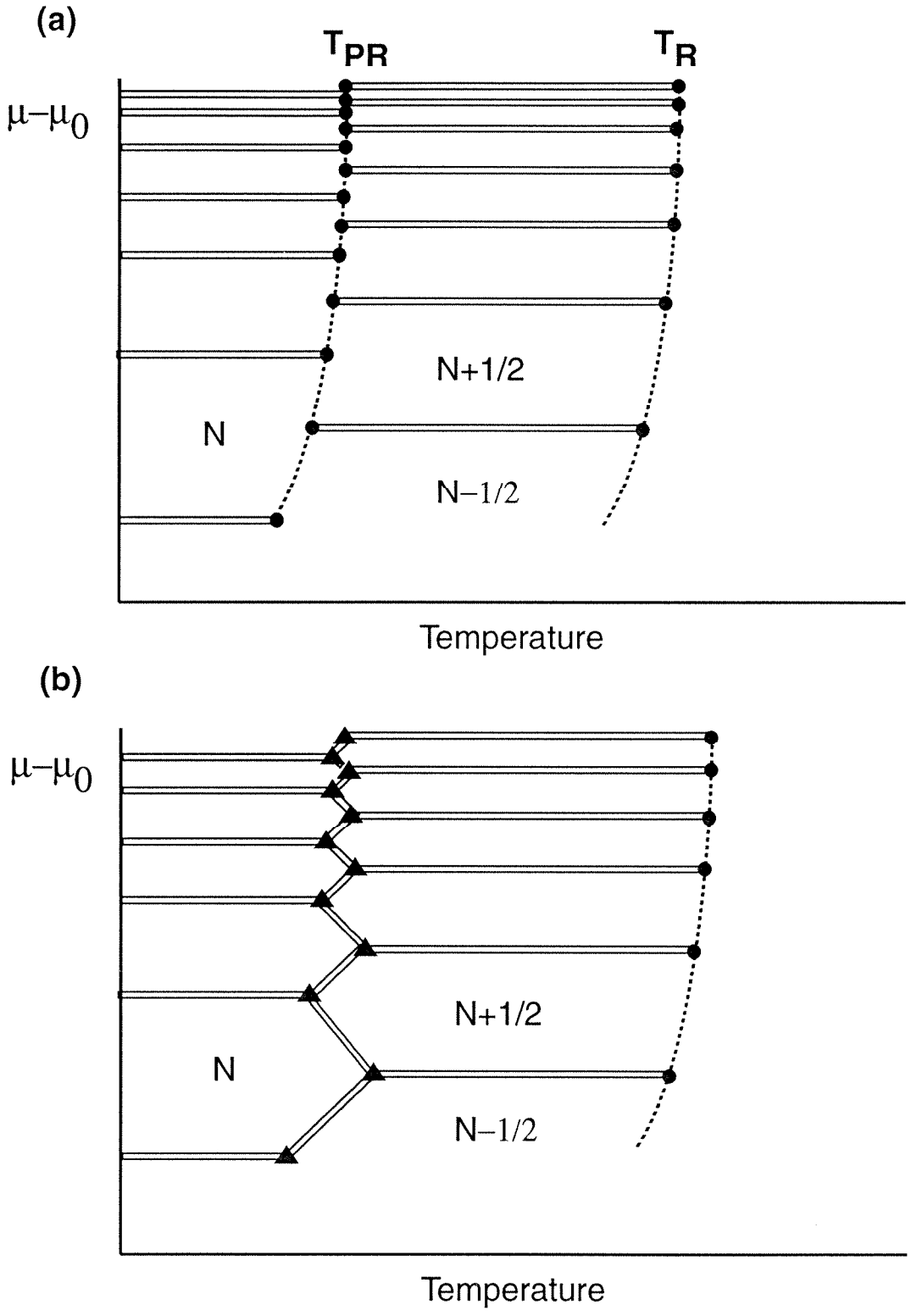

Figure 4.5: Possibilities for multilayer phase diagrams when a preroughening transition occurs at the crystal surface.

Because the height fluctuations across the preroughening transition are limited to the top few layers, it is expected that PR should have an analogue in thin films, perhaps more so than the roughening transition. Den Nijs[85] speculates that PR may be visible in multilayer film studies from the locations of the layering transitions. At temperatures $T \lesssim T_{PR}$, corresponding to a flat crystal interface, the surface prefers an occupancy of 0 mod(1), so the layering-transitions should occur between integer coverages. At temperatures $T_{PR} \lesssim T \lesssim T_R$, the surface prefers a coverage of $\frac{1}{2}$ mod(1), so the layering-transitions should occur between films of half-integer coverage. In thinner films where the symmetry breaking field is larger, there should be a gradual crossover between the two regimes. Figure 4.5 shows two possible multilayer film phase diagrams suggested by den Nijs for the case where a PR transition exists. In case (a), the low temperature layering-transitions end in critical points, and at a slightly higher temperature, reentrant layering-transitions appear at intermediate coverages. The reentrant transitions begin and end in layering critical points. In case (b), the low-temperature and reentrant layering transitions are joined together by first-order lines. The low-temperature layering-transitions end at triple points at which films of coverage N, N+1/2, and N+1 layers coexist. Similarly, the reentrant transitions begin at triple points where films of coverage N-1/2, N, and N+1/2 coexist.

4.4 Comparison with the Data

Preroughening is a very appealing explanation for the multilayer phase diagrams presented in figs. (3.29) and (3.30). PR was originally suggested as an explaination for the ellipsometry data on the basis that the shifts observed in the layering-transitions implied a shift in the surface coverage to non-integer values. Youn and Hess[58, 38] found that the surface occupancy at the reentrant layering-transitions was approximatcly 0.7 layers. This value is consistent with the heat capacity data,

and is certainly, within the experimental accuracy, consistent with 1/2, the value for the DOF phase in the RSOS model on a square lattice. At low coverages, where the number resolution of the ellipsometry data is best, the surface occupancy may be shifted by the substrate potential. Also, it is not clear whether for a triangular (or FCC) lattice, the DOF phase should have a surface occupancy of 1/2. Values such as 1/3 or 2/3 may also be possible, but excluding reconstructed phases, preroughening is the only known explanation for a non-integer surface occupancy.

In this study, we have shown that heat capacity peaks exist in the temperature region where layering is observed to shift to non-integer coverages ($\sim$ 68K for argon and $\sim$ 96K for krypton). These peaks zigzag in the chemical potential versus temperature plane. At high coverage, the peaks converge in temperature, so it seems reasonable to assume that they represent a phase transition of the bulk interface that is modified by the presence of the substrate. Because layering continues at higher temperatures, this phase transition cannot be roughening. Again, except for a possible surface reconstruction transition, the only available explanation is preroughening.

The experimental data are not conclusive as to the existence of preroughening at the 111 surfaces of argon and krypton. To prove that PR does occur at these surfaces, it will be necessary to compare the heat capacity and ellipsometry data with scattering results. The results of this study and the study of Youn and Hess, however, are very suggestive.

If our interpretion of the data is correct, then the 111 facets of argon and krypton preroughen at 69K and 96K, respectively. The roughening temperatures, estimated from the endpoints of the reentrant layering transitions, are approximately 80K for argon and 100K for krypton. The heat capacity peaks associated with preroughening are much larger than the heat capacity anomalies at the higher temperature associated with roughening. The roughening transition is an infinite-order phase transition, so the heat capacity and all of its derivatives should be

continuous. Therefore, the heat capacity signal for a roughening transition is essentially non-existent. For PR, however, the specific heat exponent is predicted to vary continuously between $-\infty$ and 2/3, depending on the microscopic parameters, so although the form of the heat capacity signal cannot be predicted from the theory, it may be expected to be larger that the heat capacity signal for roughening.

Many aspects of the multilayer phase diagrams remain unexplained by den Nijs' theory. For example, at low coverages, we find that the transition from the flat phase (layering-transitions) to the DOF phase (reentrant layering transitions) occurs over a range of temperatures. In addition, the DOF phase does not exist at all for films of under three layers. The "spreading out" of the PR transition may be explained qualitatively from den Nijs' work by assuming that the substrate has the same effect as the symetery-breaking field, but there is no simple way to see why the DOF phase should disappear completely. Both of these questions are important if we wish to use adsorbed films to study PR. In the next section, we try to answer them, using a mean-field theory.

4.5 Mean-Field Theory of Reentrant Layering

A mean-field theory was developed to study reentrant layering by Day and Weichman [86]. The approach used was similar to the one used by De Olivera and Griffiths, except that a solid-on-solid model is considered instead of a lattice-gas model, and next-nearest-neighbor interactions are added. The Hamiltonian is

$$\mathcal{H}_{SOS} = K \sum_{<r,r'>} \mid h_r - h_{r'} \mid^{p_1} + L \sum_{\ll r,r'' \gg} \mid h_r - h_{r''} \mid^{p_2} + \sum_r V(h_r), \qquad (4.12)$$

where h_r is the integer height of the column at lattice site r of a square lattice, $\langle r, r' \rangle$ denotes the sum restricted to nearest neighbor columns, $\langle\langle r, r'' \rangle\rangle$ is the sum restricted to next nearest-neighbor columns, and K and L are the nearest and next-nearest-neighbor interaction constants. For the mean-field approach, p_1 and

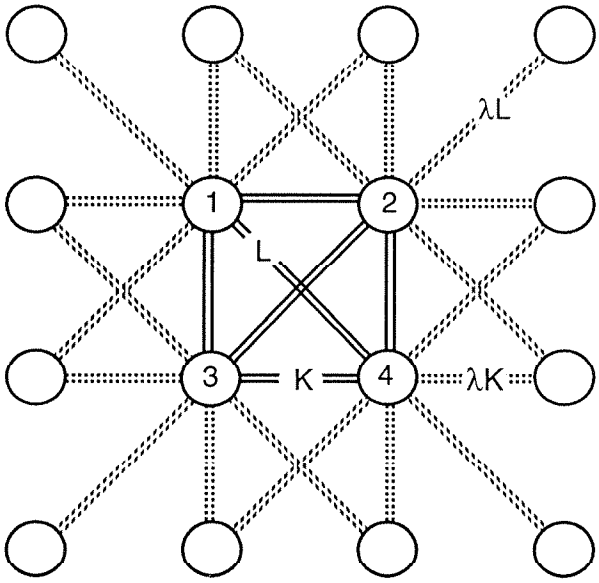

Figure 4.6: A trace is taken over all configurations of four columns. All other columns are taken to have height m.

p_2 should be chosen to be even so that the resulting free energy is analytic. The substrate pseudopotential, $V(h)$, is essentially the same as the one used by De Olivera and Griffiths,

$$V(h) = \frac{A}{h^2} - h\,\delta\mu\ . \tag{4.13}$$

The height, h_0, that minimizes $V(h)$, giving the energetically preferred column height, may be expressed as a function of the chemical potential:

$$h_0 = \left(\frac{-\delta\mu}{2A}\right)^{-1/3}\ . \tag{4.14}$$

To implement the mean-field approximation, consider a block of four columns with integer heights h_1, h_2, h_3, and h_4. All other columns in the system are taken to have the average (continuously varying) height m. Using Fig. 4.6, we may write the mean-field Hamiltonian as

$$\begin{aligned}\mathcal{H}_{MF} = \ & K[(h_1-h_2)^{p_1}+(h_2-h_3)^{p_1}+(h_3-h_4)^{p_1}+(h_4-h_1)^{p_1}] \\ & +L[(h_1-h_2)^{p_2}+(h_2-h_3)^{p_2}+(h_3-h_4)^{p_2}+(h_4-h_1)^{p_2}] \\ & +2\lambda K[(h_1-m)^{p_1}+(h_2-m)^{p_1}+(h_3-m)^{p_1}+(h_4-m)^{p_1}] \\ & +3\lambda L[(h_1-m)^{p_2}+(h_2-m)^{p_2}+(h_3-m)^{p_2}+(h_4-m)^{p_2}] \\ & +V(h_1)+V(h_2)+V(h_3)+V(h_4).\end{aligned} \tag{4.15}$$

Note that bonds between the four central columns contribute a full K or L, whereas bonds between one of the four central columns and the mean-field contribute λK or λL, where λ, introduced purely for convenience, is a tunable parameter that may be interpreted as increasing (as $\lambda \to 0$) the effect of thermal fluctuations. At this point, we choose $\lambda = 1/2$, because this choice gives the closest agreement with den Nijs' results. The mean-field free energy is found from

$$\mathcal{F}_{MF} = -\frac{1}{4} \ln \left\{ \mathrm{tr} \left(e^{-\mathcal{H}_{MF}/k_B T} \right) \right\}, \tag{4.16}$$

where the trace is over all possibilities for $\{h_1, h_2, h_3, h_4\}$. For computational purposes, only h_i within a certain range, $0 \leq h_i \leq h_{max}$ are considered. The restriction of the RSOS model may be put in by tracing over only the states for which nearest neighbor column heights differ at most by one. Alternatively, the restriction may be left out, although the number of states that must be summed over then varies as h_{max}^4.

With the choice $p_1, p_2 = 2$ we may see that the self-consistency condition, $\langle h_i \rangle = m$, holds for the value of m minimizing $\mathcal{F}_{MF}$:

$$\begin{aligned} & \frac{\partial \mathcal{F}_{MF}}{\partial m} = 2\lambda(K + \tfrac{3}{2}L) \sum_i (h_i - m) = 0 \\ \Rightarrow \quad & \tfrac{1}{4} \sum_i h_i = \langle h_i \rangle = m. \end{aligned} \tag{4.17}$$

Thus $\langle h \rangle$ may be found for various values of the parameters, K, L, Λ, and $\delta\mu$ by minimizing $\mathcal{F}_{MF}$ with respect to m.

The problem is to discover under what conditions spontaneous symmetry breaking between disordered phases may be found. As was shown in the discussion of roughening, the flat phase of a crystal interface results from the interface's spontaneously choosing one column height out of an infinite set of energetically degenerate possibilities. Likewise, the disordered flat phase occurs when the column heights are allowed to have either of two values, that is, when the average column height is approximately half-integer. Consider a five-height model (a spin-two Ising model), where the heights may take on values $h_i = \{0, 1, 2, 3, 4\}$, with

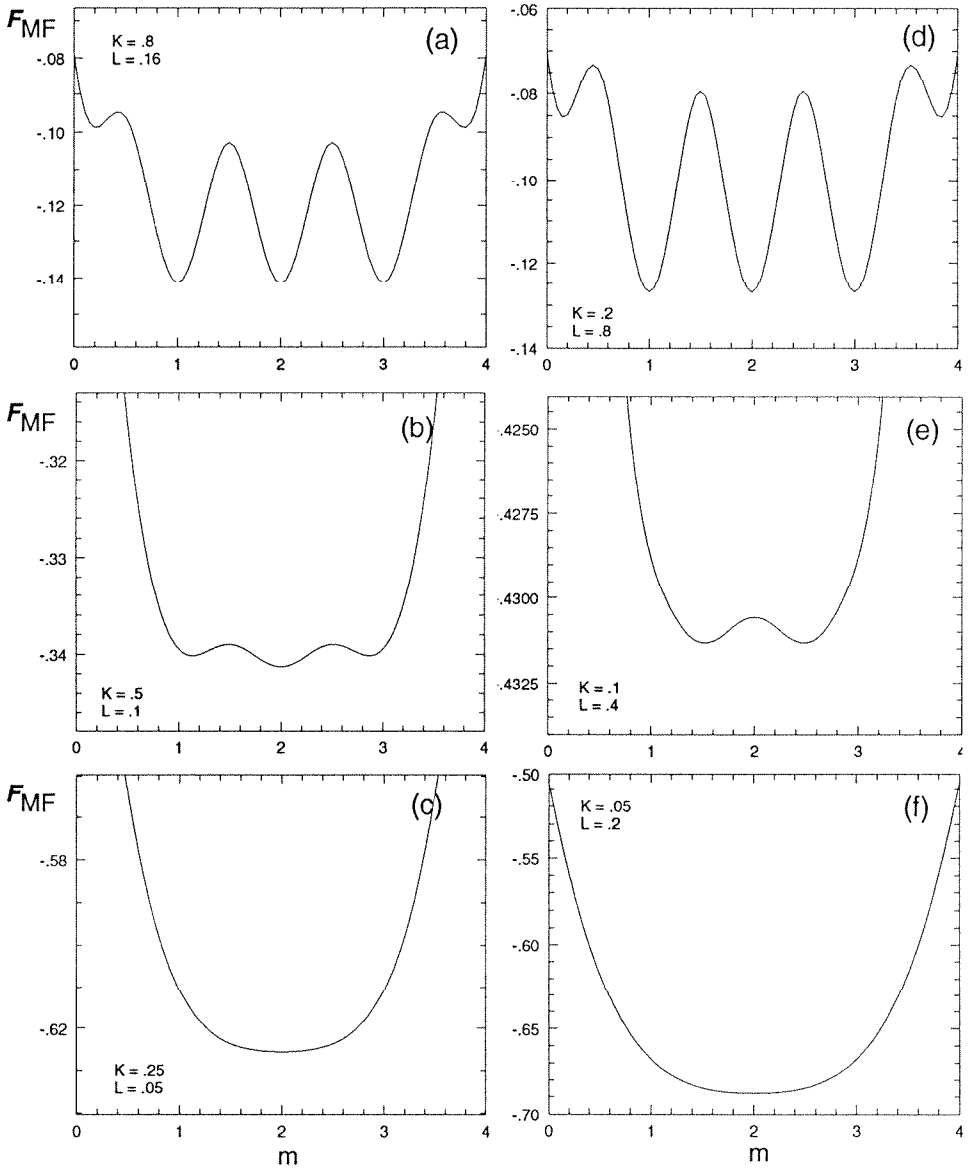

Figure 4.7: $\mathcal{F}_{MF}$ plotted versus m for various values of the parameters.

the restriction on nearest-neighbor column heights. Plots of F_{MF} versus m are given in Fig. 4.7 for zero substrate potential and various values of the parameters, K and L. For $K \gg L$ and $K \gtrsim 0.4$, corresponding to large nearest neighbor-interactions and low temperatures, F_{MF} shows three nearly degenerate minima at integer values. The steep rise in F_{MF} near $m = 0$ and $m = 4$, and the non-degeneracy of the minima at $m = 1$ and $m = 2$ are caused by the boundaries imposed on the system. This region in parameter space corresponds to the OF phase, because the height of the interface chooses one of the local minima in F_{MF}, where the four column heights average to a nearly integer value. For $K \ll L$ and $K \lesssim 0.4$, corresponding to large nearest-neighbor interactions and high temperature, there are no local minima, only a broad minimum at $h = 2$ that is due to the boundaries on the system. As $h_{max} \to \infty$, F_{MF} becomes arbitrarily flat. This region corresponds to the rough phase, where the interface is disordered (and hence does not choose any particular column height).

For $L \gg K$, the same behavior is seen in the high and low-temperature limits. At intermediate temperatures, however, a new state is found in which local minima appear at half-integer average column heights. In this case, the minima at $h = 1.5$ and 2.5 are exactly degenerate, because the problem is symmetric about $h = 2$. This region of parameter space is identified with the DOF phase. For negative coupling constants it may be possible to find ordered phases with half-integer average heights (reconstructed phases), but these are not expected to occur when the coupling constants are positive. It is possible to investigate reconstructed phases in the model by considering separate mean-fields on two sublattices, but that would take us away from the problem at hand.

The region of the phase diagram corresponding to the DOF phase may be identified by finding K and L for which the inverse compressibility, χ^{-1}, evaluated at $m = 2$, is negative. This procedure identifies the region where coexistence between disordered flat phases near $m = 1.5$ and $m = 2.5$ are expected. The

inverse compressibility is calculated from

$$\chi^{-1} = \left.\frac{\partial^2 \mathcal{F}_{MF}}{\partial m^2}\right|_{m=2}.$$

The resulting phase diagram is shown in Fig. 4.8(a). This phase diagram is very similar to the one presented by den Nijs in his treatment of the RSOS model. The dashed lines in Fig. 4.8(a) represent possible realizations of systems with fixed ratios between nearest and next-nearest-neighbor coupling energies. Varying temperature is equivalent to moving along one of the dashed lines shown. The existence of the DOF phase between the OF phase at low temperature and the rough phase at high temperature depends on the ratio K/L.

The effect of a substrate interaction on the system may be investigated by introducing a simplified substrate field, $V_2 = H(h-2) + H_2(h-2)^2$. V_2 may be thought of as a parabolic fit to the minimum of the actual Van der Waals potential. We are interested in the effect of H_2 on the spontaneous symmetry breaking around $h = 2$, and so take $H = 0$. Using this form of the potential, we may investigate the substrate interaction by varying only one parameter, H_2. Figures 4.8(b) and (c) show the result of calculating $\chi(K/T, L/T, H_2/T)$ for different values of H_2. We see that by increasing H_2, the DOF region shrinks, so that the substrate interaction may be expected to discourage the DOF phase (as manifested by the reentrant layering-transitions) at the surface of a film. The magnitude of this effect should vary from substrate to substrate. The effective H_2 should decrease as the interface moves away from the substrate, so thicker films may be expected to undergo a PR transition when thinner films do not.

To investigate multilayer phase diagrams using the mean-field theory, we keep the full form of the substrate potential given by Eqn. (4.13) and take $h_{max} = 20$. The film thickness is calculated as a function of chemical potential by minimizing $\mathcal{F}_{MF}(m)$. Layering-transitions may be identified by finding values of μ for which adjacent minima are degenerate. The C program written to do this calculation

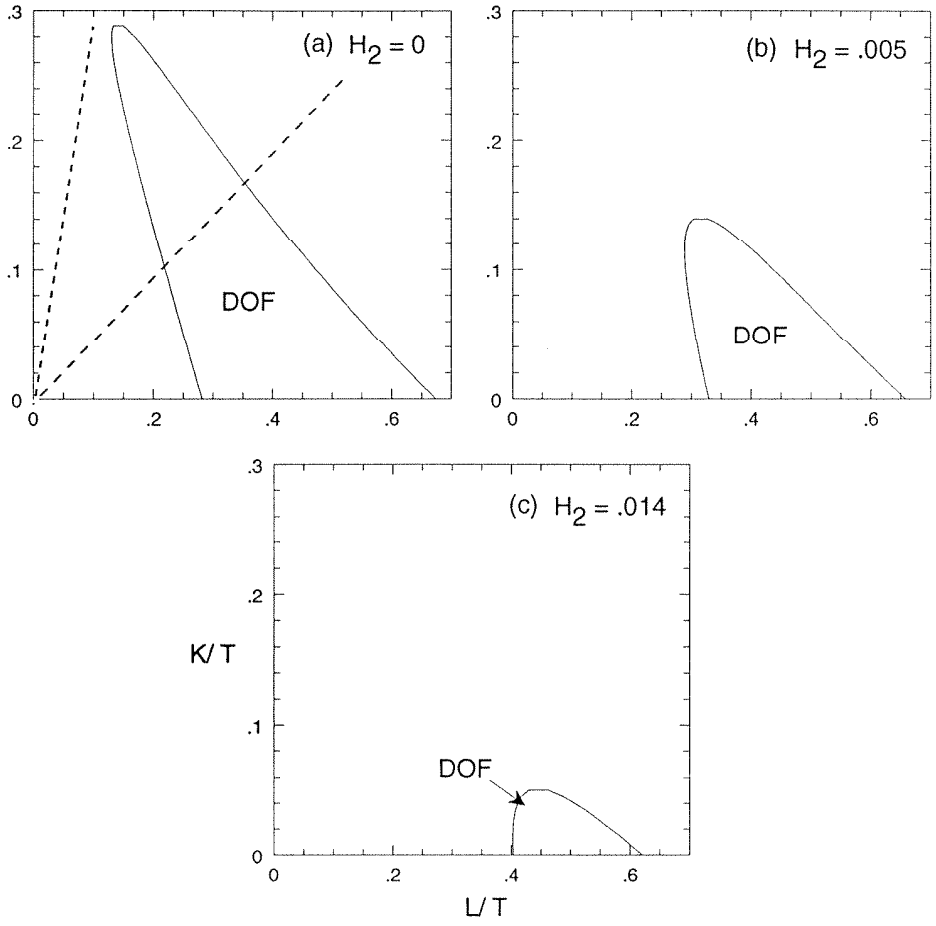

Figure 4.8: Surface phase diagrams calculated using the five-height model. The size of the DOF region decreases with increasing H2.

actually minimizes the absolute value of the difference between adjacent minima with respect to the chemical potential difference. The locations of the layering-transitions for various values of A, the substrate interaction parameter, and K/L, the ratio of nearest to next nearest neighbor coupling parameters, are shown in Fig. 4.9. The ordinate used is h_0, given by Eqn. (4.14). The N versus T phase diagram may be calculated by recording the m values of the degenerate minima at the layering-transition.

The calculated phase diagrams are similar to the one suggested by den Nijs (Fig. 4.5). Reentrant layering-transitions appear at values of h_0 midway between

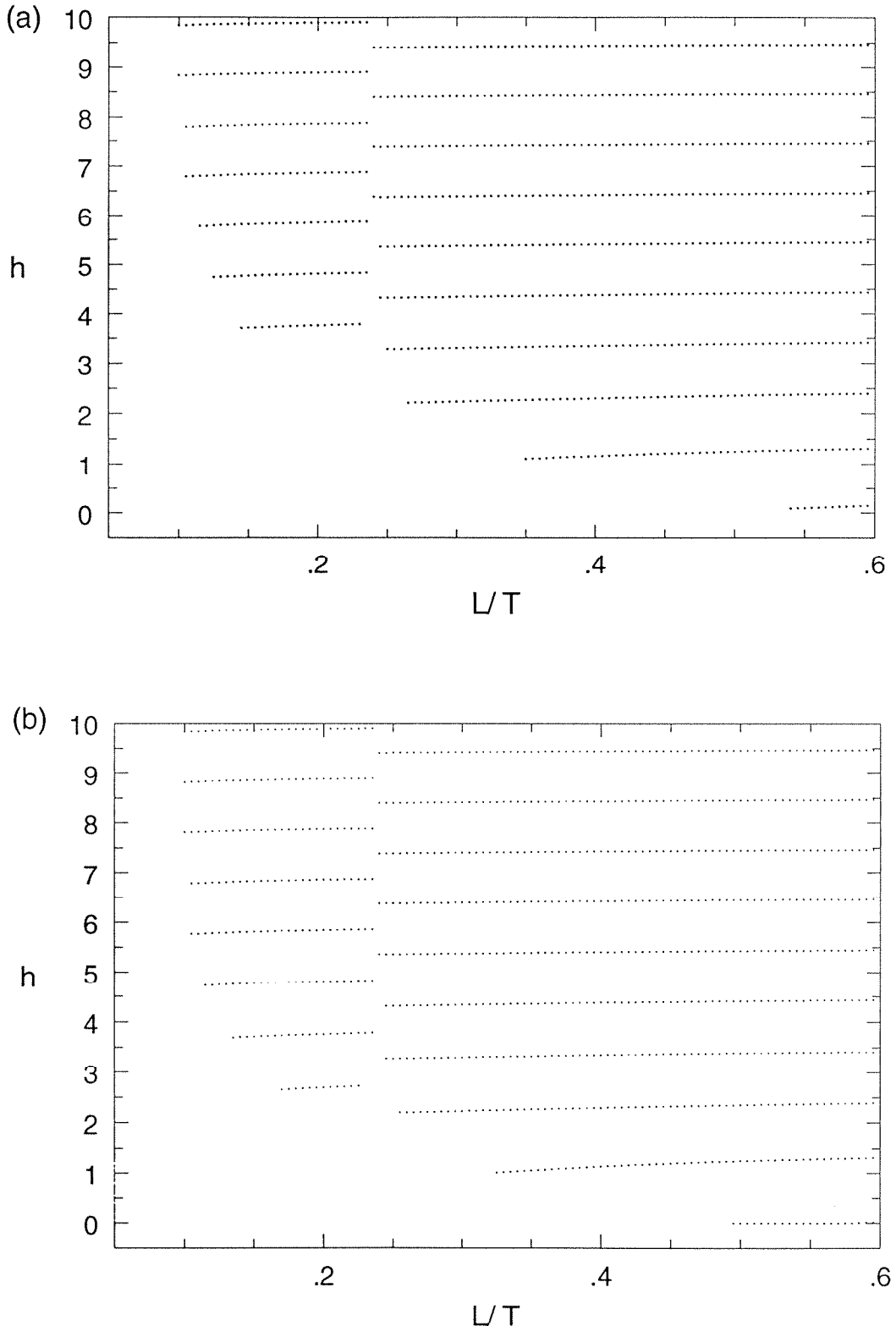

Figure 4.9: Examples of calculated phase diagrams in $(h, L/T)$ for (a) L/K = 1, A/K = 0.1; (b) L/K = 1, A/K = 0.05. High temperature is to the left; low temperature is to the right.

those of the low-temperature layering-transitions. h_0 is not exactly an integer (half integer) at the low-temperature (reentrant) layering-transitions for low coverages, although as the coverage increases, the expected behavior is found. The phase diagrams of Fig. 4.9, however, show that there is a minimum h_0 below which the reentrant transitions do not exist. This minimum h_0 depends on both the substrate interaction parameter, A, and the ratio K/L. The low-temperature layering-transitions end in critical points that we label $T_{t,n}$, which always increase to T_{PR} with increasing layer number. Similarly, the reentrant transitions start and end in critical points labeled $T_{t,n+\frac{1}{2}}$ and $T_{c,n+\frac{1}{2}}$, respectively. The $T_{t,n+\frac{1}{2}}$ always decrease toward T_{PR} with increasing n, so that the endpoints of the low-temperature layering-transitions and the starting points of the reentrant transitions approach each other as the coverage increases. Finally, $T_{c,n+\frac{1}{2}}$ always increase toward the roughening temperature.

The mean-field theory suggests that the reentrant layering transitions, associated with the DOF phase, should be quenched close to the substrate. The data show that reentrant layering starts at three layers for both argon and krypton on graphite. A vapor pressure study of argon on boron nitride found that reentrant layering starts at two layers. The difference may be explained as being due to the different substrate potentials (graphite is about 10% stronger). Finally, the experimental data show that $T_{t,n}$ increase in temperature (interestingly, we may include $n = 1$, 2, and 3 in this relation), and that $T_{t,n+\frac{1}{2}}$ basically decrease, as was found in the mean-field results.

In summary, the principal features of the behavior of multilayer argon and krypton films have been reproduced qualitatively, using a simple, mean-field model. The calculation suggests that near the substrate, reentrant layering should be suppressed, and that the magnitude of this effect should depend on the substrate used. The results of the De Olivera and Griffiths model, which successfully explain layering in CH_4, are contained within the present model. For ratios of nearest

to next-nearest-neighbor interactions small enough, the reentrant transitions are suppressed entirely.

Chapter 5

Other Models of Film Behavior

In the last chapter, it was demonstrated that lattice-gas and SOS models may be successful in describing, at least to some extent, the layering transitions by which a multilayer film grows; however, these types of models cannot hope to predict all aspects of film behavior. First of all, the lattice of the lattice-gas models has been taken to be either a square or a triangular lattice where molecules stack directly atop the molecules of the layer below. Neutron-diffraction studies have found that real multilayer films have either an ABC or ABA stacking, or a combination of the two[33]. Also, lattice-gas models cannot describe the melting transitions that are found in monolayer films, and as was shown in Chapter3, the second and third layers of argon and krypton. If these layers do indeed act like a lattice-gas, that is, if the positions of the molecules were strongly constrained to a lattice, then melting transitions and layer triple points would not be expected. If, on the other hand, the molecules were in a very weakly corrugated substrate potential, melting transitions describable by theories of two-dimensional melting would be expected. Most experimental results seem to represent an intermediate regime where the criteria for neither model are strongly met. Finally, the lattice-gas model must break down around the bulk triple point, T_t, because at this temperature, melting must occur in some form.

In this chapter, two additional models of film behavior are presented that

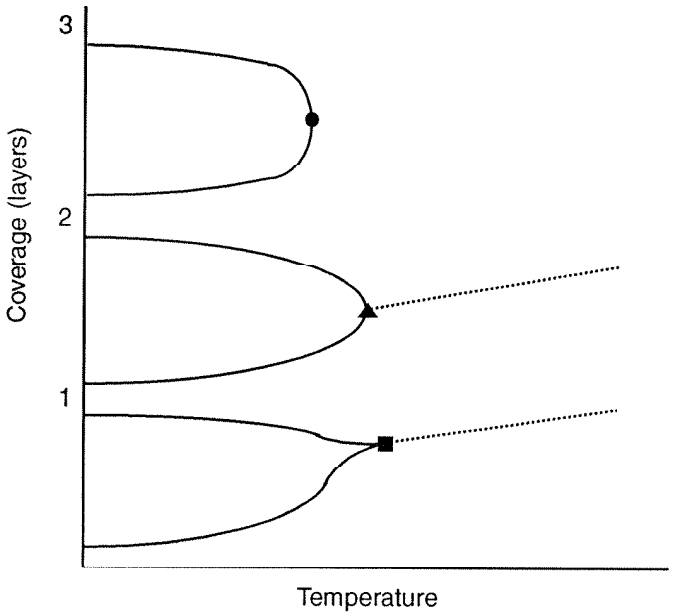

Figure 5.1: Multilayer phase diagram based on the FCC adsorption model.

describe some of the aspects of multilayer film behavior left out of the Ising lattice-gas adsorption model. The first is the "FCC adsorption model" of Saam that may describe a film with either ABC or ABA stacking. The second is the continuum surface-melting model that has been applied in past studies of argon and krypton films[30, 54, 87].

5.1 The FCC Adsorption Model

For krypton on graphite, the monolayer forms as a $\sqrt{3} \times \sqrt{3}$ commensurate phase, so that one out of every three graphite lattice sites is occupied by a krypton atom, and three equivalent solid phases may exist on sublattices A, B, and C. In Saam's[47] model, the graphite lattice is partitioned into "super sites" consisting of triangles of three graphite lattice sites. Because the size of the krypton atoms effectively excludes the occupation of nearest-neighboring sites, each super site has only four possible states, 0 (empty), A, B, or C. The first layer, therefore, should have the phase diagram of a three-state Potts lattice-gas (Fig. 5.1). This phase di-

agram is similar to that of an Ising lattice-gas in that at low temperatures a broad coexistence region exists between the gas phase (0) and one of the solid phases (A, B, or C). The coexistence region does not end in a critical point in this case. The high-temperature/ low-coverage phase consists of an equal proportion of A, B, and C, with some dislocations. As the temperature is lowered, or the coverage increased, one sublattice is chosen at a second-order phase transition. Therefore, the first-order layering-transition must continue as a second-order tricritical[1] line at higher temperatures (dashed line, Fig. 5.1). The point at which the tricritical line meets the first-order transition is termed a multicritical point[2]. The phase diagram for the first layer in Fig. 5.1 is very similar to what has been found in studies of monolayer krypton on graphite.

For the second layer, the situation is similar. However, instead of three degenerate solid phases, there are only two. If the first-layer solid phase is labeled phase A, then the only possibilities for the supersites in the second layer are 0, B, or C. There is still a second-order transition at high temperatures, in this case an Ising critical line[3] (dotted line, Fig. 5.1), associated with the spontaneous symmetry breaking between the two degenerate solid phases. The endpoint of the low-temperature coexistence region in the second layer is a tricritical point. Third and higher layers, on the other hand, are expected to have phase diagrams identical to the Ising lattice-gas because farther-than-nearest-neighbors will break the degeneracy between the sublattices. The film presumably chooses either an ABC or ABA stacking scheme, depending on the farther-than-nearest-neighbor interactions, so that once the solid phases for the first two layers have been chosen, there is only one possibility for the third and higher layers.

[1]The term tricritical is used to denote a transition from a disordered state into one of three degenerate, uniform phases.

[2]A multicritical transition involves the transition into one of four or more degenerate, uniform phases (in this case A, B, C, or 0).

[3]A transition from a disordered phase into one of two equivalent substates is termed an Ising transition.

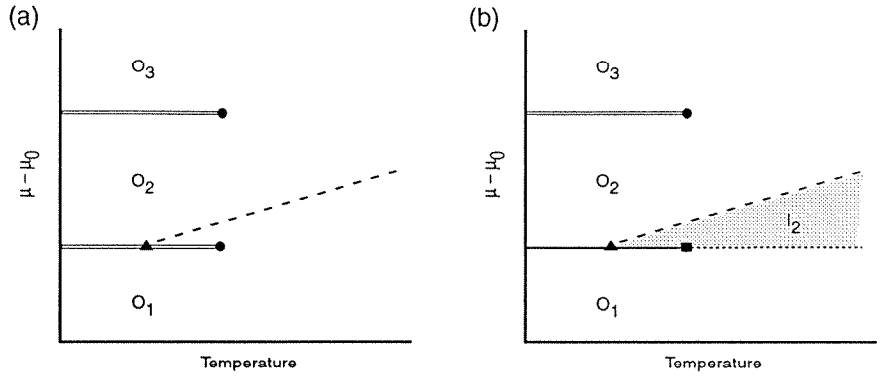

Figure 5.2: Phase diagram for the layers two and three in krypton, based on the (a) the vapor pressure study by Gangwar and Suter[88] and (b) the x-ray study by Hainsey *et al.*[89].

The FCC adsorption model, of course, cannot describe incommensurate phases, such as monolayer argon, nor can it describe the IC transition found in monolayer krypton. However, the model may still apply to the second layer, which is known to form a commensurate phase with respect to the first layer (at most temperatures and pressures), even though the first layer is incommensurate.

A recent vapor-pressure study of krypton films by Gangwar and Suter (GS)[88] found evidence for an order-disorder transition in the second layer but not in the third, in apparent agreement with the FCC adsorption model. The phase diagram suggested by GS is shown in Fig. 5.2(a). The dashed line shows the locations of small anomalies in the compressibility and was assumed to interpolate back to the second layering transition (solid line), so even though a triple point was not observed directly, the data suggest that some sort of triple-point behavior occurs. The phase diagram is slightly different from the one shown for the second layer in Fig. 5.1, because at above the triple (or tricritical) temperature, the layering-transition continues as a first-order transition between disordered phases of different densities. This difference should not change the interpretation, and GS suggest that the dashed line is a second-order transition associated with the broken stacking degeneracy. Both the second and third layering-transitions were

found to end in critical points, although the measured critical-point exponents were found to differ significantly from the expected 2D Ising values.

An x-ray diffraction study, performed in the same temperature-coverage regime by Hainsey, Gangwar, Shinder, and Suter (HGSS)[89], was interpreted to confirm the phase transitions found in the vapor-pressure study while adding an additional order-disorder transition in the second layer. The modified phase diagram is shown in Fig. 5.2(b). The new phase transition suggested by HGSS is shown with a dotted line. In this phase diagram, the second layer no longer ends in a condensation critical point, but in what HGSS label a multicritical point. They use the term generically to designate the point where a first-order transition becomes continuous. The monolayer, bilayer, and trilayer ordered phases are labeled O_1, O_2, and O_3, respectively. HGSS observe that the scattering peak decreases in intensity in going from O_2 to the phase labeled I_2, but then increases again in going from I_2 to O_1, which led to the proposition that I_2 is a bilayer, disordered phase. The new phase transition separates the monolayer ordered phase from the suggested bilayer disordered phase. From the results of the vapor-pressure study, no phase transition was expected here, because the monolayer was expected to be ordered (in most other systems, it is found that the second layer forms on top of an ordered first layer, at least below the bulk-triple-point temperature). If the first layer is ordered in I_2, then the disordered second layer should disappear continuously as the coverage is decreased, leaving the ordered first layer. Instead, HGSS suggest that the disordered second layer induces disorder in the first layer, which then reorders as the coverage is decreased. HGSS term this behavior "reentrant melting." This phenomenon, if it does occur, would be a unique observation in multilayer film studies. If this phenomenon occurs in krypton, then according to our data, it almost certainly occurs in argon, because the heat capacity signals are nearly identical in the two systems. HGSS suggest, in apparent opposition to the conclusions of GS, that both the order-disorder transitions are infinite-order

phase transitions, and so may be manifestations of KTHNY melting. Because the scattering data in the I_2 phase do not fit the expected peak shapes for either a solid or liquid film, HGSS suggest that I_2 may actually represent a hexatic phase, although this suggestion seems far-fetched.

The heat capacity data taken in our study dramatically confirm the existence of a triple point (or critical endpoint), and thus an order-disorder transition between dense phases, in the second-layer phase diagram. The heat capacity peaks associated with second-layer melting, however, are not fully understood. These peaks were the broad, mesalike peaks shown in Fig. 3.12. The corresponding peaks for argon were shown in Fig. 3.11. The mesas have a very abrupt rise or peak at some coverages, followed by a much more gradual falloff at higher temperatures. Plots in the (μ, T) plane of the positions of the peaks and the approximate positions of the falloffs suggest that the mesalike behavior does not represent the existence of a broad, solid-liquid coexistence region, which should occur along a line (the melting line) in μ versus T (figs. 3.29 and 3.30). Instead, the mesas map out a region (the region marked 2F in figs. 3.22 and 3.30) that agrees quite well with HGSS's I_2 region in the temperature range treated in that study. From the heat capacity data, it is not clear whether a real phase transition occurs going from I_2 to O_1. The heat capacity mesa may, indeed, be due to the passage through a bilayer-disordered phase, ending in an infinite-order phase transition that should be unobservable in the heat capacity. An alternative explanation may be that the observed falloff of the mesa is an effect of losing the second film layer to desorption as the temperature is increased. In that case, it is possible that the first layer is ordered in I_2.

Although the heat capacity data cannot confirm or disprove the reentrant melting hypothesis, it is relevant to understanding the high-coverage, order-disorder transition of Fig. 5.2(b). As this phase boundary is crossed, the heat capacity shows a sharp discontinuity in slope, in disagreement with its interpretation as

an infinite-order phase transition. The data suggest instead that the phase transition is either first order, at non-constant spreading pressure, or second order. The interpretation of the phase transition as being due to the broken stacking degeneracy of Saam's FCC model[47], would imply that the transition is second order with specific heat exponent $\alpha = 0$. The heat capacity data may be viewed as being consistent with this type of logarithmic (lambda-like) divergence. On the other hand, a first-order phase transition may suggest that the mechanism is 2D grain-boundary-induced melting[18, 19], expected to occur on a smooth substrate.

It is not clear, even in the case of a registered uppermost layer, which model should apply theoretically. If the atoms of the uppermost layer were strongly confined to the positions of a lattice, one should expect the system to be described in terms of the lattice model. If the corrugation potential were very weak, one might expect to describe the system in terms of a continuous system in a weak ordering field. For intermediate cases, as are probably found in most experiments on adsorption systems, a crossover might be expected from one type of behavior to the other. Not enough simulational work has been done, however, to try to predict into which category most systems should fall.

On the other hand, the second-layer data in both gases show a small peak that was interpreted as a commensurate-incommensurate transition. This phase transition has not yet been detected in scattering studies. If the interpretation is correct, then the second layer melts from an incommensurate phase at most coverages, and it is the continuous model that should be applied.

The heat capacity data contradicts the phase diagrams for the third layer presented by GS and HGSS. Instead of simply a layering-transition ending in an Ising critical point, as would be consistent with the FCC adsorption model, the heat capacity data show an order-disorder transition between dense phases similar to what is found in the second layer. In the argon data, a triple point between solid, liquid, and gas phases is observed. Above the triple-point temperature, the

μ versus T data (Fig. 3.9) are inconclusive as to the order of the phase transition. In the third layer of krypton, the data suggest a quite different picture. No triple point exists, (Fig. 3.18) as is evidenced by only a single peak for scans that pass along the third layering-transition. The layering-transition does not end at a critical point, but continues to higher temperature as an order-disorder transition between dense phases (a melting transition). In this case, the μ versus T data suggest that the melting transition is first order, because the μ trajectories follow the melting line for a short interval. The phase diagram for the third layer of krypton is reminiscent of the incipient triple-point scenario used by Chan and coworkers[29] to explain the monolayer N_2 phase diagram. In this picture, the substrate stabilizes the solid phase to above the liquid-gas critical temperature, so that only two phases, solid and fluid, may exist.

Clearly, the FCC adsorption model fails to predict the behavior of the third and higher layers in argon and krypton. This is hardly surprising, since lattice models employing only nearest-neighbor interactions have not been able to reproduce the reentrant layering behavior found in the fourth layer and higher. The FCC adsorption model does present an attractive explanation for the order-disorder transition found in the second layer, but the data do not prove that the broken stacking degeneracy is the mechanism responsible for the transition, and the observation of a possible CI transition calls into question the applicability of a lattice model to second layer melting. An alternative explanation is that the second layer acts like a continuous two dimensional system and that melting occurs by the (first-order) grain-boundary melting mechanism[18, 19].

5.2 Surface Melting and Substrate-Induced Freezing

As was mentioned in Chapter 1, surface melting is a phenomenon thought to occur when a crystal surface disorders below the bulk-triple-point temperature, T_t. The same phenomenon may also occur at the surface of a thick film, where it is sometimes given the designation "stratified melting." For several years it was widely believed that surface melting does occur in argon, neon, and krypton films, based on the studies of Zhu and Dash[54, 30] and Pengra, Zhu, and Dash[87]. This evidence has recently been overturned by the neutron study of Gay *et al.*[33] and by the heat capacity study of Lysek[46]; Lysek *et al.*[90], where it was shown that the melting peaks believed to be due to surface melting of the uniform film were actually due to the melting of capillary condensate. With the realization that it is possible to form films of about only six layers on grafoam, it seems that these types of adsorbed films are much less ideal systems for studying surface melting than was previously expected. Nevertheless, computer simulations and neutron-diffraction studies continue to suggest, although less stongly, that surface melting may occur in argon on grafoam. Much better evidence for surface melting has been found in scattering studies of metal surfaces [91, 92, 93, 94, 95, 96] (and references in [97]). Finally, because a related phenomenon, substrate-induced freezing, does occur in argon and krypton on graphite, it is appropriate here to examine the data taken so far in this laboratory for evidence of surface melting and to compare our data with other studies that have treated the subject.

Surface melting and substrate-induced freezing are very easy to justify in terms of a continuum model[98, 99]. Suppose that a thin layer of thickness L_l near the surface is converted to liquid at below T_t, as illustrated in Fig. 5.3(a). Neglecting surface terms, the free energy is always unfavorable to the conversion, because the chemical potential of the liquid phase is higher. The change in the free energy per

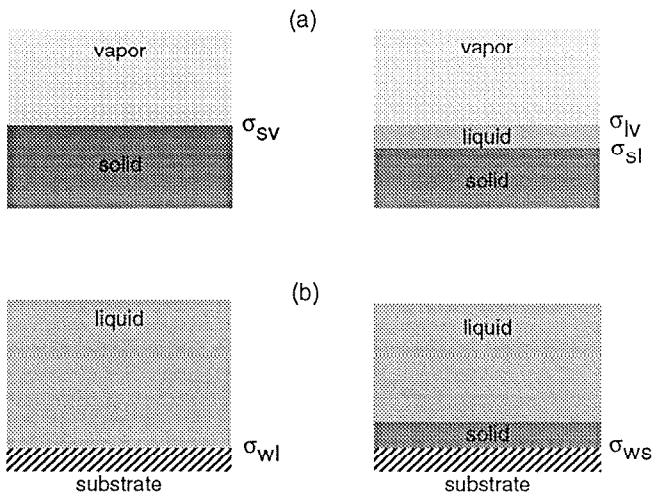

Figure 5.3: Possible states of films in the continuum model: (a) illustrates surface melting, (b) describes substrate-induced freezing.

unit area that is due to the bulk terms is

$$\delta\mathcal{F}_{bulk} = (\mu_l - \mu_s)L_l \ , \tag{5.1}$$

where μ_l and μ_s are the chemical potentials of the liquid and solid at the same temperature. However, as the solid-vapor interface is replaced by a solid-liquid-vapor sequence, the interfacial terms in the free energy also change by

$$\delta\mathcal{F}_{surface} = \tilde{\sigma}_{sl} + \tilde{\sigma}_{lv} - \sigma_{sv} \equiv \delta \ ,$$

where σ is the surface tension, and the subscripts s, l, v, stand for solid, liquid, and vapor. The tildes are added to the solid-liquid and liquid-vapor surface tensions to suggest that these interfaces may interact with each other, so that we have $\tilde{\sigma}_{sl} \rightarrow \sigma_{sl}$ and $\tilde{\sigma}_{lv} \rightarrow \sigma_{lv}$ in the limit $L_l \rightarrow \infty$. The parameter δ describes the propensity of the material to surface melt. For $\delta < 0$, there will be some temperature below T_t at which the system will be able to lower its free energy by forming a liquid layer.

Substrate-induce freezing, or surface freezing, may be described in exactly the same way. In this case, the situation is that of a semi-infinite region of material

System	layers solid at T_t
CH_4/gr	1 or 2
Ar/gr	3
Kr/gr	3
CF_4/gr	≥ 4

Table 5.1: Surface freezing in all systems studied

in contact with a solid substrate (Fig. 5.3(b)). If the parameter

$$\delta' = \tilde{\sigma}_{ws} + \tilde{\sigma}_{sl} - \sigma_{wl} \ , \tag{5.2}$$

where w denotes the wall, is negative, then a slab of solid material will form next to the substrate at a temperature above T_t. Both parameters, δ and δ' must be known to predict the region where a stratified film, a film composed of a solid layer beneath a liquid layer, is thermodynamically favorable. If δ is negative, the transition from uniform to stratified film occurs below T_t. Similarly, the sign of δ' determines whether the transition from stratified to uniform liquid film occurs above or below T_t. It is also possible for the stratified phase to be suppressed completely, depending on the relative magnitudes of the parameters, but clearly this is not the case for the systems that have been studied.

The data taken in this study clearly show a stratified film existing above T_t, indicating that δ' is negative for all the systems studied if the model is applicable. Table 5.1 gives the number of layers known to remain solid above T_t for the thickest films attainable. The results suggest the relation, $\delta'_{CH_4} < \delta'_{Ar} \sim \delta'_{Kr} < \delta'_{CF_4}$. It may seem strange at first that δ'_{CF_4} is so much larger than δ'_{CH_4}, but because δ' is a small difference in large numbers, the relative difference between the parameters in the two systems is understandable.

The data show no evidence of the existence of a liquid layer below T_t in either system except for approximately one fluid layer associated with the melting of the uppermost layer of the film. In argon, krypton, and CF_4, it might be expected that if stratified melting occurs below the bulk triple point, it would involve only layers

above the third or fourth, since the solid phase of these layers seems to be strongly stabilized by the substrate. It should be noted that according to the continuum model[100], if surface melting does not occur in the bulk, but substrate-induced freezing does occur, then a dewetting transition should exist at the triple point, and a uniform solid film of finite thickness should be able to exist above T_t. It seems unlikely that these phenomena occur in argon, krypton, or methane, but the data do not rule them out.

Another model has been proposed for substrate-induced freezing[101] that also treats the film as bulk material and calculates the hydrostatic pressure that the film exerts on itself because of the substrate field. The height of the solid film underneath the liquid film is determined by the place where the pressure becomes equal to the bulk melting pressure. This model, of course, predicts that the transition between stratified and uniform liquid film always occurs above the triple point. The pressure model seems to underestimate the magnitude of substrate-induced freezing in argon on graphite[102]. We cannot compare the data to the surface-tension model, as the relevant surface tensions are unknown.

The phenomenon of surface melting is distinct form substrate-induced freezing, which involves the solid-substrate and liquid-substrate surface tensions, but both can give rise to layer-by-layer melting. We believe that conclusions cannot be drawn about surface melting using adsorbed films of less that five layers, since the layer-by-layer melting behavior observed is obviously due to substrate-induced freezing, as is evidenced by the first three layers' melting above the triple point.

Two recent neutron-diffraction studies have addressed the question of surface melting in argon on graphite. The first, by Larese and Zhang[32], found that disordering occurs in a film two or more layers thick at temperatures below the melting temperature of the first layer. The authors conclude that melting proceeds from those portions of the film farthest from the substrate inward. Since the first layer in a two-layer film melts well above the bulk triple point, we believe that

the layer-by-layer melting observed is due to substrate freezing. That is, within the continuum model, the result determines only the sign of δ'. Larese and Zhang also note that layers are observed to melt over a range of temperatures as great as 10 kelvins. We find that the uppermost layer of a film up to three layers thick acts as an independent, two-dimensional system adsorbed on the solid lower layers. Melting at above the layer triple-point temperature may be first order, so the system can pass through a coexistence region where the uppermost layer is partially liquid and partially solid. Because this gradual disordering is limited to the uppermost layer, we believe that it is not evidence of surface melting.

The other neutron diffraction paper by Gay *et al.* studied the surface melting of *Ar* in graphite foam by integrating the intensity of a peak corresponding to the 2D 11 and 3D 220 peaks to measure the total amount of solid adsorbed in the experimental cell. The amount of liquid, in statistical layers, was deduced by subtracting from the total number in the cell. Measurements were made at 80.5K for different total amounts adsorbed, finding that for coverages between 5.0 and 10.8 statistical layers, an average or 1.5 layers were liquid. For total coverages of 13.8 and 22.9 layers, the amount in the liquid phase was 2.5 and 5.7 layers. According to our findings, layer triple points (at least for the second and third layers) occur below 70K, so around one layer of liquid can be accounted for in the uppermost film layer. Since the film thickness increases by only about one layer between 12 and 20 equivalent layers adsorbed, the increase in liquid thickness in this region must be due to melting of the capillary condensate. However our thermodynamic measurements show that the capillary condensate does not start melting until about 82K on the adsorption branch. It is conceivable that the lattice structure of the condensate may be sufficiently distorted that the amount of solid is undercounted in the neutron measurements. Indeed, we find that the condensate melts over a range of temperatures instead of with a delta function peak as is expected for a solid. This behavior may be due to the effect of the

capillary walls on the condensed solid. In conclusion, we do not find convincing evidence of surface melting in argon on graphite, or in the other systems studied, from this or from previous studies, although more detailed studies of thicker films may well be able to uncover information about this phenomenon.

Chapter 6

Conclusions

Until quite recently, a simple and appealing picture seemed to have emerged, showing how thin films of simple substances like argon may evolve into bulk matter. However, evidence has recently begun to emerge, calling this picture into question. In this and in companion studies, using calorimetry much more sensitive than was previously available, combined with simultaneous vapor-pressure measurements, and armed with a better understanding of how to take capillary condensation into account, we have confirmed that the truth is considerably more complex and more interesting than was previously suspected.

According to the previous view, the first layer has a rich, two-dimensional phase diagram including gas, liquid, and solid phases. In some substances, e.g., methane, the solid phase could be commensurate with the substrate, or incommensurate at lower density or higher density, depending on temperature and coverage. In argon, on the other hand, no commensurate phase had been detected at all. Thicker films could be understood in terms of a simple lattice-gas model, the completed first layer forming the underlying lattice. Each layer would undergo an Ising-like critical point, $T_{c,n}$, that terminates a first-order layering transition. As the layer number N increases to infinity, $T_{c,n}$ would tend to the roughening transition of the bulk interface, T_R. At somewhat higher temperatures, but still somewhat below T_t, a separate phenomenon, called surface melting in the bulk, or

stratified melting in the film, would occur. Surface melting could be understood to be a consequence of the fact that if the liquid phase wetted the solid-vapor interface, the system could lower its free energy at $T < T_t$ by interspersing a film of liquid between the solid and the vapor. Bulk melting at T_t could then be understood as the propagation of the liquid-solid interface, into the bulk. It was also noticed that the reverse phenomenon could occur: If the solid phase wetted the liquid-substrate interface, a solid film at the interface would be expected at $T > T_t$. This phenomenon was termed substrate-induced freezing.

If surface melting occurs in argon, we find no evidence for it in our measurements. We do find that observations previously taken to be evidence of surface melting may instead be understood as being due to the two-dimensional melting of the uppermost layer, or to the melting of capillary condensate.

Our results confirm the earlier observation by Zhu and Dash[30, 31], that a film of solid does in fact persist at the substrate interface for $T > T_t$. Indeed, the first three layers are each seen to melt at temperatures above T_t, that increase with increasing thickness of overlayers adsorbed on top of them. However, our data indicate that the first layer probably forms a commensurate phase just before it melts, and the second layer appears to form an incommensurate (with respect to the first layer) film just before it melts. The same behavior is found in the second layer of krypton. We have found that the second and third layers of argon adsorbed on graphite and the second layer of krypton each have a complex, two-dimensional phase diagram much like the first layer. The solid first layer forms an inert substrate for the second layer, and the second does likewise for the third.

Between three and four layers in both systems, there is a broad, two-phase melting region between 70 and 80K that seems to be a precursor of an entirely new kind of behavior in the fourth and higher layers called reentrant layering. These new layering transitions, between films of fractional coverages, are evidence for a recently proposed phase transition called preroughening. Further evidence

	T_R	T_{PR}	T_R/T_t	T_{PR}/Tt
Methane	80	none	0.88	-
Argon	80	69	0.96	0.83
Krypton	110	96	0.95	0.83
CF_4	none	none	-	-

Table 6.1: Roughening and preroughening temperatures for all systems studied.

for preroughening comes from the observation of heat capacity peaks between the two different layering regimes that converge in temperature as the coverage is increased and as bulk interfacial behavior is approached. The data taken in this study suggest that at least for argon and krypton, the critical endpoints of the low-temperature layering transitions tend not to roughening, but to preroughening, $T_{c,\infty} = T_{PR}$. The endpoints of the reentrant layering transitions should tend to T_R in argon and krypton. The older picture may, however, continue to be valid in methane, which does not appear to have a PR transition, and CF_4, which has neither roughening or preroughening transitions (see Appendix B). These results are summarized in Table 6.

By considering the onset of the reentrant layering transitions in argon and krypton on graphite and the locations of the heat capacity peaks associated with preroughening, we may conclude that these systems begin to show behavior characteristic of bulk interfaces at around three and a half layers adsorbed. The onset of this sort of behavior seems to be dependent on the substrate used. Since methane and CF_4 behave in a manner qualitatively different from argon and krypton, it is clear that there is more than one kind of approach to bulk behavior. Whether there are yet other kinds remains to be determined for future observations. These measurements also fail to shed very much light on the melting of thick films, since the signal is overwhelmed by melting of the capillary condensate in the relevant temperature range. We hope that future observations will provide new insights into this problem.

Appendix A

Melting of Capillary-Condensed Solid

Many studies have reported finding heat capacity peaks in adsorbed matter near the temperature of the triple point. In the past, these peaks have always been attributed to the melting of the film, although recent reinterpretations of some studies have suggested that these peaks are actually due to the melting of capillary condensed matter[33]. The triple-point peaks for argon and krypton taken during this study are shown in Figs. A.1 and A.2. The same sort of peaks shown in Fig. A.1 were observed by Zhu and Dash (ZD) in argon and neon[30, 31] and attributed to the surface melting of the uniform film. According to this theory, melting should initiate at a thin layer at the surface, and the solid-liquid interface should move completely through the film as the triple-point temperature, T_t, is approached. The theory predicts that near T_t, the heat capacity should rise as $(T_t - T)^{-4/3}$, and this behavior was confirmed by fits to the experimental data. Because ZD did not realize that capillary condensation occurred in the system, they greatly overestimated the film thickness, and the surface-melting picture seemed likely.

For krypton, the peaks observed in the study by Pengra, Zhu, and Dash (PZD)[87] are qualitatively different from those shown in Fig. A.2. PZD found a

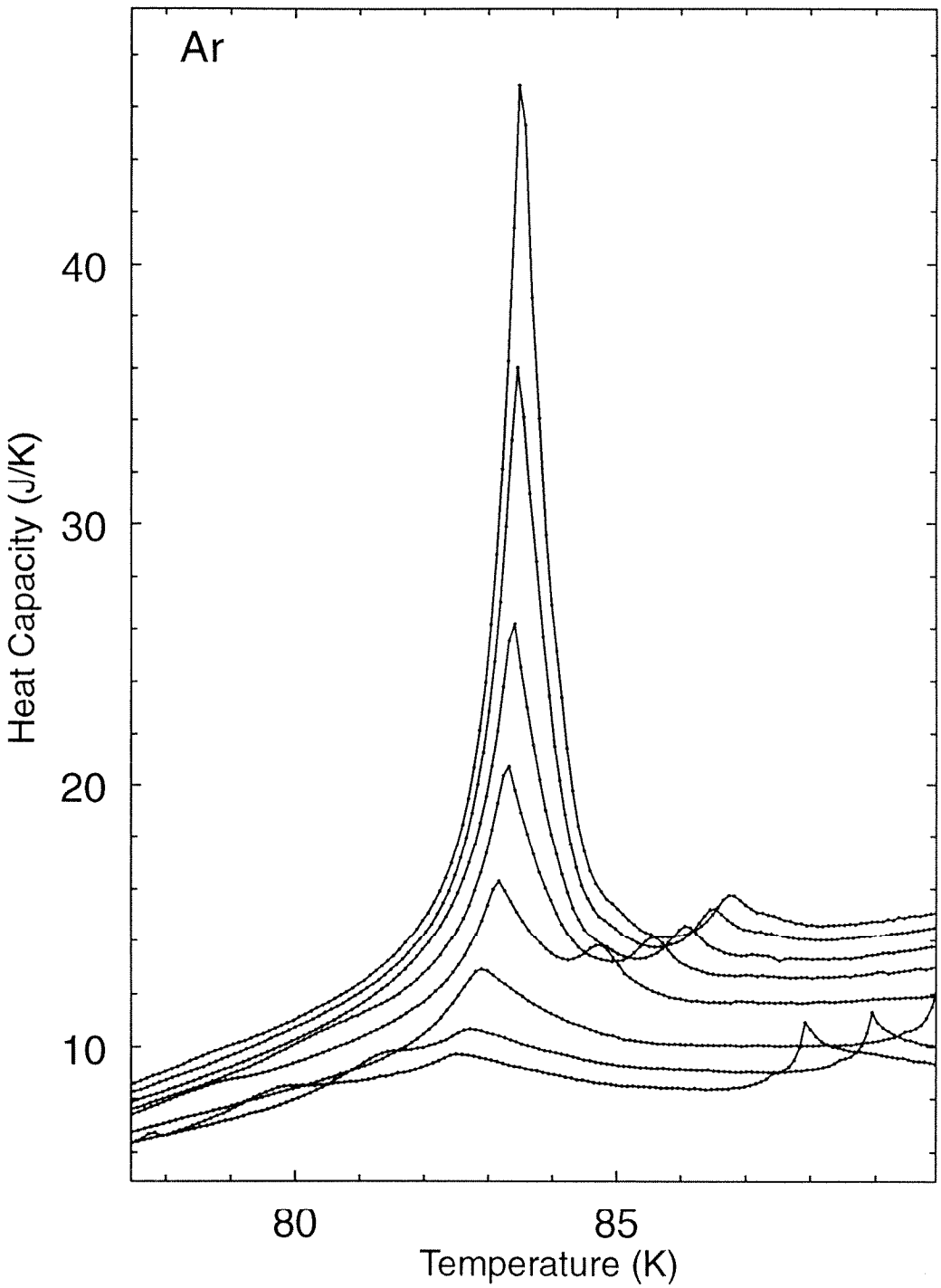

Figure A.1: Capillary-condensate melting peaks for argon. Coverages, at the peak, are 3.74, 3.99, 4.68, 5.28, 5.98, 6.64, 7.61, and 8.60 equivalent layers. The peak at the far left is second-layer melting. The peaks crossing the condensate melting peaks are third-layer melting.

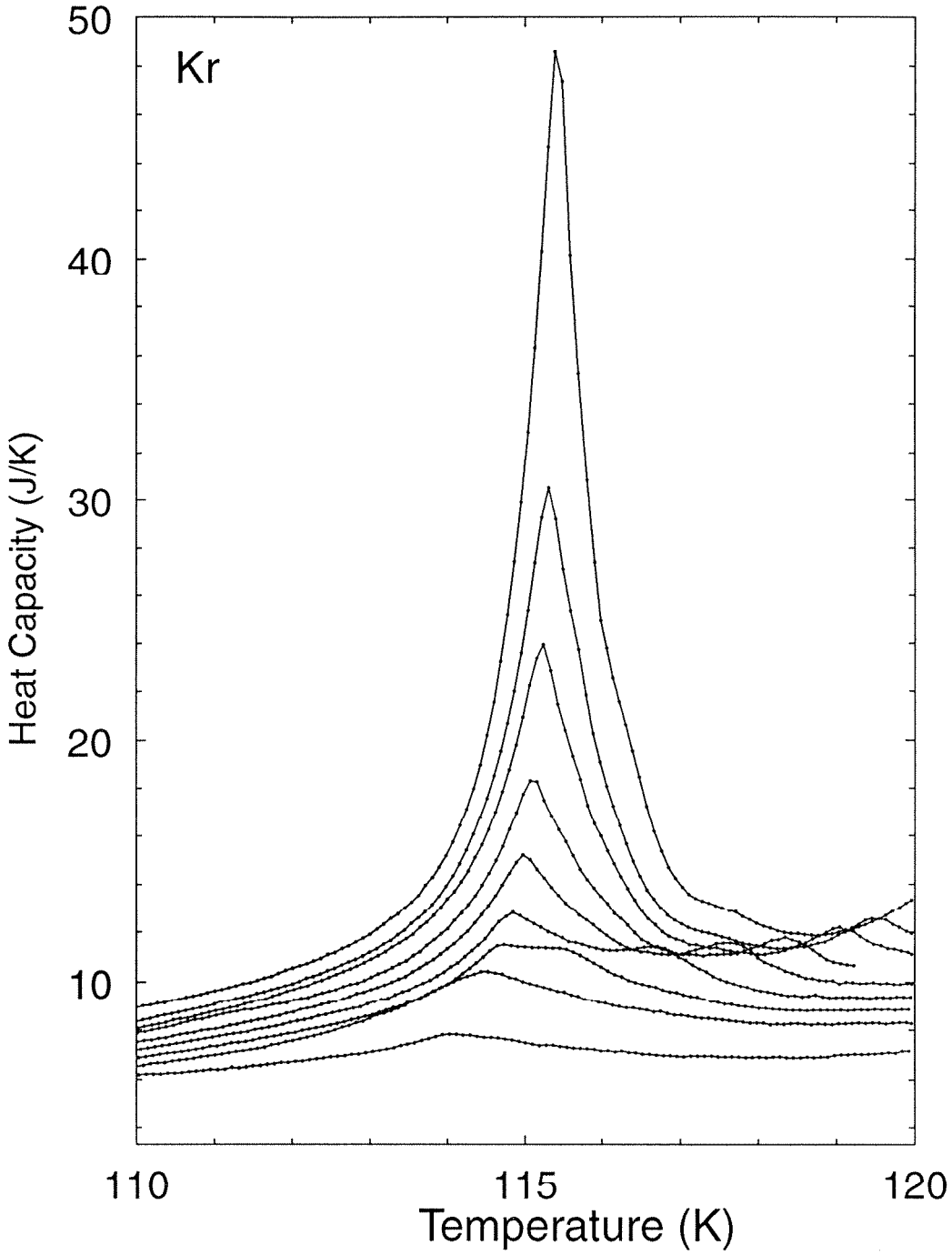

Figure A.2: Capillary-condensate melting peaks for krypton. Coverages, at the peak, are 2.69, 3.23, 3.53, 3.87, 4.24, 4.64, 5.20, 5.78, and 7.08 equivalent layers. The small peak at the right is third-layer melting.

series of peaks that were spread out over a much larger temperature interval, and in which lower-coverage peaks were no longer enveloped by the peaks at higher coverage. This behavior was attributed to surface melting in a strained film. PZD surmised that thin films were strained by the substrate, causing the melting transition to occur at much lower temperatures. As the film thickness increased, the film would relax toward the bulk lattice constant, and the melting transition would occur closer to T_t. The discrepancy between the data shown in Fig. A.2 and the data of PZD can be explained by the results of the methane study. The melting peaks from systems on the adsorption branch of the hysteresis curve resemble the data of Figs. A.1 and A.2 in that peaks from lower-coverage scans are enveloped by the peaks from higher-coverage scans, and they occur over a relatively narrow range of temperatures. On the other hand, peaks from systems on the desorption branch are much more spread out in temperature, and are not enveloped by higher-coverage peaks. It is probable, therefore, that the peaks reported by PZD were taken along the desorption branch. The method of preparing the films was not reported in the paper.

Capillary condensate has little to do with multilayer films, but it is an important system in its own right. The question of the melting of capillary-condensed matter has been treated in the past, but theories were not compared with accurate experimental results until Lysek's methane study. Based on the results of that study, a new parameterless theory was developed that predicts the melting curve of capillary-condensed matter[64]. The results of the argon and krypton studies allow us to compare the different theories qualitatively in three different substances. A review of the different theories pertaining to the melting of capillary condensate is given here, and the data are used to suggest which of them is correct.

The chemical potential of the capillary condensate will be reduced with respect

to the bulk-saturated chemical potential by

$$\mu - \mu_i^0 = v_i \frac{\sigma_i}{D_i}, \tag{A.1}$$

where v_i and σ_i are the molar volume and surface tension of the capillary condensed phase, either solid or liquid, and D_i is the radius of curvature as in Eqn. 3.1. Equation A.1, known as the Kelvin equation, is usually derived by integrating Eqn. 3.1 from bulk coexistence at constant temperature using the differential relation $d\mu_i = v_i dp$. Another completely independent derivation of Eqn. A.1 is given in Ref. [64].

Three different models use Eqn. A.1 to predict different melting behavior. The first is due to Defay and Prigogine[103]. According to their classic textbook, melting may occur when solid and liquid are able to coexist in a pore. Equating the chemical potentials of solid and liquid condensates, and using Eqn. A.1 yields for the melting temperature T_m,

$$\frac{T_t - T_m}{T_m} = \frac{1}{L}\left(\frac{v_l \sigma_l}{D_l} - \frac{v_s \sigma_s}{D_s}\right), \tag{A.2}$$

where L is the latent heat of fusion. To derive this equation, the Clausius Clapeyron relation was used in the form

$$\mu_l^0 - \mu_s^0 = \frac{L}{T_m}(T_t - T_m), \tag{A.3}$$

where, if melting occurs at $T_m < T_t$, $\mu_l^0(T_m)$ is the extrapotation of μ_l^0 to temperatures below T_t. Equation A.3 assumes that the radius of curvature may change as the condensate melts. According this equation, melting may occur over some region of the $\mu - T$ plane, provided that pores are not all uniform.

A refinement was made of Bachelor and Forster (BF) in their measurement of the solid surface tension of dioxane. BF make the assumption that $D_l = D_s \equiv D$, which was also suggested, somewhat disapprovingly, by Defay and Prigogene[103]. Using BF's assumption in Eqn. A.3 and eliminating D, using Eqn. A.1, we have

$$\frac{T_t - T_m}{T_m} = \frac{\mu_s^0 - \mu}{L}\left[\frac{v_l \sigma_l}{v_s \sigma_s} - 1\right]. \tag{A.4}$$

This equation predicts a unique melting curve in the T–μ plane for any adsorbate. If Eqn. A.4 is correct, the slope of the melting line would yield a measurement of $\frac{v_l \sigma_l}{v_s \sigma_s}$. BF used their measurement of this quantity to calculate σ_s. Solid surface tensions have proven to be very difficult to measure by other means.

Based on the data reported in this appendix, and also on the data from Lysek's methane study, Lysek, LaMadrid, Day, and Goodstein (LLDG)[64] presented an alternative model for the melting of capillary condensate. This model makes a different restriction than the one proposed by BF. The conditions imposed at melting are that solid and liquid condensate have the same chemical potential, temperature, *and pressure.* Pressure equality, $p_l = p_s$, means

$$\frac{\sigma_l}{D_l} = \frac{\sigma_s}{D_s}, \tag{A.5}$$

according to Eqn. 3.1. Using Eqns. A.3 and A.5, the new criterion for melting is

$$\frac{T_t - T_m}{T_m} = \frac{v_l - v_s}{v_s L}(\mu_i^0 - \mu). \tag{A.6}$$

This equation also predicts that melting will occur along a substrate-independent straight line in the μ–T plane, intercepting the bulk triple point. This model, unlike the previous one, has no unknown parameters. The slope of the melting line is determined solely by the molar volumes and the latent heat. The surface tensions do not enter the equation.

We wish to compare the three models, represented by Eqns. A.3, A.4 and A.6. Equations A.4 and A.6 predict that melting will occur along a single line in the μ–T plane. On the other hand, Eqn. A.3 predicts that melting will occur in some region of that plane. As was shown in Figs. A.1 and A.2, the melting peaks are broad and have widths of two to three degrees. Ideally, a first-order phase transition, such as melting, should be observed either as a delta-function heat capacity peak, if the transition occurs at constant pressure, or a mesalike peak, if it occurs at constant volume. In the case of the constant-volume transition, the

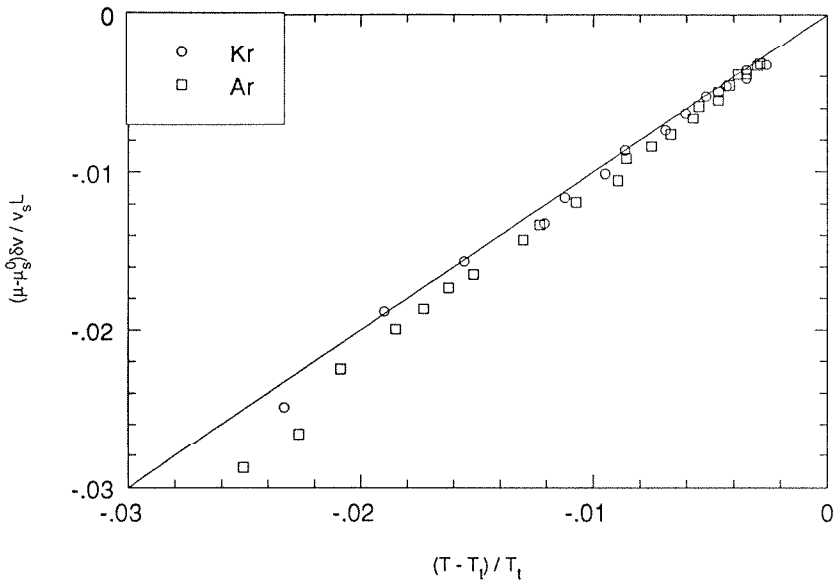

Figure A.3: Positions of capillary condensate melting peaks plotted in (μ, T). For both argon and krypton the points fall close to a straight line.

μ data should be observed to follow the melting line while material is converted from solid to liquid. An analysis of the μ data (not shown) reveals that this is not the case. The fact that deltalike functions are not observed, however, is not necessarily evidence for the the Defay and Prigogene model (Eqn. A.3). There are other reasons that we may expect the melting transition in this particular system to be smeared out. For example, finite-size effects are expected to round out a first-order phase transition when the characteristic dimension of the system is small. Surface melting of the condensate may cause melting to initiate below T_m, and substrate-induced freezing may cause it to extend above T_m.

To test the prediction of Eqns. A.4 and A.6, Fig. A.3 shows plots of the melting peak positions, defined to be the point where the heat capacity feature reaches its maximum value, on a graph of $(\mu - \mu_s^0)(v_l - v_s)/v_s L$ versus $(T - T_t)/T_t$. Both equations predict that the data points will fall on a single, striaght line extrapolating throught the point (0,0). Equation A.6 predicts in addition that the line will

have a slope equal to one. The result is in excellent agreement with both predictions. Similar plots of the methane data give equally good results. These results suggest that the melting lines predicted by Eqns. A.4 and A.6 should instead be identified with the line in μ–T on which melting occurs most rapidly.

To make a further quantitative test of the models we rewrite Eqns. A.3, A.4, and A.6 in the following way:

$$\frac{T_t - T_m}{T_m} = \frac{\mu_s^0 - \mu}{L}, \left(\frac{v_l}{v_s}x - 1\right) \tag{A.7}$$

where

$$x = \frac{\sigma_l/D_l}{\sigma_s/D_s}. \tag{A.8}$$

Then the three models may be summarized as follows: the model of Defay and Prigogine, Eqn. A.3, leads us to expect that melting will occur for an unpredicted range of values of x, which would generally be expected to be different for each substance and each substrate. The model of Batchelor and Foster, Eqn. A.4, gives $x = \sigma_l/\sigma_s$, so that we would expect a single distinct value of x for all the data from each adsorbate. The values of σ_s are unknown, but generally speaking it is expected that

$$\frac{\sigma_l}{\sigma_s} \approx \left(\frac{v_s}{v_l}\right)^n, \tag{A.9}$$

i.e., that the ratio will scale as the ratio of densities to some power, perhaps $n = 2/3$. If so, one would expect to find a value of x in the range 0.9 to 0.95 for each of the three substances, CH_4, Ar, and Kr. Finally, the third model makes the simple prediction $x = 1$ for all three substances.

Figure A.4 shows plots of x versus T for the argon and krypton peaks. The error bars are pricipally due to the uncertainties in T and μ, which become comparable to $T_t - T$ and $\mu_s^0 - \mu$ near the triple point. Figure A.5 shows similar data for the adsorption and desorption branch peaks in methane. All the results are consistent with $x = 1$, although it is not possible to rule out systematic deviations

from $x = 1$ of the order of 1 to 2% for a particular substance. However, it does seem fair to say that all the data are consistent with the conclusion

$$x = 1.00 \pm .02 \,. \tag{A.10}$$

We conclude that all of the heat capacity peaks are accounted for with $x \approx 1$. The simplest explanation of this result is that the LLDG model is correct: Capillary-condensed material melts when liquid and solid may coexist in the same pore, at the same temperature, chemical potential, and pressure. Conversely, if the BF model is correct, then methane, argon, and krypton all have solid surface tensions very nearly equal to the liquid surface tension at their respective triple-point temperatures.

Notice that either of these two models account nicely for the difference between the adsorption and desorption branch behavior found in the methane study and also in the krypton work[1]. In either model, the temperature at which melting occurs is governed by the chemical potential. On the adsorption branch, capillary condensation does not begin to occur until μ is close to μ_s^0, so melting is confined to a narrow range of temperatures. On the desorption branch, however, capillary condensation persists as matter is removed, until much larger values of $\mu_s^0 - \mu$, so that melting occurs over a wider range of temperatures.

It should be stressed that all the arguments that have been given concern the thermodynamic melting temperature of matter, unaffected by small size effects. Other studies have observed that melting may be suppressed to below T_t for matter confined to very small pores, or formed into very small clusters[104, 105, 106, 107] (and references in [107]). That is not the kind of behavior discussed here. Using the known value of σ_l and $\mu_s^o - \mu$ for our data, we find that all the peak temperatures we observe correspond to capillary condensation in pores of diameter

[1]We believe that the melting peaks observed by Pengra *et al.* in Ref. [87] were taken along the desorption branch. The data reported in this work were taken along the adsorption branch.

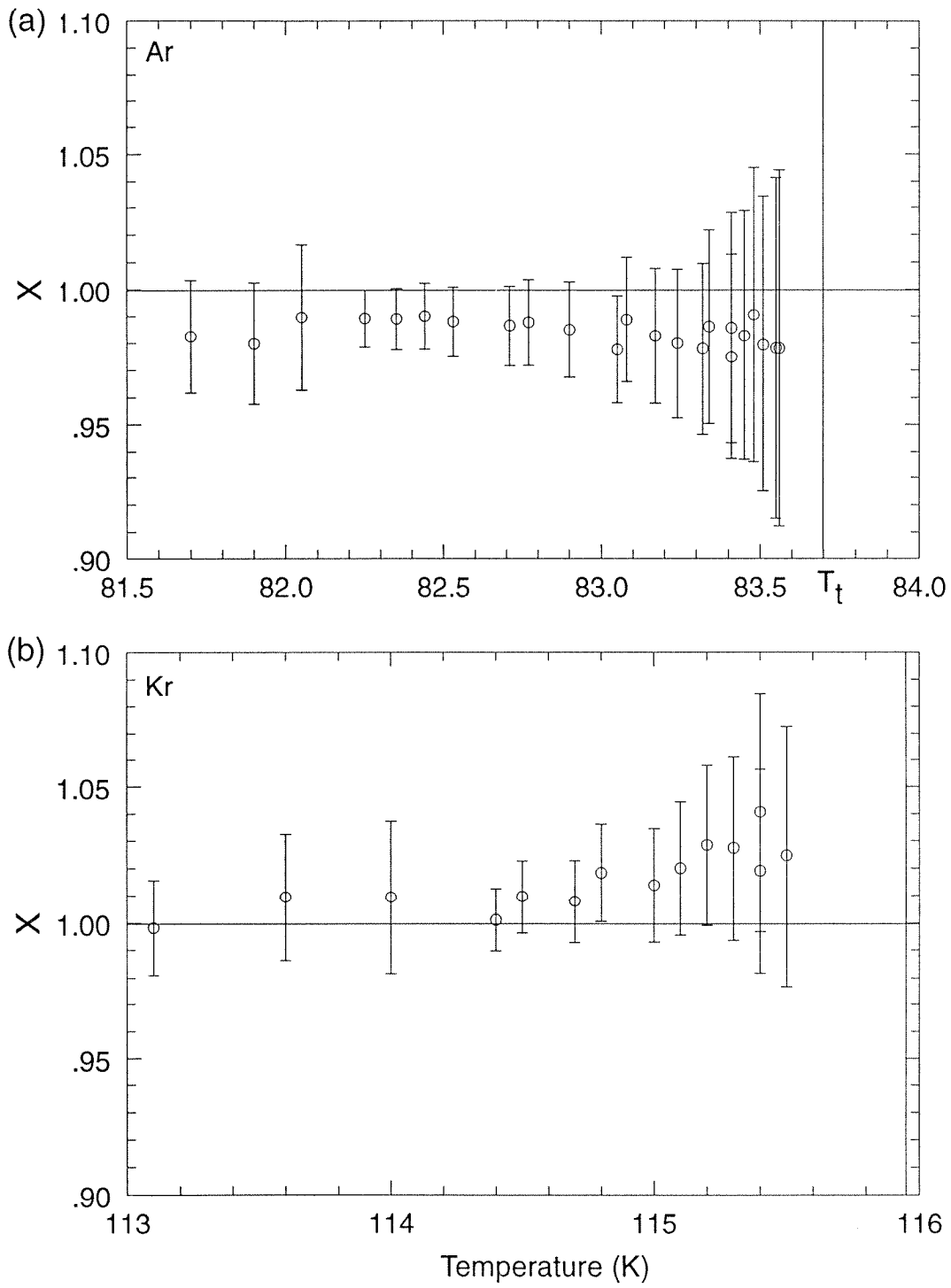

Figure A.4: The quantity x plotted versus temperature for argon and krypton.

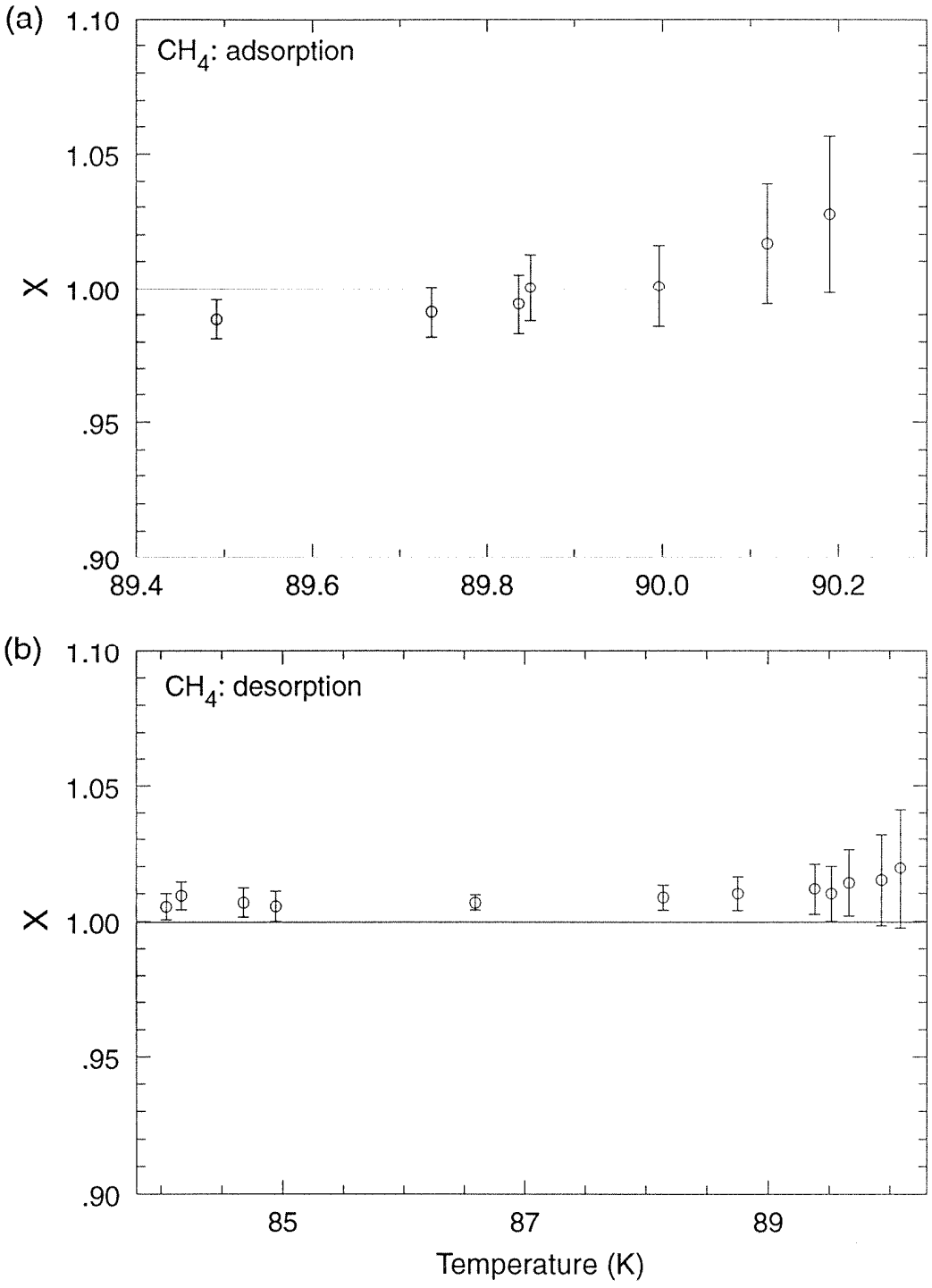

Figure A.5: The quantity x plotted versus temperature for CH_4 adsorption and desorption runs.

100-400$\mathring{A}$. Generally speaking, finite-size effects are observed to suppress melting only for dimensions less than 100$\mathring{A}$.

The most important prediction of the LLDG model, that $T_m(\mu)$ will be given by Eqn. A.6 with $x = 1$, not only for different condensates, but also for different substrates, has not been tested by these data. Measurements using other substrates are clearly needed.

Appendix B

And now for something completely different

Various aspects of the CF_4 work have been briefly mentioned in Chapters 1 through 4 of this thesis. This work is being presented in an appendix because it does not fit in very well with the argon and krypton work, and because we are not able to identify the various heat capacity features with as much confidence as we were in the other systems. Also, CF_4 films have been better studied than argon and krypton films, and our contribution over and above the other investigations is limited. There are many mysteries in both the monolayer and multilayer phase diagrams of CF_4/graphite. Presented in this appendix are the highest resolution heat capacity data yet taken in this system, at higher than 70K. These data will be of use to anyone studying this system in the future.

An important difference between CF_4 and Ar, Kr, and CH_4 is that CF_4 is an example of an incompletely wetting film, as was established in the ellipsometry study of Nham, Dhir, and Hess (NDH) [108]. An example of a phase diagram for an incompletely wetting film is shown in Fig. B.1(a). In the example shown, a wetting transition exists, so that at temperatures above T_W, the film wets the substrate, but below T_W, the film thickness is finite at the bulk-saturated vapor pressure. At low temperatures, a series of individual "layer condensation" tran-

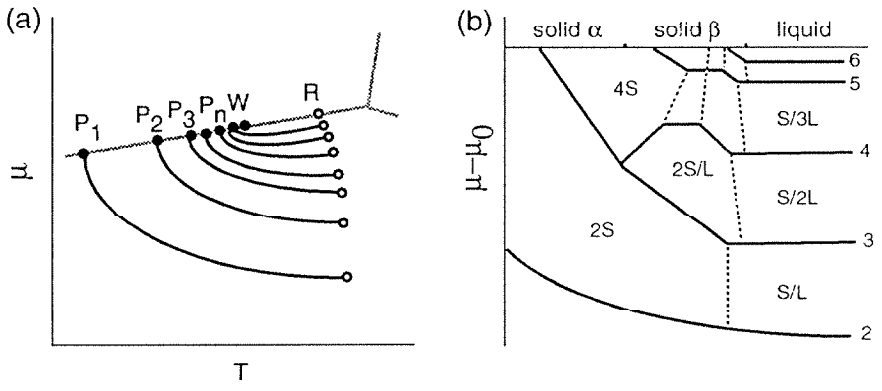

Figure B.1: (a) Phase diagram, in (μ, T) for a generic incompletely wetting film. P_n are individual layer-condensation transitions; W is wetting, and R is roughening. (b) The multilayer phase diagram proposed by NDH for CF_4/graphite.

sitions, P_n, may exist at the bulk coexistence boundary. The temperatures at which these phase transitions occur, T_{P_n}, approach T_W in the limit $n \to \infty$. It is believed, on the basis of vibrating fiber experiments [44, 109], that in a number of systems T_W equals T_t, the bulk triple point. This behavior is termed triple-point wetting. NDH report that CF_4 is limited to two layers on graphite below 71K, and that at 71K a double layer condensation (third and fourth layer) transition occurs. At 80K the fifth layer condenses, at 87K the sixth, and evidence was found for at least eight layers above T_t. NDH also report that the double layering transition splits into two separate layering-transitions at a triple point (between two-, three-, and four-layer films) at 75K. The phase diagram suggested by their study is shown in Fig. B.1(b). The dashed lines shown are melting transitions, not observed directly, but implied by the bends in layering-transitions. In our heat capacity study, we have found that a maximum of four layers of CF_4 form on grafoam, significantly less than NDH found for single-crystal graphite. Because of this limit, we are unable to investigate the possibility of triple-point wetting. We do find evidence for the layer-condensation transition at around 75K observed by NDH. Also, we find that the third- and fourth-layer triple points exist above T_t, a few degrees above where NDH suggest. This is the first time layering triple

points for layers beyond the first have been found above the bulk triple-point temperature.

Another difference between CF_4 and the other systems studied is that CF_4 undergoes an orientational order-disorder transition in the temperature range we are studying. Below $T_{\alpha\beta}$ =76.2K, the fluorine atoms of the CF_4 molecules are oriented relative to one another in the crystal. This phase is termed the α solid. Above $T_{\alpha\beta}$ the molecules are orientationally disordered in what is called the β solid phase. The latent heat associated with this solid-solid transition is approximately twice the latent heat of melting[110]. CH_4 also has an orientational transition, but at much lower temperatures ($\sim$ 11K). At higher temperatures, the CH_4 molecule acts as though it were spherical. The fact that CF_4 has an orientational transition at higher temperatures allows for the possibility of numerous solid phases in the film with different orientations. Indeed, a monolayer phase diagram with five different monolayer solid phases was presented, based on the results of an ac heat capacity study by Zhang, Feng, Kim, and Chan (ZFKC)[50]. The identification of the various phases was made by comparison with the x-ray data of Kjaer *et al.*[111]. The phase diagram is shown in Fig. B.2. The five solid phases are HI (high-density incommensurate), 2 $\times$ 2 (the registered phase), I(S) (an incommensurate phase believed to be anisotropic), 3P (an unknown phase; 3P is for "three peaks" after the x-ray-diffraction profile), and IP (an intermediate phase proposed solely on the basis of the heat capacity data). ZFKC found that the melting of the 2 $\times$ 2 and I(C) phases is strongly first order. In contrast, two heat capacity peaks were identified with the melting of the HI phase, a small sharp peak and a broad, rounded peak at slightly higher temperature. The small peak was labeled "weakly first order" and the broad peak was called continuous. ZFKC suggest that the HI solid melts by a two-step KTHNY process, in which case the first peak would be a transition to an orientationally ordered fluid, and the second a transition to an isotropic fluid.

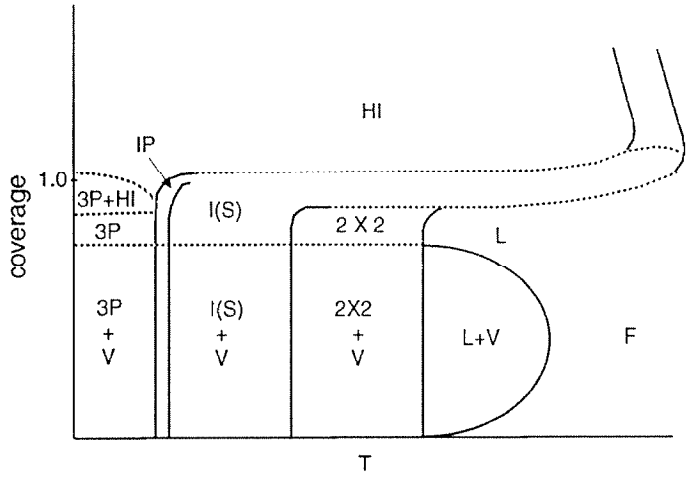

Figure B.2: The phase diagram proposed by Zheng *et al.* for monolayer and extended monolayer CF_4.

According to Fig. B.2, the CI transition from I(S) to 2 × 2 joins the 2 × 2 melting at around 81K at what should be a triple point (or critical endpoint, if the CI transition is continuous). However, ZFKC do not present evidence that this sort of phenomenon occurs. We have found heat capacity evidence for a (second) triple point at 85K, suggesting that the IC transition meets the melting transition at that temperature.

A final important difference between CF_4 and the other systems is that in CF_4 the bulk saturated vapor pressure is extremely low around the triple point temperature, where interesting phenomena occur in the film. Because we had no way of measuring such low pressures accurately at the time these data were being collected, it is impossible to compute the chemical potential of the film accurately enough to use for analyzing the data. An advantage of the small vapor pressure is that the contribution of desorption to the measured heat capacity is nearly absent.

B.1 Monolayer and Extended Monolayer Triple points

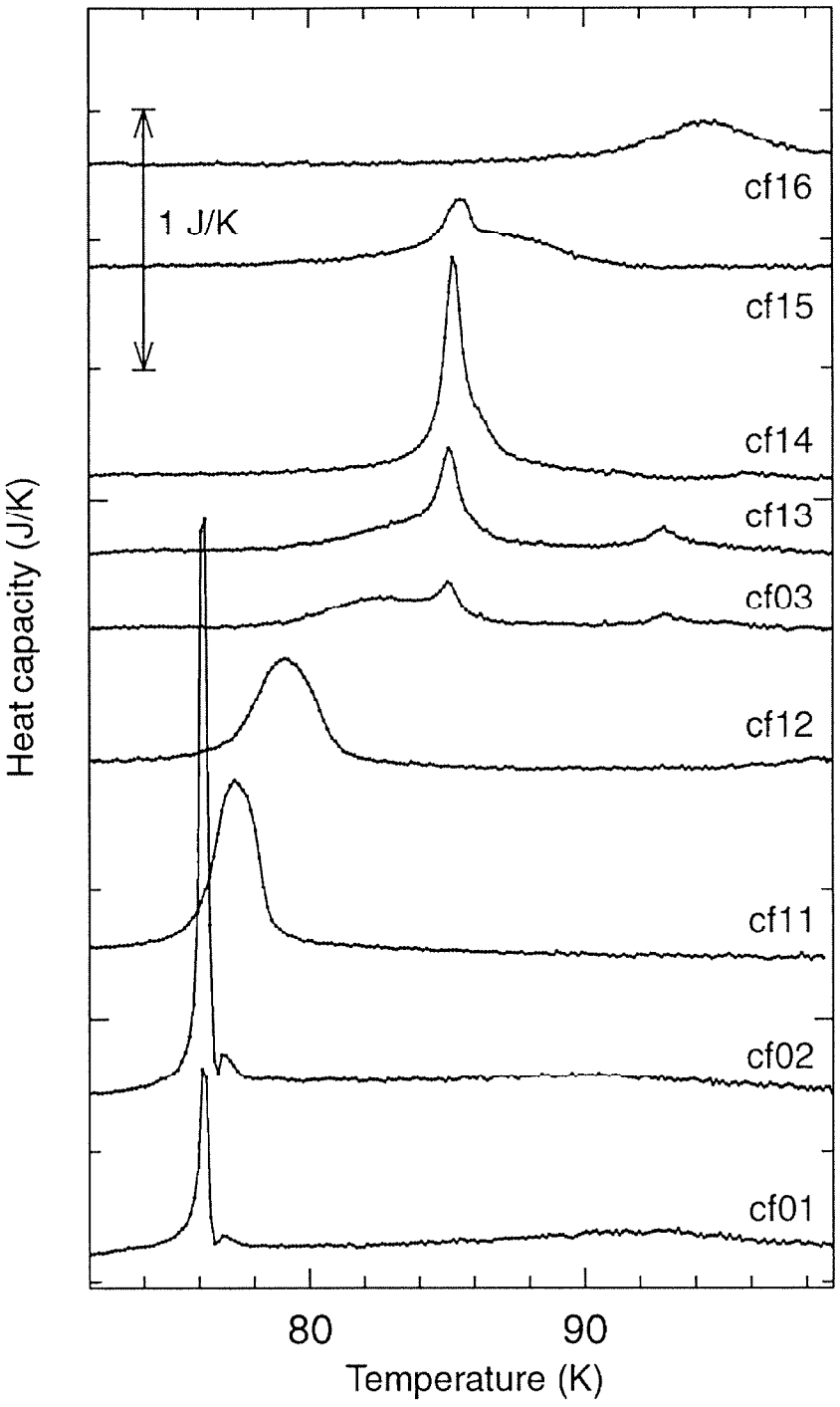

Figure B.3: Heat capacity scans in the monolayer and extended monolayer. Coverages, at low temperature, are 42.47, 83.68, 112.56, 117.27, 119.66, 121.90, 126.24, 130.04, 134.25 stpccs.

Figure B.3 shows heat capacity peaks that are due to melting in the monolayer and extended monolayer region. Scans cf01 and cf02 show the strongly first-order, triple-point melting of the 2 × 2 phase at T_t^{2D}, also found by ZFKC. At a coverage of about 0.8 layers (scan cf11), slightly past the maximum coverage of monolayer solid-gas coexistence, the melting transition moves to higher temperatures, as is found in most other systems. The melting peaks at above the triple-point temperature are rounded instead of δ-functionlike. ZFKC found flat-topped (mesalike) peaks in this region. In either case, the breadth of the peak is likely to be due to passage through a narrow, solid-liquid coexistence region. The latent heat of the transition in scans cf11 and cf12, as calculated from the area under the peak, is approximately the same as that for scan cf02. Instead of continuing smoothly to high temperature as the coverage is increased, the melting line appears to trace out a step at 85K. ZFKC do not report any peaks in this region, but we find four peaks occurring at the same temperature for different coverages (scans cf03, cf13-15). This situation has always been taken as evidence for a triple point. The simplest modification of Fig.B.2 that allows for a triple point at $T_t^X = 85$K is that the IC transition (I(S) to 2 × 2) joins the 2 × 2 melting line at this temperature. Two possible phase diagrams are shown in Figs. B.4(a) and (b). In case (a), the CI transition is first order, so that there is a change in density between the incommensurate and the registered phases. In case (b), the CI transition is continuous. In either case, the triple-point peaks represent the transition from 2 × 2 + L (islands of registered solid, locked onto the corrugation of the substrate, in a disordered fluid) to I(S) + L (floating solid in a disordered fluid). In case (a), some of the triple-point peaks may also be due to the transition between 2 × 2 + IC and IC + L (the melting of the 2 × 2 phase), as shown in the figure. The difference between the two cases is that in (a), there is a change in density across the transition. It seems unlikely that merely the unlocking of islands of 2 × 2 solid from registry would give rise to as large a heat capacity signal as is found

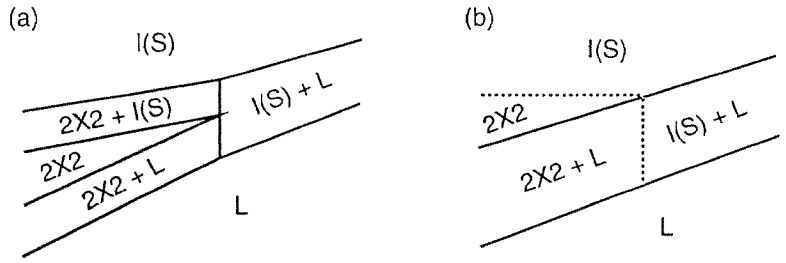

Figure B.4: (N,T) plots of two possibilities for the triple point phenomenon in the extended monolayer of CF_4.

in scan cf14, for example. That sort of transition is found in monolayer Ar and CH_4, where very small, but sharp, heat capacity peaks were observed. It is more likely that phase diagram (a) is correct, and that the CI transition is first order. To our knowledge, this is the first direct observation of a triple point between two solid phases and one fluid phase. At higher coverages (cf16), the melting line again turns to higher temperature, and melting from the I(S) phase also appears as a broad, rounded peak.

B.2 Melting from the HI phase

One of the most interesting possibilities raised by ZFKC is that a KTHNY melting transition occurs from the HI phase. One of our main reasons for studying CF_4 was to examine this phase transition more closely. Figure B.5 shows several scans taken in the HI-monolayer to bilayer region. The double-peak structure, first observed by ZFKC, is found in scans cf18,04-07. These peaks, unlike melting peaks in the extended monolayer of any other system, move to lower temperature with increasing coverage. At the same time, the area under the peaks decreases. In cf07 the two peaks are barely noticeable, and in cf19, the next higher-coverage scan, the two peaks have disappeared entirely. ZFKC also observed that HI melting disappears as the second layer is completed. They suggest two possibilities for the fate of this phase transition: Either it ends on the second layering-transition,

perhaps at the critical point, or it continues to higher coverage without a heat capacity signal. The peaks at 89.0K in scans cf05-07,19 are due to triple-point melting in the second layer. The two peaks preceding, at approximately 80.5K and 85.0K in scans cf06, 07, and 19, are unidentified phase transitions (UFTs). These are most likely first order UFTs occurring at triple points along the second layering-transition. Scan cf08 represents a density above second layer coexistence, where the UFTs and melting have moved to higher temperature.

The hypothesis that the double-peak structure is due HI melting comes from ZFKC's assumption, illustrated in their phase diagram, that the HI/I(S) transition basically runs parallel to the temperature axis after the monolayer is completed. In our view, there is nothing in either study to disprove an alternative hypothesis, that the small peak is due to the HI/I(S) transition, and the broad rounded peak to the continuation of the I(S) melting transition. Indeed, in Ar and CH_4 we found registry transitions that closely followed the first-layer melting transition, as the melting line continued toward higher coverages. Also, the broad peak, identified by ZFKC as the second part of HI melting, is very similar in size and shape to the peak identified with I(S) melting. We must conclude that the data do not choose between the two possibilities. What does seem clear is that both peaks disappear abruptly around the second layer critical point. We know that scan cf07 comes closest to the second layer critical point, because the broad peak following the second layer melting peak extends to higher temperature than in either cf19 or cf06. Cf07 also marks the abrupt disappearance of the double peak. It seems most likely, therefore, that the monolayer melting transition ends on the second layer critical point. The physical interpretation is that once the second layer reaches a sufficient density, the first and second layer become coupled and melt together at the "second layer" triple point, similarly to what was suggested by HGSS for krypton, as was described in Chapter 5. This situation is in contrast to what was found in Ar and CH_4, where the first layer remains solid to very high

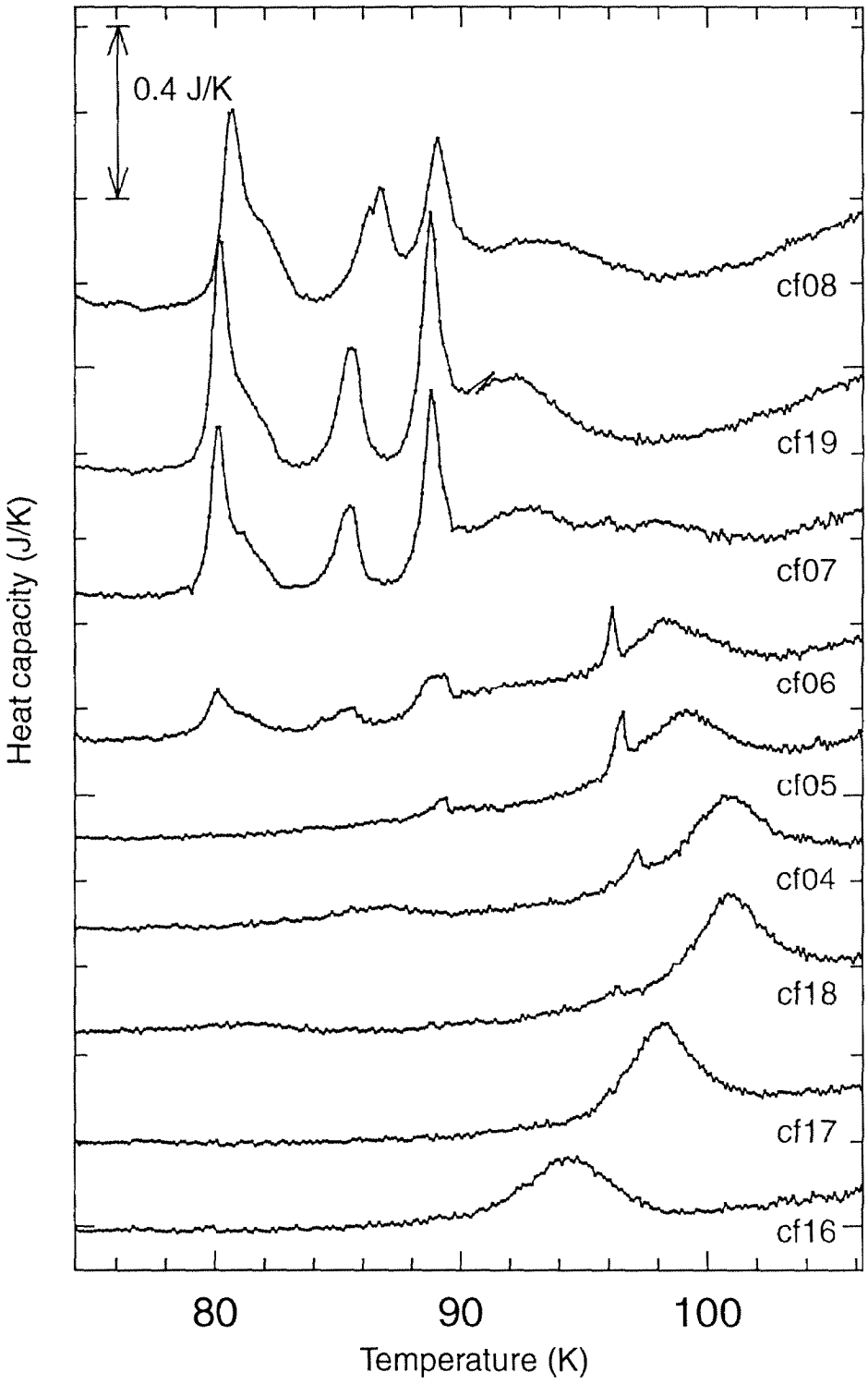

Figure B.5: Heat capacity scans showing the double peak, interpreted as HI melting, and phase transitions in the second layer. Coverages, at low temperatures, are 134.25, 137.85, 147.36, 154.64, 177.27, 208.58, 247.16, 298.52, and 272.29.

temperatures and the second layer acts independently.

B.3 Orientational transition and layering

The large peaks at low temperature in Fig. B.6 are due to the orientational transition occurring in the capillary condensate, and possibly in the film, for relatively low-coverage scans. As was found in a thermodynamic study of bulk CF_4[110], the peak is characterized by a gradual rise and an abrupt falloff at higher temperature. In the data taken in this study, we observe that the peak temperature increases slightly as the coverage is increased. Unfortunately, the absence of good pressure data makes it impossible to analyze the capillary-condensate α-β line in detail; but even without the pressure data, an important difference is apparent between these peaks and the capillary-condensate melting peaks in Ar, Kr, and CF_4. For melting, the maxima of the peaks occur below the triple-point temperature T_t for all scans. However, the temperatures of the $\alpha\beta$ peaks continue to rise above $T_{\alpha\beta}$. For melting, it was found that the width of the peaks caused them to extend above T_t, but the maxima always occurred below that temperature. Therefore, the same equations that were successful in describing the melting transition of capillary condensate cannot possibly describe the $\alpha\beta$ transition, if the transition temperature is identified with the peak maximum. $T_{\alpha\beta}$ was reported by Ref. [110] to be 76.2K. ZFKC made an independent measurement of bulk CF_4 and found $T_{\alpha\beta}$ = 76.5K. ZFKC report that the first-layer triple point occurs at 76.2K, whereas we find 76.1K, so we may use ZFKC's value to adjust our temperature scale. Accordingly, we use $T_{\alpha\beta}$ = 76.4K. The $\alpha\beta$ transition peaks for the highest-coverage scans taken in this study have maxima at 77.6K, more than one full degree above $T_{\alpha\beta}$. ZFKC report that a side peak occurs on the high-temperature side of the $\alpha\beta$ peak at high coverages. They claim that the side peak is due to the interaction of the capillary condensate with the substrate. We do not observe a side peak on the

high-temperature side of the $\alpha\beta$ peak, but it seems clear that the presence of the substrate stabilizes the α phase of the condensate, and possibly the orientationally ordered phase of the film, above $T_{\alpha\beta}$.

At higher coverage (Fig. B.7), a peak seems to emerge from the low-temperature side of the $\alpha\beta$ peak, and move to lower temperature with increasing coverage. ZFKC also noticed a peak in this region that appeared as a side peak on the low-temperature side of the $\alpha\beta$ peak. They observed that the side peak remained at a constant temperature in all heat capacity scans except for their very highest-coverage scan. ZFKC identified this side peak, on the basis of a lengthy series of arguments, as being due to the bilayer-trilayer transition known to exist in that temperature range. ZFKC remarked that they did not understand why the side peak in the highest-coverage scan occurred at lower temperature. With our new knowledge of the role that capillary condensation plays in this system, we can easily answer their question. ZFKC assumed that below the layering-peak temperature, the system was on the bulk coexistence boundary. That is, they believed that the bulk phase in equilibrium with the incompletely wetting film was saturated bulk crystalites. We now know that the bulk phase is unsaturated capillary condensate, so the system's pressure is always below the saturated vapor pressure, $P_0(T)$. As the coverage is increased, the capillaries fill, and the pressure approaches $P_0(T)$. The layering peaks should decrease in temperature, as we observe, because the layering-transition slopes backward in the (μ, T) plane (see Fig. B.1). The layering-transition we observe is in the temperature range where NDH report the double layering-transition. It is not clear whether the peaks shown in Fig. B.7 correspond to the transition between two- and four-layer films or between two- and three-layer films, although the highest-coverage scan (cf37) shows two peaks (at 73K and 76K), in addition to the $\alpha\beta$ peak, which may indicate that the proposed bilayer-trilayer-quadralayer triple point has been crossed.

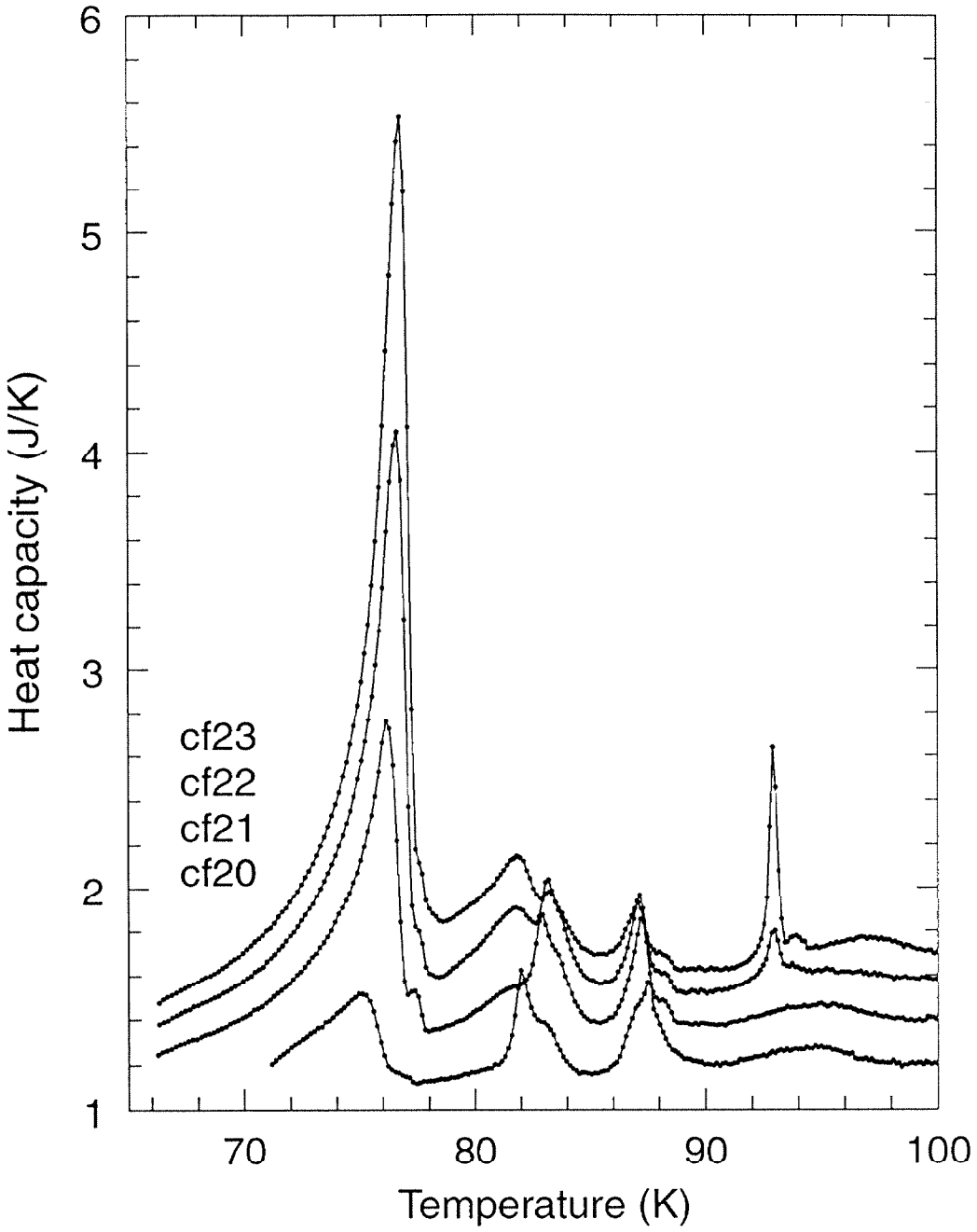

Figure B.6: Four heat capacity scans showing, at low temperature, the peaks that are due to the orientational transition. The peaks at 93.1K in the two highest-coverage scans are third-layer melting. Coverages, at low temperature, are 343.59, 399.97, 447.45, and 489.69 stpccs.

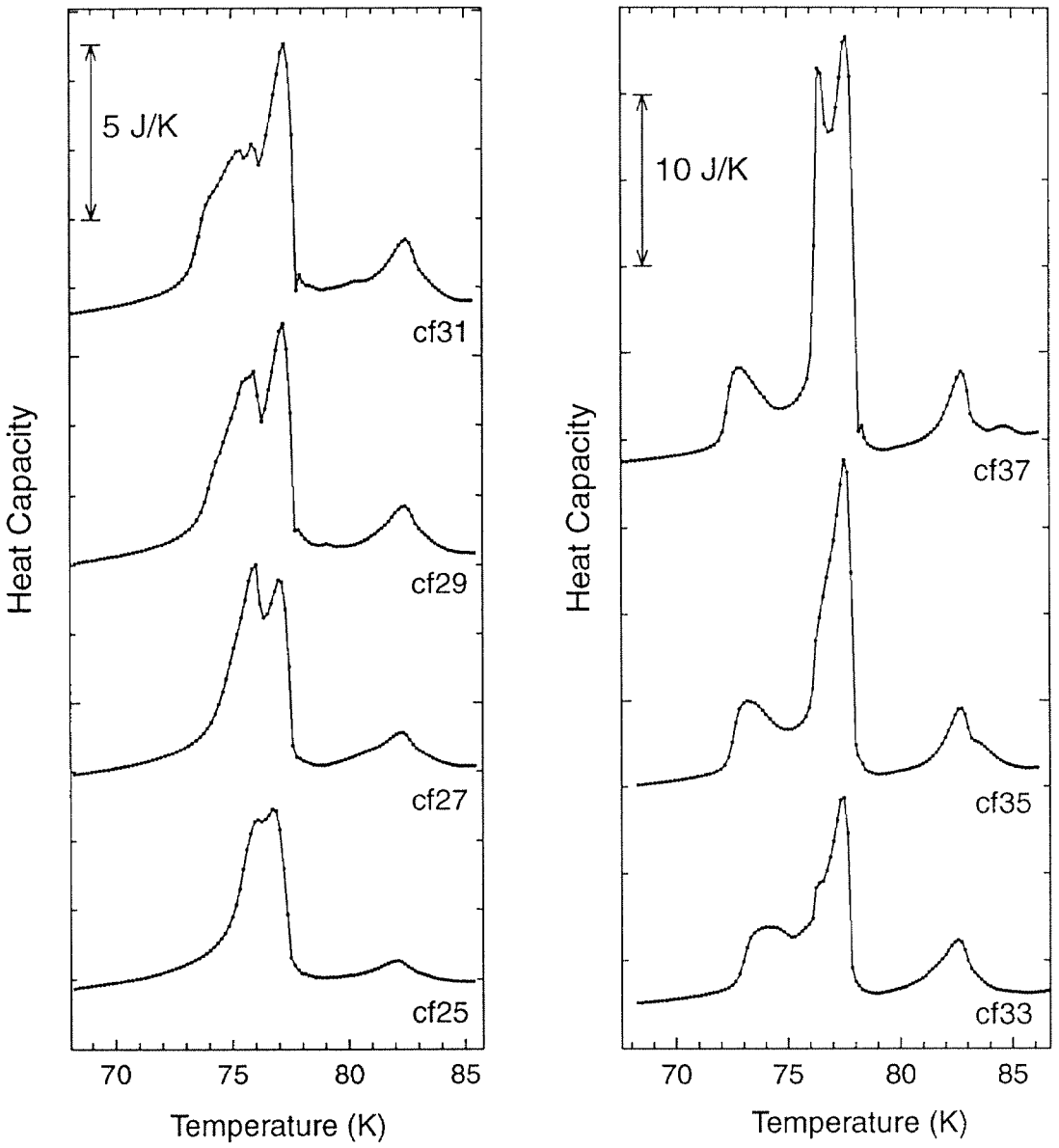

Figure B.7: Peaks that are due to the orientational transition (around 76-77K), and at lower temperature, the possible layering-transition. Coverages, at low temperature, are 560.10, 624.70, 676.32, 734.16, 905.23, 1100.13, and 1368.19 stpccs. The peak at 83K is a UTP.

B.4 Melting in the third and fourth layer

The melting of the third and fourth layers in CF_4 has not been observed previously. NDH suggest melting transitions, shown with dashed lines in Fig. B.1(b), located slightly below T_t. They label, somewhat mysteriously, the phases on either side of the third-layer melting transition (the dashed line above the third layering-transition) as 2S/L and S/2L, suggesting that a three-layer film always has a liquid uppermost layer and the "third layer" melting transition is actually the melting of the second layer underneath the liquid third layer.

The peaks we identify with the melting of the third layer are shown in Figs. B.6 (scans cf22 and 23) and B.8 (scans cf25, 27, 30, 33, 34, and 36). These peaks are very surprising because they are the sharpest peaks we have ever found associated with the third layer in our work, or in any other heat capacity study with which we are familiar. We suggest strongly that these peaks are associated with the melting of the third layer, and not of the second, because the observed growth of the peak between scans cf22 and 23 is consistent with the formation of the third layer. If the peak were second-layer melting, it should have the same area in these two scans, because the second layer is complete at these coverages. Also, the peak in cf23 is sharper than the corresponding peaks for second-layer melting, shown in scans cf07 and 19 of Fig. B.5. It is also rather surprising that the temperature we identify with the third-layer triple point, 93.1K, is almost four degrees above the second-layer triple-point temperature and the bulk triple-point temperature. We found in the argon and krypton studies that the completed, solid third layer may be stabilized by the substrate to temperatures above T_t, when it is covered with a sufficient number of the higher layers. The results for CF_4 suggest that an incomplete, solid third layer may be stable above T_t.

The remaining mystery in our proposed phase diagram is the fate of the second-layer melting transition. The integrated area under the third-layer melting peak

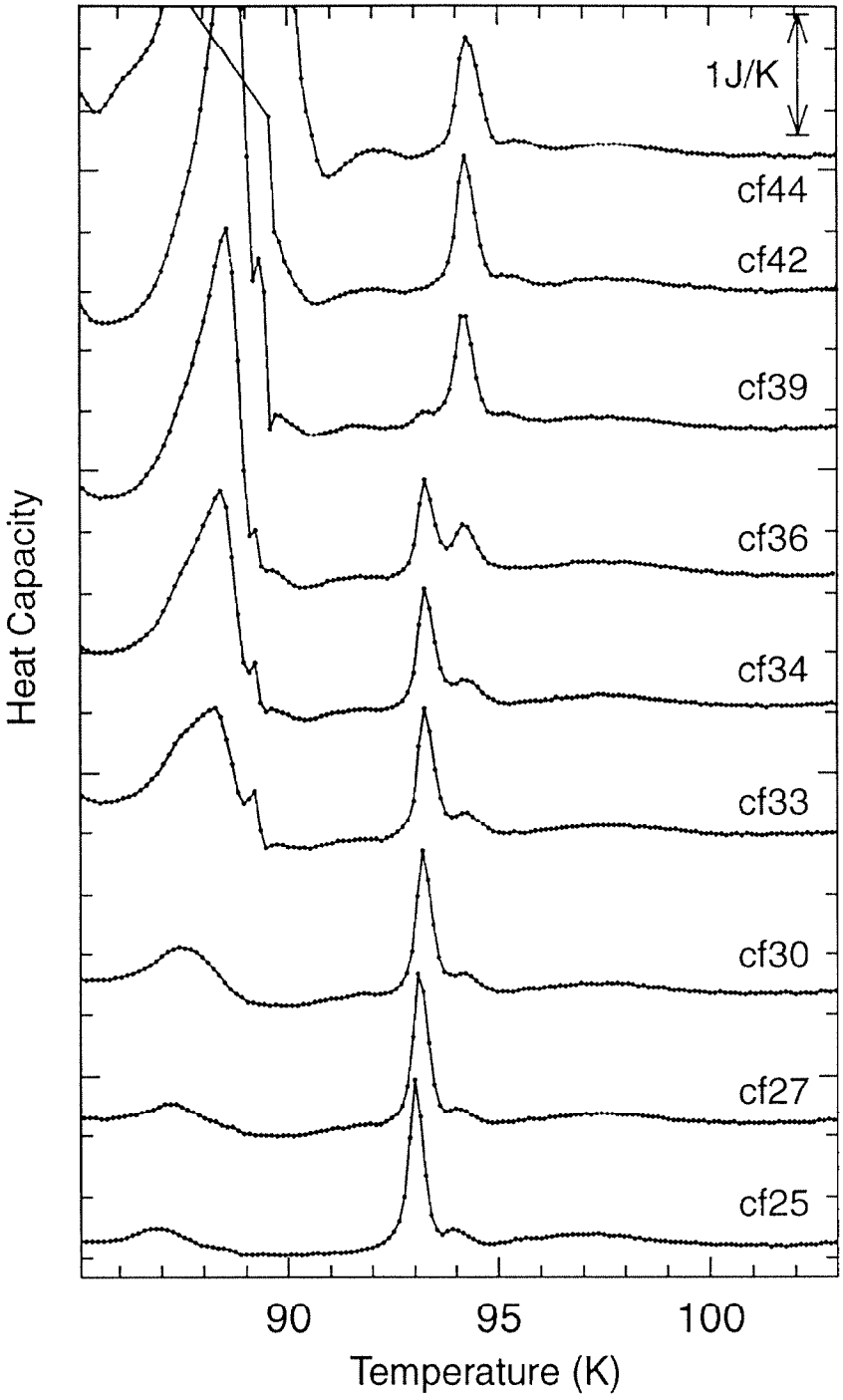

Figure B.8: Heat capacity scans for high coverages. The high temperature peaks are third- and fourth-layer melting. The large peaks around 89.5K are the melting of capillary-condensed material. Coverages, at low temperature, are 560.10, 624.7, 714.85, 905.23, 996.63, 1246.35, 1710.94, 2375.23, and 2693.70 stpccs.

T_t^{2D}	76.1K
T_t^X	85.0K
T_t^2	89.4K
T_t^3	93.1K
T_t^4	94.2K

Table B.1: Individual layer triple points in CF_4

yields a latent heat about 75% of that of first-layer melting, so it is unlikely that the second and third layers melt together at the 93.1K peak. The second layer must melt at higher temperature than the third layer, but we do not observe any sharp feature in the heat capacity up to 120K. There is a very shallow feature around 97K, a few degrees above the third-layer melting transition. It is possible that this feature is due to second, and possibly first, layer melting. It was found in the methane study that layer-melting peaks moved to higher temperature with increasing coverage and then broadened out, disappearing from view. Why the latent heat should diminish past the layer triple point is not understood.

The peaks at 94.2K in Fig. B.8 are identified tentatively as fourth-layer melting. If this identification of these peaks is correct, then the layer triple points for layers one through four increase in temperature with layer number, although with decreasing increments. Table B.4 lists the triple-point temperatures for layers one to four. Again, it is not clear what happens to third-layer melting, once the fourth layer forms. The fact that both third- and fourth-layer melting are observed in scan cf36 may be explained as being due to the formation of the fourth layer. In some regions the film is four layers thick and in some only three. We identify the fourth-layer melting peak tentatively because an alternative explanation for that peak is possible. Fourth-layer melting may occur at lower temperatures, perhaps around the triple point, and the peak at 94.2K may instead be due to third layer melting. The third-layer melting peak may shift by a degree when the (liquid) fourth layer forms on top if it, but then may remain at nearly constant tempera-

ture because film thickness does not continue to increase beyond four layers.

B.5 Conclusions about CF_4

We have found that CF_4/graphite is an extremely complex system, because of the orientational transition the incomplete mode of wetting. Insofar as the individual layer-melting transitions go, CF_4 is in some respects similar to CH_4, although the layer triple points in CH_4 all occur well below T_t. The CF_4 data, like the data for CH_4, do not show any of the behavior associated with preroughening found in Ar and Kr. In fact, the observation of layer triple points above T_t, along with the ellipsometry results, suggests that CF_4 belongs to a class of films that exhibit layering-transitions extending above T_t. The sequence of layer critical points, $T_{c,n}$, cannot converge to a temperature above T_t in the limit $n \rightarrow \infty$, but it can converge to T_t. If this is the case, then CF_4's 111 facet does not have a roughening transition.

Appendix C

Log of runs

This appendix lists the total number in the system for each of the heat capacity runs conducted in this experiment. The total number includes the number in the film and the number in the vapor phase in the sample cell, the filltube, and in the plumbing connected to the barocel pressure sensor at room temperature. The number in the fill tube was found to be approximately $N_{filltube} \simeq 0.08779P + 7.55 \times 10^{-5}T$. The free volume of the sample cell is 100.1 ccs, and the volume at room temperature is 68.4 ccs. The vast majority of runs were with films formed on the adsorption branch. Those films formed on the desorption branch are marked. Numbers are given in stpccs (cubic centimeters at standard temperature and pressure), and also in equivalent layers. The power dissipated in the CTM, P_{std}, which determines the scan rate, is also given. Coverages for the CF_4 scans are given in 2×2 layers, where one 2×2 layer is 124 stpccs. This value was found by multiplying the $\sqrt{3} \times \sqrt{3}$ coverage of 165 stpccs, found in Lysek's methane study, by 3/4.

Argon runs:

ar00-ar08 debugging runs.

ar09	0.00	background run	P_{std} = .045 Watts
ar10	0.00	background run	P_{std} = .0255 Watts

scans ar11-18 used P_{std} = 0.045 Watts (about 2K/hour)

ar11	0.00	calibration of dr resistor in: dr = 9.95×10^{-3} ohms.
ar11	0.00	filltube calibration run.
ar13	540.	(2.45 layers)
ar14	540.	(2.45 layers) heat capacity reproduced to 0.1%
ar15	540.	(2.45 layers)
ar16	936.	(4.38 layers)
ar17	3483.	(15.83 layers) T = 62 to 79K.
ar18	3483.	(15.83 layers) T = 80 to 90K. P_{std} = 0.015 W

Scans ar19-73 were taken at $P_{std} = .038 Watts$ (about 3K/2hours)

ar19	264.	(1.20 layers)
ar20	302.	(1.37 layers)
ar21	385.	(1.75 layers)
ar22	402.	(1.82 layers)
ar23	440.	(2.00 layers)
ar24	494.	(2.25 layers)
ar25	572.	(2.60 layers)
ar26	627.	(2.85 layers)
ar27	681.	(3.10 layers)
ar28	740.	(3.35 layers)
ar29	792.	(3.60 layers)
ar30	825.	(3.75 layers)
ar31	857.	(3.90 layers)
ar32	913.	(4.15 layers)
ar33	989.	(4.50 layers)
ar34	1023.	(4.65 layers)
ar35	1057.	(4.80 layers)
ar36	1088.	(4.95 layers)
ar38	0.00	background run at 0.038 Watts (about 3K/2hours)
ar38	1111.	(5.05 layers)
ar39	1158.	(5.26 layers)
ar40	1262.	(5.74 layers)
ar41	1301.	(5.90 layers)
ar42	1369.	(6.22 layers)
ar43	1437.	(6.53 layers)
ar44	1542.	(7.01 layers)
ar45	1801.	(8.18 layers)
ar46	2051.	(9.32 layers)
ar47	2273.	(10.33 layers)
ar48	2602.	(11.83 layers)

ar49	3032.	(13.78 layers)
ar50	3272.	(14.87 layers)
ar52	709.	(3.22 layers)
ar53	952.	(4.32 layers)
ar54	1122.	(5.10 layers)
ar55	1155.	(5.25 layers)
ar56	1220.	(5.55 layers)
ar57	1297.	(5.90 layers)
ar58	1385.	(6.30 layers)
ar59	1441.	(6.54 layers)
ar60	1507.	(6.85 layers)
ar61	1606.	(7.30 layers)
ar62	1695.	(7.71 layers)
ar63	1759.	(8.00 layers)
ar64	1869.	(8.50 layers)
ar65	1979.	(9.00 layers)
ar66	2200.	(10.00 layers)
ar67	2530.	(11.50 layers)
ar68	2805.	(12.75 layers)
ar69	3576.	(16.25 layers)
ar70	4510.	(20.50 layers)
ar71	358.	(1.63 layers)
ar72	660.	(3.00 layers)
ar73	693.	(3.15 layers)

Krypton runs

kr00	0.00	backrground run at 0.045 watts.
kr01	107.	(0.41 layers)
kr02	143.	(0.55 layers)
kr03	168.	(0.65 layers)
kr04	233.	(0.90 layers)
kr05	280.	(1.08 layers)
kr06	320.	(1.23 layers)
kr07	359.	(1.38 layers)
kr08	407.	(1.57 layers)
kr09	456.	(1.75 layers)
kr10	505.	(1.94 layers)
kr11	574.	(2.21 layers)

kr12	613.	(2.36 layers)		
kr13	652.	(2.51 layers)		
kr14	700.	(2.69 layers)		
kr15	746.	(2.87 layers)		
kr16	801.	(3.08 layers)		
kr17	824.	(3.17 layers)		
kr18	873.	(3.36 layers)		
kr19	965.	(3.71 layers)		
kr20	1030.	(3.96 layers)		
kr21	1111.	(4.27 layers)		
kr22	1202.	(4.62 layers)		
kr23	1303.	(5.01 layers)		
kr24	1409.	(5.42 layers)		
kr25	1557.	(5.99 layers)		
kr26	1704.	(6.55 layers)		
kr27	1849.	(7.11 layers)		
kr28	2036.	(7.83 layers)		
kr29	2211.	(8.50 layers)		
kr30	2430.	(9.35 layers)		
kr31	2544.	(9.79 layers)		
kr32	2816.	(10.83 layers)		
kr33	3108.	(11.95 layers)		
kr34	3487.	(13.41 layers)		
kr35	3870.	(14.88 layers)		
kr36	4272.	(16.43 layers)		
kr37	4660.	(17.92 layers)		
kr38	5433.	(20.90 layers)		
kr39	3621.	(13.93 layers)	desorption	
kr40	3577.	(13.76 layers)	desorption	$P_{std} = .015$ W
kr41	3564.	(13.71 layers)	desorption	$P_{std} = .008$ W
kr42	3559.	(13.96 layers)	desorption	$P_{std} = .008$ W
kr43	3557.	(13.98 layers)	desorption	$P_{std} = .008$ W
kr44	3557.	(13.98 layers)	desorption	$P_{std} = .008$ W
kr45	1212.	(4.66 layers)	desorption	
kr46	315.	(1.21 layers)	desorption	
kr47	761.	(2.93 layers)		
kr48	781.	(3.01 layers)		
kr49	803.	(3.09 layers)		
kr50	823.	(3.17 layers)		
kr51	841.	(3.24 layers)		

kr52	863.	(3.31 layers)
kr53	883.	(3.39 layers)
kr54	902.	(3.47 layers)
kr55	922.	(3.55 layers)
kr56	942.	(3.62 layers)
kr57	962.	(3.70 layers)
kr58	982.	(3.78 layers)
kr59	1003.	(3.86 layers)

CF_4 runs

$P_{std} = 0.045$ Watts for all the CF_4 runs.

cf01	42.	(0.34 layers)
cf02	84.	(0.68 layers)
cf03	120.	(0.97 layers)
cf04	155.	(1.25 layers)
cf05	177.	(1.43 layers)
cf06	209.	(1.69 layers)
cf07	247.	(2.00 layers)
cf08	272.	(2.20 layers)
cf09	94.	(0.75 layers)
cf10	105.	(0.85 layers)
cf11	113.	(0.91 layers)
cf12	117.	(0.95 layers)
cf13	122.	(0.99 layers)
cf14	126.	(1.02 layers)
cf15	130.	(1.05 layers)
cf16	134.	(1.08 layers)
cf17	138.	(1.12 layers)
cf18	147.	(1.19 layers)
cf19	299.	(2.42 layers)
cf20	344.	(2.78 layers)
cf21	400.	(3.23 layers)
cf22	447.	(3.61 layers)
cf23	490.	(3.96 layers)
cf24	530.	(4.28 layers)
cf25	560.	(4.53 layers)
cf26	590.	(4.77 layers)
cf27	625.	(5.05 layers)

cf28	639.	(5.16 layers)
cf29	676.	(5.46 layers)
cf30	715.	(5.78 layers)
cf31	734.	(5.93 layers)
cf32	788.	(6.37 layers)
cf33	905.	(7.31 layers)
cf34	997.	(8.06 layers)
cf35	1100.	(8.89 layers)
cf36	1246.	(10.07 layers)
cf37	1368.	(11.05 layers)
cf38	1493.	(12.06 layers)
cf39	1711.	(13.83 layers)
cf40	1973.	(15.94 layers)
cf41	2201.	(17.78 layers)
cf42	2375.	(19.19 layers)
cf43	2522.	(20.38 layers)
cf44	2694.	(21.77 layers)
cf45	2989.	(24.15 layers)

Bibliography

[1] R. H. Fowler and E. A. Guggenheim. *Statistical Thermodynamics.* Cambridge University Press, Teddington, England, 1939.

[2] G. D. Halsey. *J. Chem. Phys.*, 16:931, 1948.

[3] T. L. Hill. *J. Chem. Phys.*, 15:767, 1947.

[4] M. H. Polley, W. D. Schaeffer, and W. R. Smith. *J. Chem. Phys.*, 57:469, 1953.

[5] A. Thomy and X. Duval. *J. Chim. Phys.*, 66:1966, 1969.

[6] A. Thomy and X. Duval. *J. Chim. Phys.*, 67:286, 1970.

[7] A. Thomy and X. Duval. *J. Chim. Phys.*, 67:1101, 1970.

[8] Grafoam is a trademark of the Union Carbide Corperation.

[9] W. A. Steele. *The Interaction of Gases with Solid Surfaces.* Pergamon, Oxford, 1974.

[10] D. L. Goodstein, J. G. Dash, and W. D. McCormick. *Phys. Rev. Lett.*, 15:447, 1965.

[11] D. L. Goodstein, W. D. McCormick, and J. G. Dash. *Cryogenics*, 6:167, 1966.

[12] R. J. Bergeneau, P. A. Heiney, and J. P. Pelz. *Physica (Utrecht)*, 109/110B:1785, 1982.

[13] D. R. Nelson and B. I. Halperin. *Phys. Rev. B*, 19:2457, 1979.

[14] A. P. Young. *Phys. Rev. B*, 19:1855, 1979.

[15] J. M. Kosterlitz and D. J. Thouless. *J. Phys. C*, 6:1181, 1973.

[16] J. M. Kosterlitz. *J. Phys. C*, 7:1046, 1974.

[17] M. E. Fisher, B. I. Halperin, and R. Morf. *Phys. Rev. B*, 20:4692, 1979.

[18] S. T. Chui. *Phys. Rev. Lett.*, 48:933, 1982.

[19] S. T. Chui. *Phys. Rev. B*, 28:178, 1983.

[20] H. Taub, K. Caniero, J. K. Kjems, L. Passell, and J. P. McTague. *Phys. Rev. B*, 16:455, 1978.

[21] C. Tiby and H. Lauter. *Surf. Sci.*, 117:277, 1982.

[22] T. T. Chung. *Surf. Sci.*, 87:348, 1979.

[23] Y. Larher. *Surf. Sci.*, 87:348, 1979.

[24] J. P. McTague, J. Als-Nielsen, J. Bohr, and M. Nielsen. *Phys. Rev. B*, 25:7765, 1982.

[25] D. M. Butler, J. A. Litzinger, A. J. Stewart, and R. B. Griffiths. *Phys. Rev. Lett.*, 42:1289, 1979.

[26] E. D. Specht, A. Mak, C. Peters, M. Sutton, R. J. Birgeneau, K. L. D'Aminco, D. E. Moncton, S. E. Naylor, and P. M. Horn. *Z. Phys. B, Cond. Matt.*, 69:347, 1987.

[27] M. H. W. Chan. Phase transitions in monolayer films adsorbed on graphite. In H. Taub, editor, *Phase Transitions in Surface Films 2*, page 1. Plenum Press, New York, 1991.

[28] A. D. Migone, M. H. W. Chan, K. J. Niskanan, and R. R. Griffiths. *J. Phys. C*, 16:L1115, 1983.

[29] M. H. W. Chan, A. D. Migone, K. D. Miner, and Z. R. Li. *Phys. Rev. B*, 30:2681, 1984.

[30] D. M. Zhu and J. G. Dash. *Phys. Rev. Lett.*, 60:432, 1988.

[31] D. M. Zhu and J. G. Dash. *Phys. Rev. B*, 38:11673, 1988.

[32] J. Z. Larese and Q. M. Zhang. *Phys. Rev. Lett.*, 64:922, 1990.

[33] J. M. Gay, J. Suzanne, J. G. Dash, and H. J. Lauter. *J. Phys I France*, 1:1279, 1991.

[34] Rahul Pandit, M. Schick, and Michael Wortis. *Phys. Rev. B*, 26:5112, 1982.

[35] R. J. Muirhead, J. G. Dash, and J. Krim. *Phys. Rev. B*, 29:5074, 1984.

[36] F. T. Gittes and M. Shick. *Phys. Rev. B*, 30:209, 1984.

[37] D. A. Huse. *Phys. Rev. B*, 29:6985, 1984.

[38] see G. B. Hess in ref. [27].

[39] J. W. O. Faul, U. G. Volksmann, and K. Knorr. *Surf. Sci*, 227:390, 1990.

[40] H. S. Youn. *Phys. Rev. Lett.*, 64:918, 1990.

[41] F. Ser, Y. Lahrer, and B. Gilquin. *Molec. Phys.*, 67:1077, 1989.

[42] U. G. Volkmann and K. Knorr. *Surf. Sci*, 221:379, 1989.

[43] G. Zimmerli and M. H. W. Chan. unpublished.

[44] L. Bruschi, G. Torzo, and M. H. W. Chan. *Europhys. Lett.*, 6:541, 1988.

[45] M. J. Lysek, M. LaMadrid, P. K. Day, and D. L. Goodstein. to be published in Phys. Rev. B.

[46] M. J. Lysek. *A thermodynamic study of layering and capillary condensation in methane adsorbed of graphite foam.* PhD thesis, Caltech, Pasadena, CA, 1992.

[47] W. F. Saam. *Surf. Sci*, 125:253, 1983.

[48] M. J. De Olivera and B. Griffiths. *Surf. Sci*, 71:687, 1978.

[49] M. P. Nightingale, W. F. Saam, and M. Shick. *Phys. Rev. B*, 30:3830, 1984.

[50] Q. M. Zhang, Y. P. Feng, H. K. Kim, and M. H. W. Chan. *Phys. Rev. Lett.*, 57:1456, 1986.

[51] H. K. Kim, Y. P. Feng, and Q. M. Zhang. *Phys. Rev. B*, 37:3511, 1988.

[52] M. H. W. Chan and Y. P. Feng. *Am. Phys. Soc. Bul.*, 33:283, 1988.

[53] B. Gilquin, 1979. D. Sc. thesis, Nancy.

[54] D. M. Zhu and J. G. Dash. *Phys. Rev. Lett.*, 57:2959, 1986.

[55] Y. P. Feng. *Phys. Rev. Lett.*, 64:2148, 1990.

[56] S. E. Polanco and M. Bretz. *Phys. Rev. B*, 17:151, 1978.

[57] J. Ma, T. A. Sullivan, and O. E. Vilches. *J. App. Phys.*, 26:263, 1987.

[58] H. S. Youn and G. B. Hess. *Phys. Rev. Lett.*, 64:918, 1990.

[59] H. S. Youn and G. B. Hess. *Phys. Rev. Lett.*, 64:443, 1990.

[60] M. J. Lysek, P. K. Day, M. LaMadrid, and D. L. Goodstein. To be published in Rev. Sci. Instru.

[61] The non-preemptive multitasking kernel was adapted by Mark Lysek from: R. M. Foard. Multitasking Meathods. *P. C. Tech Journal*, page 53, March 1986.

[62] VCR is a registered trademark of the Cajon Corporation.

[63] G. A. Cook. *Argon, Helium, and the Rare Gases; the Elements of the Helium Group.* Interscience Publishers, New York, 1961.

[64] M. J. Lysek, M. LaMadrid, P. K. Day, and D. L. Goodstein. to be published.

[65] E. Cheng and M. W. Cole. *Phys. Rev. B*, 41:9650, 1990.

[66] K. Morishige, K. Kawamura, M. Yamamoto, and I. Ohfuji. *Langmuir*, 6:1417, 1990.

[67] A. D. Migone, Z. R. Li, and M. H. W. Chan. *Phys. Rev. Lett.*, 53:810, 1984.

[68] Q. M. Zhang and J. Z. Larese. *Phys. Rev. B*, 43:938, 1991.

[69] D. L. Goodstein, private communication.

[70] W. K. Burton and N. Cabrera. *Disc. Faraday Soc.*, 5:33, 1949.

[71] W. K. Burton, N. Cabrera, and F. C. Frank. *Phil. Trans. Roy. Soc. London*, 243A:299, 1951.

[72] L. Onsager. *Phys. Rev.*, 65:117, 1944.

[73] H. J. Leamy, G. H. Gilmer, and K. A. Jackson. *Surface Physics of Materials*, volume 1, page 121. Academic, New York, 1975.

[74] J. D. Weeks. *Ordering in Strongly Fluctuating Condensed Matter Systems*, page 293. Plenum, New York, 1980.

[75] S. T. Chui and J. D. Weeks. *Phys. Rev. B*, 14:4978, 1976.

[76] T. Ohta and K. Kawasaki. *Prog. Theor. Phys.*, 60:365, 1978.

[77] J. V. Jose, L. P. Kadanoff, S. Kirkpatrick, and D. R. Nelson. *Phys. Rev. B*, 16:1217, 1977.

[78] J. E. Avron, L. S. Balfur, C. G. Landau, S. G. Libson, and L. S. Shulman. *Phys. Rev. Lett.*, 45:814, 1980.

[79] K. A. Jackson. *Liquid Metals and Solidification*, page 174. ASM, Cleveland, 1958.

[80] K. A. Jackson. *Progress in Solid State Chemistry*, volume 4, page 53. Pergamon, New York, 1958.

[81] J. D. Weeks. *Phys. Rev. B*, 26:3998, 1982.

[82] K. Rommelse and M. den Nijs. *Phys. Rev. Lett.*, 59:2578, 1987.

[83] M. den Nijs. *Phys. Rev. Lett.*, 64:435, 1990.

[84] M. den Nijs. *Phys. Rev. Lett.*, 66:907, 1991.

[85] M. den Nijs. *Phase Transitions in Surface Films 2*, page 247. Pergamon, New York, 1991.

[86] P. K. Day and P. Weichman. Unpublished.

[87] D. B. Pengra, D. M. Zhu, and J. G. Dash. *Surf. Sci*, 245:125, 1991.

[88] R. Gangwar and R. M. Suter. *Phys. Rev. B*, 42:2711, 1990.

[89] R. F. Hainsey, R. Gangwar, J. D. Shindler, and R. M. Suter. *Phys. Rev. B*, 44:3365, 1991.

[90] M. J. Lysek, M. LaMadrid, P. K. Day, and D. L. Goodstein. *Langmuir*, 8, 1992.

[91] J. W. M. Frenken, P. M. J. Maree, and J. F. van der Veen. *Phys. Rev. B*, 34:7506, 1986.

[92] J. W. M. Frenken and J. F. van der Veen. *Phys. Rev. Lett.*, 54:134, 1985.

[93] J. C. Heyraud, J. J. Metois, and J. M. Bermond. *Journal of Crystal Growth*, 98:355, 1989.

[94] A. W. Denier van der Gon, R. J. Smith, J. M. Gay, D. J. O'Connor, and J. F. van der Veen. *Surf. Sci*, 227:143, 1990.

[95] B. Pluis, A. W. Denier van der Gon, and J. F. van der Veen. *Surf. Sci*, 239:265, 1990.

[96] A. W. Denier van der Gon, H. M. van Pinxteren, J. W. M. Frenken, and J. F. van der Veen. *Surf. Sci*, 244:259, 1991.

[97] J. F. van der Veen. *Phase Transitions in Surface Films 2*, page 289. Pergamon, New York, 1991.

[98] J. K. Kristensen and R. M. J. Cotterill. *Phil. Mag.*, 36:437, 1977.

[99] J. Q. Broughton and G. H. Gilmer. *Acta. Meta.*, 31:31, 1983.

[100] M. S. Pettersen, M. J. Lysek, and D. L. Goodstein. *Phys. Rev. B*, 40:4938, 1989.

[101] J. Krim and J. G. Dash. *Surf. Sci*, 162:421, 1985.

[102] D. M. Zhu. *Surface Melting in Multilayer Argon and Neon Films.* PhD thesis, University of Washington, Seatle, WA, 1988.

[103] R. Defay and I. Prigogine. *Surface Tension and Adsorption.* John Wiley and Sons, Inc., New York, 1966.

[104] A. A. Antoniou. *J. Phys. Chem.*, 68:2754, 1964.

[105] J. L. Tell and H. J. Maris. *Phys. Rev. B*, 28:5122, 1983.

[106] D. D. Awschalom and J. Warnock. *Phys. Rev. B*, 35:6779, 1987.

[107] P. Buffat and J. P. Borel. *Phys. Rev. A*, 13:2287, 1976.

[108] H. S. Nham, M. Dhir, and G. B. Hess. *Phys. Rev. B*, 35:3675, 1987.

[109] G. Zimmerli and M. H. W. Chan. *Phys. Rev. B*, 45:9347, 1992.

[110] J. H. Smith and E. L. Pace. *J. Phys. Chem.*, 73(12):4232, 1969.

[111] K. Kjaer, M. Nielsen, J. Bohr, H. J. Lauter, and J. P. McTague. *Phys. Rev. B*, 26:5168, 1982.